Title
High Resolution Calorimetry for Thermal and Biological Applications

Author
Dechaumphai, Edward

Publication Date
2016

UNIVERSITY OF CALIFORNIA, SAN DIEGO

High Resolution Calorimetry for Thermal and Biological Applications

A Dissertation submitted in partial satisfaction of the
requirements for the degree
Doctor of Philosophy

in

Engineering Sciences (Mechanical Engineering)

by

Edward Dechaumphai

Committee in charge:

Professor Renkun Chen, Chair
Professor Prabhakar R. Bandaru
Professor Ratneshwar Lal
Professor Zhaowei Liu
Professor Liangfang Zhang

2016

The Dissertation of Edward Dechaumphai is approved, and it is acceptable in quality and form for publication on microfilm and electronically:

Chair

University of California, San Diego

2016

DEDICATION

Dedicated to my family for their unconditional love and supports.

TABLE OF CONTENTS

LIST OF FIGURES

ACKNOWLEDGEMENTS

First and foremost, I would like to express my sincere appreciation and gratitude to my advisor, Prof. Renkun Chen, who molds me into a scientist/engineer that even myself could not imagine I could be one day. I would like to thank him for his unmatched dedications and for making futures of his students and their well beings as his main priorities. His guidance makes my Ph.D. experience particular fulfilling. I am very grateful to be in the group with a very strong work ethic, interesting projects, and a very friendly working atmosphere, a culture that Prof. Chen instilled in our group. I truly believe that my career path cannot come this far without his inspirations and supports.

I would like to thank Prof. Zhaowei Liu and Prof. Eric Fullerton for a great collaboration on studying thermal transport across a multilayer film with a highly mismatched material pair. I thank Prof. George Tynan for our pleasant collaboration on investigating thermal properties of near-surface regime ion-damaged tungsten used as plasma facing components. I would like to thank Prof. Ratneshwar Lal on his support on biocalorimeter project. In addition, I thank Prof. Prabhakar R. Bandaru and Prof. Liangfang Zhang for being part of my dissertation committee, showing their interests in, and providing helpful advices for my research.

I also would like to recognize and thank my co-worker/my friend, Sahngki Hong, who works on my biocalorimeter project with me. The progress of this project is driven by his hard work and his creative solutions to different problems we faced. I appreciate many extra hours that we worked together to overcome many experimental challenges. In short, I cannot ask for a better person to work with me on this project.

My experiences as a Ph.D. student cannot be this joyful without wonderful fellow graduate students in our lab. Therefore, I want to thank all of Renkun Chen's former and current group members including Jaeyun Moon, Matthew Wingert, Jianlin Zheng, Sahngki Hong, Shuang Cui, Sunmi Shin, Young Jin Kim, Soonshin Kwon, Gunwoo Kim, Lizzie Cladwell, Qingyang Wang, Patrick Charles, Minjae Lee, Kristine McGrath, Taylor Yuen, Cheng-Kai Li, and Jongok Choi for many great discussions, both technical and non-technical, and for always show helping hands when I needed them.

A lot of my research works relies on fabricating micro/nano devices inside cleanroom. With that, I thank all of the Nano3 personnel: Bernd Fruhberger, Larry Grissom, Ivan Harris, Sean Parks, Xuekun Lu, Ryan Anderson, and Maribel Montero who make sure our cleanroom at UC San Diego always run very smoothly. I would like to thank them for their advices on microfabrications and for always assisting me when I faces problems inside the cleanroom.

Throughout my Ph.D. career, I met many great people in San Diego. I would like to thank my friends, in particular: Tissana Kijsanayotin, Praween Siritanasak, Wiroj Nantasetphong, Teerapong Pirojsirikul, Kumpee Chansang, and Votsawat Chaichitt for all the fun and relaxing experiences here. I also would like to acknowledge and thank the Thai community in San Diego including June and Brian Sanders for helping me settle in San Diego. I also want to thank Soracha Thamphiwatana for teaching me how to culture cells. More importantly, I would like to thank her for her kindness, humor, care, and for making my time here very colorful.

My gratitude also goes to my Aunt and Uncle, Boonlom and Sangob Mangkonkarn, who I grew up with when I came to America when I was 14. I thank them for teaching me and raising me as if I am their own son. A paragraph here cannot even express how grateful I am for their sacrifices they made for me. I also would like to thank Lisa Mangkonkarn, Kashane Mangkonkarn, and Munkanit Viphunphong for taking me into their arms as their brother.

I would like to express my deepest gratitude to my family and for making me feel I am always being loved. I thank my sister, Anna Dechaumphai, for always being my delightful sister. Growing up together, I can see the person who she is turning into and that makes me very proud of her. Lastly, I would like to thank my parents Pramote and Yupa Dechaumphai for their love, supports, and encouragements. We are usually on the opposite side of the world and I miss them dearly everyday, but their unconditional love always helps me through difficult days. I thank my parents for being the most awesome parents anyone could ask for. This Ph.D. degree and dissertation is dedicated to them.

Chapter 2, in part, is a reprint of the material in Nanoletters, 2014, Edward Dechaumphai, Dylan Lu, Jimmy J. Kan, Jaeyun Moon, Eric E. Fullerton, Zhaowei Lie, and Renkun Chen. The dissertation author was the primary investigator and the first author of this paper.

Chapter 3, in part, is a reprint of the material in Journal of Nuclear Material, 2014, Edward Dechaumphai, Joseph L. Barton, Joseph R. Tesmer, Jaeyoon Moon, Yongqiang Wang, George R. Tynan, Russ P. Doerner, and Renkun Chen. The dissertation author was the primary investigator and the first author of this paper.

Chapter 4, in part, is a reprint of the material in Review Scientific Instruments, 2013, Jianlin Zheng, Matt Wingert, Edward Dechaumphai, and Renkun Chen. The dissertation author was the primary investigator and the co-first author of this paper.

Chapter 4, in part, is a reprint of the material in Review Scientific Instruments, 2014, Edward Dechaumphai and Renkun Chen. The dissertation author was the primary investigator and the first author of this paper.

Chapter 5, in part, is in a manuscript in preparation, Sahngki Hong, Edward Dechaumphai, Ratneshwar Lal and Renkun Chen. The dissertation author was the primary investigator and the co-first author of this paper.

Edward Dechaumphai

San Diego, CA

May, 2016

VITA

2010	B. S. in Mechanical Engineering (with minor in Project Management), University of Maryland, College Park
2012	M. S. in Engineering Sciences (Mechanical Engineering), University of California, San Diego
2016	Ph. D. in Engineering Sciences (Mechanical Engineering), University of California, San Diego

PUBLICATIONS

E. Dechaumphai and R. Chen, “Sub-picowatt Resolution Calorimetry with Niobium Nitride Thin-film Thermometer”, Rev. Sci. Instrum., 85, 094903, (2014).

E. Dechaumphai, D. Lu, J.J. Kan, J.Moon, E.E. Fullerton, Z. Liu, and R. Chen. “Ultralow Thermal Conductivity of Multilayers with Highly Dissimilar Debye Temperature”, Nano Lett., 14 (5), 2448-2455 (2014).

E. Dechaumphai, J. Moon, M.C. Wingert, and R. Chen. “Engineering Phononic and Electronic Transport in Nanowires for Enhanced Thermoelectrics”, Book Chapter in ‘Semiconductor Nanowires: From Next-Generation Electronics to Sustainable Energy’, Royal Society of Chemistry, (2014).

E. Dechaumphai, J.L. Barton, J.R. Tesmer, J. Moon, Y.Q. Wang, G.R. Tynan, R.P. Doerner, and R. Chen. “Near-Surface Thermal Characterization of Plasma Facing Components Using the 3-omega Method”, J. Nucl. Mater., 445, 56-60 (2014).

J. Zheng*, M.C. Wingert*, **E. Dechaumphai***, R. Chen. “Sub-picowatt/Kelvin resistive thermometry for probing nanoscale thermal transport”, Rev. Sci. Instrum., 84, 114901 (2013). **(* = J. Zheng, M.C. Wingert, and E. Dechaumphai contributed equally to this work)**

E. Dechaumphai and R. Chen. “Thermal Transport in Phononic Crystals: the Role of Zone Folding Effect”, J. Appl. Phys., 111, 073508 (2012).

M. C. Wingert*, Z. C. Y. Chen*, **E. Dechaumphai**, J. Moon, J. Kim, J. Xiang, and R. Chen. “Thermal conductivity of Ge and Ge-Si Core-Shell Nanowires In the Phonon Confinement Regime”, Nano Lett., Vol. 11, pp. 5507-5513, 2011.

E. Dechaumphai, Z. Zhang, N.P. Siwak, R. Ghodssi, and T. Li. “Resonant frequency of gold/polycarbonate hybrid nano resonators fabricated on plastics via nanotransfer printing”, Nanoscale Research Letters, Vol. 6, No. 90, 2011.

ABSTRACT OF THE DISSERTATION

High Resolution Calorimetry for Thermal and Biological Applications

by

Edward Dechaumphai

Doctor of Philosophy in Engineering Sciences (Mechanical Engineering)

University of California, San Diego, 2016

Professor Renkun Chen, Chair

Calorimetry is a heat measuring process that quantifies heat generation, loss, and transport. Calorimetry holds significant values to a multitude of scientific disciplines such as nanoscale heat transfer, bolometer infrared detection, and drug discovery. This dissertation focuses on two aspects of calorimetry: 1) application of a calorimetry technique to investigate fundamentals of thermal transport at micro/nanoscale level, and 2) development of high-resolution microfluidic calorimeters for biological applications.

A modulated calorimetry technique, namely, the 3ω method, was used to study thermal transport across highly mismatched interfaces, where Au/Si multilayers (MLs), were used as the model material. By leveraging thermal resistance at interfaces of Au and Si, which have highly dissimilar acoustic impedance, we experimentally demonstrated an ultralow thermal conductivity, κ, of 0.33 ± 0.04 W $\mathrm{m}^{-1}\mathrm{K}^{-1}$ at room temperature with a high interfacial density of $\sim$0.2 interface nm^{-1}. The measured κ was the lowest amongst inorganic MLs with similar interfacial density. The 3ω method was also applied to measure thermal conductivity of the near-surface regime of tungsten damaged by ion irradiation used in plasma facing components (PFCs) in fusion reactors. The measurement showed a nearly 60% reduction in κ in comparison to pristine tungsten, which can be detrimental to the mechanical integrity of the PFCs under heat fluxes

The second thrust of the dissertation is focused on the development of high-resolution calorimeters. A high performance resistive thermometer material, NbNx, was developed and integrated into a suspended bridge calorimeter. When used with a modulated heating current and a differential instrumentation schemes, the NbNx-based calorimeter demonstrated an exceptional high power resolution of 0.26 pW at room temperature. Furthermore, the high-resolution calorimetry was extended to microfluidic platform for biological applications. Owing to the low parasitic heat loss and a long-term temperature stability platform, the biocalorimeters developed from this study possess a significant enhancement over the state-of-the-art long-term power detection limit, which enable the detection of metabolic rate of individual living cells in the microfluidic channels. Such a biocalorimetry technique will open up new opportunities in a biomedical field such as in cell and tissue metabolism, drug discovery and screening, and antibody-antigen detection.

Chapter 1

Fundamentals of High Resolution Calorimetry

1.1 Introduction to Calorimetry

Calorimetry is a heat measuring technique that quantifies generation, loss, or transport. Measuring heat holds significant values to many scientific fields and engineering applications. The first calorimetry experiment reported in a literature, conducted by Lavoisier and Laplace, was demonstrated to determine the metabolic rate of guinea pig. The heat was measured by placing a guinea pig in an ice calorimeter and observing the amount of ice that melts. Calorimetry is also a very essential technique to characterize thermal properties of a given material. Such measurements provide a foundation in understanding thermal transport in various materials. Being able to characterize thermal properties including thermal conductivity and specific heat of materials not only allows scientists and engineers to understand thermal transport physics in materials, but also provides guidelines to engineering designs. In a specific case, for instance, as the size of electronics miniaturized, the power density increases and leads to overheating of electronic components [1]. When the size of the material is reduced down to nanometer scale, the thermal properties can be different from what is observed is bulk materials [2,3]. These understandings in nanoscale heat transport generates broader impacts in technological development [4] such as developments in heat-assisted magnetic recording [5], thermal management in microelectronics [6–10], phase change memories technology [11–13], thermoelectric energy conversion [14–20], and a new class of insulating materials. However, quantifying thermal properties of micro/nano-materials require a high-resolution calorimetry technique. Therefore, developing a high-resolution calorimeter to study heat transport at nanoscale will greatly propel the advancement in nanotechnology.

Beyond developing a calorimeter for fundamental studies in thermal transport, a high-resolution calorimeters are employed as IR detector known as bolometer [21, 22]. Calorimeters are also widely used in biomedical field. For instance, at an early state of drug screening process before clinical trials, there are an immense possible number of drug compounds that can be the ‘hit’ compound. A calorimetry technique is then applied to measure the thermodynamics properties of each compound in order to isolate a promising compounds from the rest. However, thermal characterization of compounds are done at the later stage of the drug screen process because current calorimeters require a large amount of sample and the measurement time is time consuming. If a calorimeter becomes more sensitive, then a calorimeter can be brought into play at an early stage and accelerate the drug discovery process [23]. In addition, calorimetry can even be used as a rapid bacteria detection method such as what were demonstrated for detecting *Mycobacterium tuberculosis* [24,25].

In this chapter, I will discuss about the principles of a microfabricated suspended calorimeter that is used to study heat transport at nanoscale level and to observe heat generation from bio/chemical reactions; and the 3ω technique that is used to measure the thermal properties of bulk and thin film down to sub 100-nm thin. The goal of this chapter is to provide a brief technical background of calorimetry that leads to my research in understanding heat transport at nanoscale level, the development of a sub-picowatt high-resolution calorimeter and high-resolution calorimeter for biological applications in the latter chapters.

1.2 Principles of Microfabricated Suspended Calorimeter

In a calorimeter, a sensing chamber is connected to the thermal reservoir with a fixed temperature T. When a heat current is applied to the sensing chamber, the temperature then increases by ΔT. The temperature difference ΔT is dictated by the rate of heat transfer between the sensing chamber and the thermal reservoir, i.e. thermal conductance G. This relationship, which the basis of any calorimetry technique, can be written as

$$Q = G \times \Delta T. \tag{1.1}$$

Given the relationship above, the power resolution or the minimum detectable heating power a calorimeter can detect, Q_{res} depends on the thermal conductance between the calorimeter to the environment, and the minimum temperature a thermometer can sense. Therefore, the key factors for high-resolution calorimetry are: 1)

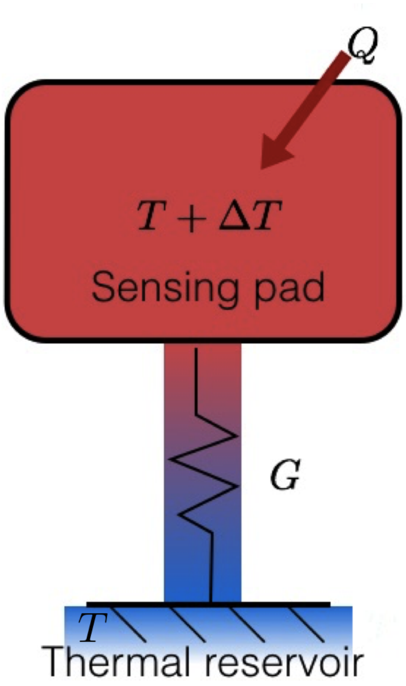

Figure 1.1: The principle of calorimetry: $Q = G \times \Delta T$.

to thermally isolate the sensing chamber from the thermal reservior leading to reduction in G and 2) to use a very sensitive thermometer in order to sense the minute changes in ΔT.

To reduce G, many researchers implemented a suspended structure to the calorimeter design to reduce thermal conductance between the sensing pad/chamber to the thermal reservoir similar to Fig.(1.2) [26–29].

As shown in the figure, a sensing pad/chamber is connected to the environment via a small cross-sectional area beam. Due to thin/long beam, the thermal conductance between the sensing chamber and the thermal reservoir is very small (assuming convective or radiative heat transfer can be eliminated by vacuum and low emissivity coating of the beam), where G for a single beam can be written as

$$G_{\text{half}} = \frac{\kappa A_c}{L}, \tag{1.2}$$

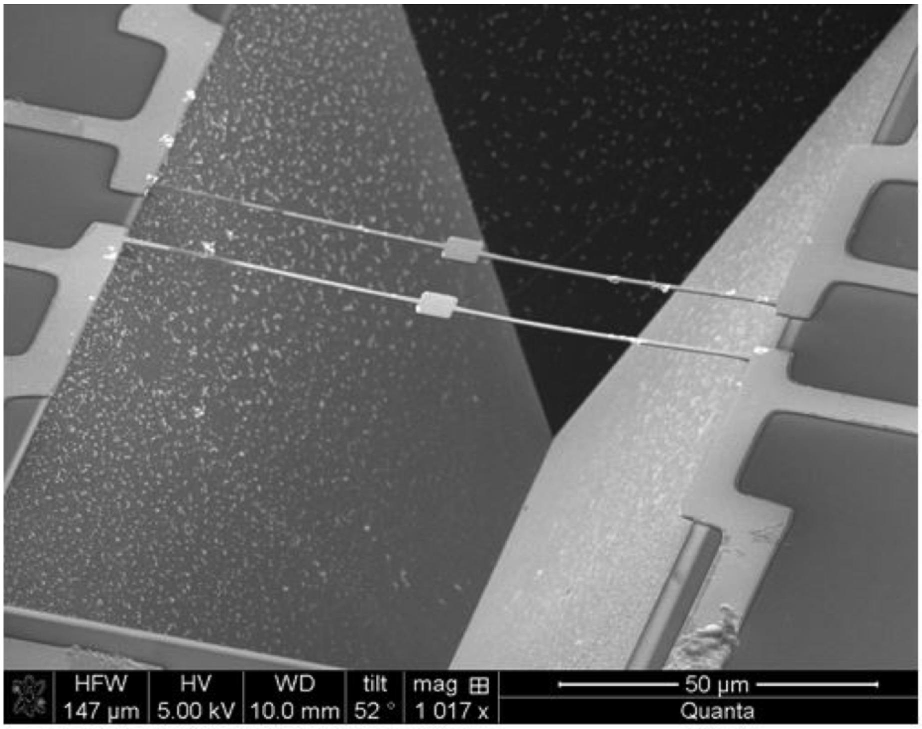

Figure 1.2: SEM image of a suspended calorimeter.

where G_{half} is the thermal conductance from the middle of the beam to the thermal reservoir, κ is the effective thermal conductivity of the material of the beam, A_c is the cross-sectional area of the beam, and L is the length of the beam from the middle to the end. Note that the total thermal conductance G_{total} in Fig.(1.2) will be $G_{total} = 2G_{\text{half}}$ since there are two half-beams. Another important aspects that cannot always be neglected is the thermal conductance from radiation. Radiative heat transport depends on the surface area of the device ($G_{rad} \approx 4\epsilon\sigma T_{avg}^3$, where ϵ is emissivity of the material, σ is Stefan-Boltzmann constant, and T_{avg} is the average temperature between the sample and the environment). Therefore, if the surface area is large, a significant heat loss can originate from thermal radiation and cannot be neglected in the thermal analysis. This will be described in detail in Chapters 4 and 5.

1.3 Principles of the 3ω Techniques

The 3ω technique is one of the most established, yet powerful, techniques to characterize thermal properties of bulk and thin film as thin as sub-100 nm. The technique to measure thermal conductivity of a solid with 3ω was developed by Cahill et al. [30]. In a nutshell, a thin metal strip is patterned on a sample of interest, where this metal strip acts as both resistive thermometer and heater. An AC current modulated at 1ω is applied, which generates 2ω heat flux and 2ω temperature change. By measuring a 3ω voltage, one can quantify the 2ω temperature rise at the surface caused by Joule heating. From the frequency-dependent temperature rise measurement data, known heat flux, and known geometry of the sample, the thermal conductivity of the sample of interest can then be obtained. A more detail principles of 3ω method will be discussed later in this section.

In the 3ω method, a microfabricated metal heater is pattern on top of the sample Fig.(1.3). A typical procedure for preparing 3ω samples are:

1. Deposition of electrically insulated thin film. If the sample is not electrically insulated (even if it is slightly electrically conductive), a thin insulation layer is needed on the sample such that there will be no current leakage between the heater/thermometer to the sample. An example of insulators are Al_2O_3, SiO_2, parylene, etc., which can be deposited using PECVD, CVD, or ALD process.

2. Electrode (heater/thermometer) patterning using either E-beam lithography, photolithography, or shadow mask.

3. Metal deposition, typically Au or Pt. A very thin Cr or Ti is usually needed as an adhesion layer between Au or Pt and the sample.

This microfabricated metal pattern, which acts as a resistive thermometer,

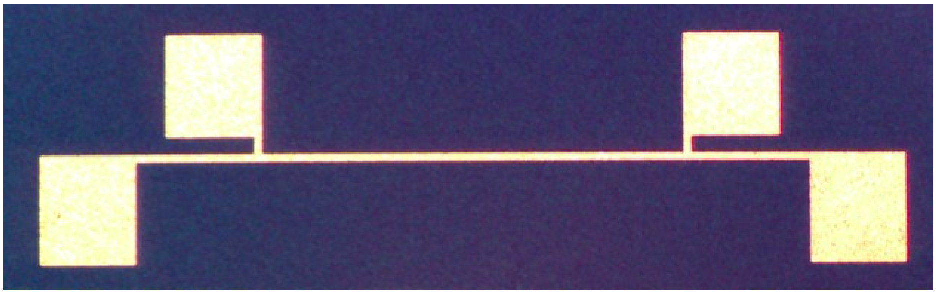

Figure 1.3: An optical image of 3ω heater/thermometer

can measure a temperature by relating the electrical resistance of the thermometer to the temperature, which is dictated by the intrinsic property of a material called temperature coefficient of resistance TCR and can be defined as

$$TCR = \frac{1}{R_o}\frac{dR}{dT} \tag{1.3}$$

In other word, TCR indicates the relative change of resistance when there is a degree of temperature change (unit of TCR is 1/K). Therefore, a material with larger TCR will experience larger change in resistance for a degree change in temperature. A commonly used resistive thermometer especially in thermal measurement research are platinum and gold resistive thin film thermometer since both Pt and Au have relatively high TCR values ($\sim$0.17%/K). Additionally, Pt and Au can be easily fabricated using a standard microfabrication technique such as thin film sputtering and/or electron beam evaporator deposition, and they are typically inert to most chemicals and gases. The thin film resistive thermometer can also act as a heat source via Joule heating. To perform a 3ω measurement, an AC current is applied across the metal strip as shown in Fig.(1.3), where heat flux at the surface can be written as

$$\begin{aligned} Q &= \left[I_o \sin(\omega t)\right]^2 R_o & (1.4) \\ &= I_o^2 R_o \left(1 - \cos^2(\omega t)\right) & (1.5) \\ &= I_o^2 R_o \left(\frac{1}{2} + \frac{\cos(2\omega t)}{2}\right) & (1.6) \\ &= \frac{I_o^2 R_o}{2} + \frac{I_o^2 R_o \cos(2\omega t)}{2}, & (1.7) \end{aligned}$$

where I_o is the applied AC current, R_o is the resistance at an initial temperature, and ω is the frequency of the applied current. Note that the first term on Eq.1.7 is the DC component of joule heating and the second term is the 2ω heat flux component resulted from the same joule heating.

In heat conduction (in accordance to Fourier's law), the heating power or heat flux is directly proportional to temperature. Therefore, the temperature change at the surface detected by the resistive thermometer can be written as:

$$T_{rise} = T_{DC} + T_{2\omega} \cos(2\omega t + \phi) \tag{1.8}$$

From the temperature-resistance relationship associated through TCR, the resistance of the thermometer is then,

$$\begin{aligned} R &= R_o + \frac{dR}{dT}\Delta T_{DC} + \frac{dR}{dT}\Delta T_{2\omega t+\phi}, \text{where} & (1.9) \\ R_{2\omega} &= \frac{dR}{dT}\Delta T_{2\omega} \cos(2\omega t + \phi) & (1.10) \end{aligned}$$

Since the $I_{1\omega}$ is applied to the heater, the voltage across the metal strip (Fig. AA) becomes

$$\begin{aligned} V &= I_o \sin(\omega t)\left(R_o + \frac{dR}{dT}\Delta T_{DC} + \frac{dR}{dT}\Delta T_{2\omega}(2\omega t + \phi)\right) && (1.11) \\ &= I_o \sin(\omega t)\left(R_o + \frac{dR}{dT}\Delta T_{DC}\right) + I_o \sin(\omega t)\frac{dR}{dT}\Delta T_{2\omega}\cos(2\omega t + \phi) && (1.12) \\ &= I_o \sin(\omega t)\left(R_o + \frac{dR}{dT}\Delta T_{DC}\right) \\ &\quad + I_o \frac{dR}{dT}\Delta T_{2\omega}\left(\frac{\sin(3\omega t + \phi) + \sin(\omega t - \phi)}{2}\right) && (1.13) \end{aligned}$$

From Eq.1.13, one can split voltage terms into voltage signal modulated at 1ω and 3ω:

$$\begin{aligned} V_{1\omega} &= I_o \sin(\omega t)\left(R_o + \frac{dR}{dT}\Delta T_{DC}\right) + \frac{1}{2} I_o \frac{dR}{dT}\Delta T_{2\omega}\sin(\omega t - \phi) && (1.14) \\ V_{3\omega} &= \frac{1}{2} I_o \frac{dR}{dT}\Delta T_{2\omega}\sin(3\omega t + \phi) && (1.15) \end{aligned}$$

The voltage modulated at 1ω, $V_{1\omega}$, composes of both ΔT_{DC} and $\Delta T_{2\omega}$, while $V_3\omega$ is only influenced by $\Delta T_{2\omega}$. In other word, $\Delta T_{2\omega}$ can be determined from $V_{3\omega}$ as

$$\begin{aligned} V_{3\omega} &= \frac{1}{2} I_o \frac{dR}{dT}\Delta T_{2\omega} \\ &= \frac{1}{2}\frac{V_{1\omega}}{R_o}\frac{dR}{dT}\Delta T_{2\omega}, && (1.16) \\ \Delta T_{2\omega} &= \frac{2V_{3\omega}}{V_{1\omega}TCR} = T_{rise}. && (1.17) \end{aligned}$$

Therefore, by measuring 3ω voltage signal, one can obtain the average surface temperature at the metal strip to work out thermal analysis to deduce the thermal conductivity of the material of interest. The frequency used in the experiment will determine the thermal penetration depth, which is the depth that the heat can transport through the sample. The thermal penetration depth is defined as:

$$L_{pen} = \sqrt{\frac{\alpha}{\omega_{\text{thermal}}}}, \tag{1.18}$$

where α is the thermal diffusivity and ω_{thermal} is the frequency of the temperature causes by applied heat flux.

Compared to the steady-state method, the advantage of the 3ω method is that one can go to higher frequencies to shorten the thermal penetration depth. As a result, the measurement is more sensitive to the thin-layer regime of interest.

A general 2D heat transfer analytical solution for the temperature rise generated by a heating propagate into N-layers of materials with a finite thickness, derived and reported by Kim et. al. [31], can be formulated as [31, 32]

$$T_{rise} = \frac{-Q}{\pi l \kappa_{y_1}} \int_0^\infty \frac{1}{A_1 B_1} \frac{\sin^2(b\lambda)}{b^2\lambda^2} d\lambda, \tag{1.19}$$

where

$$\begin{aligned} A_{i-1} &= \frac{A_i \frac{k_{y_i} B_i}{k_{y_{i-1}} B_{i-1}} - \tanh(\varphi_{i-1})}{1 - A_i \frac{k_{y_i} B_i}{k_{y_{i-1}} B_{i-1}} \tanh(\varphi_{i-1})} && (1.20) \\ B_i &= \left(\kappa_{xy_i} \lambda^2 + \frac{i2\omega}{\alpha_{y_i}} \right)^{1/2}, && (1.21) \\ \varphi_i &= B_i d_i, && (1.22) \\ k_{xy} &= k_x / k_y, && (1.23) \end{aligned}$$

where T_{rise} is the temperature rise, Q is the power dissipated in the heater, l is the heater's length, b is the heater's half width, d is the layer thickness, n is the total number of layers, κ_x and κ_y are in-plane and cross-plane thermal conductivity, respectively, λ is the variable of integration, and i is the i-th layer of the measured sample with $i = 1$ being the substrate.

The calculated $T_{rise,calc}$ from 2D heat conduction model (Eq.1.19) can then be fitted with the experimental data of $T_{rise,exp}$ as a function of applied current frequency with a known/measured sample thickness, heater's geometry, and heating power, having κ_{sample} as the fitting parameter.

For a thin film measurement (especially if the overall thermal resistance across the film in comparable or smaller than the substrate thermal resistance), a differential technique should be carried out to minimized measurement error due to unknown contributions from the substrate. In differential technique, the T_{rise} of the sample comprises of substrate + insulation layer + all other layers except the thin film of interest) is first measured to determine the thermal conductivity/thermal resistance of the layers under the thin film sample. The controlled thermal properties of the layers below the film is then employed when fitting the 2D heat conduction model with the sample with the thin film. That way, the only fitting parameter for the thin film sample is the $\kappa_{\text{thin film}}$. In other word, this technique essentially resolve the T_{rise} contributed by substrate + insulation layer and the T_{rise} contributed by substrate+insulation layer + thin film. By differentiating these two T_{rise}, we can get the T_{rise} resulted by thin film only.

For a thermal conductivity of a bulk material, an approximated analytical solution can be employed with certain conditions. Assuming the heater is a line source, the material is isotropic, the thermal penetration depth is much larger than the heater's width, and the thickness of the film is much larger than the thermal penetration depth, the thermal conductivity analysis, known as "slope method" can be calculated as [30]

$$\begin{aligned}\kappa_{\text{bulk}} &= -\frac{Q}{2\pi L}\frac{d(\ln(2\omega))}{dT_{rise}}, &(1.24)\\ \kappa_{\text{bulk}} &= -\frac{Q\cdot V_{1\omega}\cdot TCR}{4\pi L}\frac{d(\ln(\omega))}{dV_{3\omega}} &(1.25)\end{aligned}$$

where Q is the heating power, and L is the length of the heater.

Practically, the sample has a finite thickness, which gives rise to error in experimental analysis. In a practical point of view, to use the "slope method", the following criteria must be met in order to have less than 1% of error due to data analysis in comparison to the analysis from the general heat conduction solution when no assumptions are made regarding to the sample's and heater's geometry [32]:

1. the substrate thickness must be at least 5 times longer than the thermal penetration depth

2. the thermal penetration depth times the anisotropic thermal conductivity ratio between cross-plane and in-plane must be 5 times larger than the heater half width.

3. From criteria 1 and 2, if the sample has an isotropic thermal conductivity, the substrate thickness must be at least 25 times longer the heater half width.

Although, measuring 3ω voltage signal is not trivial since the magnitude of $V_{3\omega}$ is typically quiet small compare to $V_{1\omega}$. Therefore, the noise/signal from 1ω voltage can hinder and distort measured the 3ω signal. To measure $V_{3\omega}$ signal accurately, we implemented instrumentation scheme as shown in Fig.(1.4) similar to Refs. [30, 33]. The 3ω heater is connected in series with a precision resistor (low TCR resistor) with a matching resistance. When a current is applied, only the 3ω heater undergoes temperature modulation at 2ω and voltage modulation at 3ω from Joule heating. Note that since the precision resistor has a very small TCR, 3ω signal is negligible. In an ideal case when the resistances between the sample and the precision resistor are identical, through signal differential technique (voltage drop across sample heater minus voltage drop across the precision resistor), the voltage modulates at 1ω will cancel out leaving only the 3ω signal generates by the sample heater. However, in practice, we cannot cancel out $V_{1\omega}$ completely because the resistance is not completely matched. One can uses decade resistors to match the resistance, but it is limited by the resolution of the decade resistors. One can also uses a fixed potentiometer, but the measurement could be tedious for thermal conductivity measurement at a wide range of temperature since at different temperature, the resistance of the heater also changes.

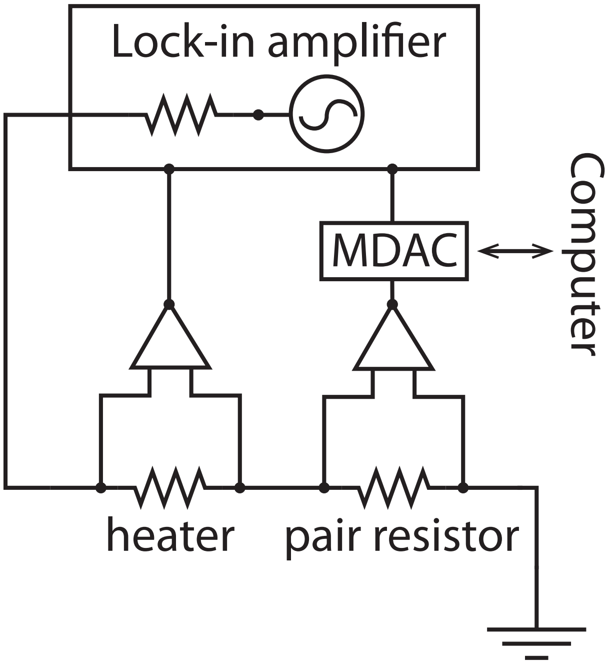

Figure 1.4: A simplified schematic of the 3ω instrumentation set up.

The other option is to use a multiplying digital-to-analog converter (MDAC). What MDAC does is it can adjusted the gain, which will adjust the voltage output across the precision resistor such that it is very close to the voltage drop across the sample. To do this, we first have to measure the first harmonic voltage drop across the sample and across the precision resistor. Then through an automated system (such as Labview), we can digitally adjust the gain of the MDAC such that the output will match the voltage drop across the sample.

Again, since the 3ω voltage signal level is very low, we use lock-in amplifier to minimize the noises from the environment. With a lock-in amplifier, which can 'lock-in' and read voltage at a specific harmonic and frequency and filtering out noises and signal from the environment that is not part of the frequency of interest. In our work, we use Stanford Research SR850 to measure the first and third harmonic voltage drops across the sample and the differential voltage between the sample heater and precision resistor. From these careful instrumentation, we can then measure the low-level signal to examine the thermal transport from bulk material down to sub 100-nm thin film.

For a thin film measurement, few considerations also must be realized to obtain an accurate measurement:

1. The temperature rise contributed by the thin film must be at least comparable, if not higher, than the substrate and insulator. Typically, insulator has a low thermal conductivity and the temperature rise is proportional to the thermal resistance across the film. Therefore, one must make sure than the insulation layer is sufficiently thin such that the thermal resistance of the insulator is smaller or comparable to the thermal resistance of the film of interest. A quick rule of thumb

(zeroth order approximation) is to ensure that the thermal resistance of the film is at least 1/3 of the total thermal resistance. The smaller contribution from the thin film temperature rise will lead to a large uncertainty in the measured κ value.

2. The temperature rise signal resulted from the thermal resistance of the thin film of interest must be larger than the noise.

In this thesis, I employed 3ω technique to examine the thermal transport across a highly mismatched interfaces using Au/Si multilayers as the model system and investigate the thermal property of ion-damaged tungsten layer used as plasma facing components in the fusion reactor.

1.4 Thesis Structure

In this thesis, I will first discuss about thermal transport physics across a highly mismatched materials, namely interfaces between Au and Si by measuring the thermal conductivity of Au/Si multilayers (MLs) (Chapter 2). The thermal conductivity characterization of Au/Si MLs was executed by using the 3ω technique. Understanding thermal transport phenomenon at interfaces is crucial in thermal management of electronic components especially as their size reduces to nanometer scale. Knowing the thermal conductivity of multilayer system and be able to predict will also be advantageous in designs of tunnel junctions, high performance optic mirrors, etc. Therefore, my work also involves in modeling heat transport across interfaces using a diffusive mismatched model in conjunction with a full phonon dispersion (will be discussed in detailed in Chapter 2).

Similar to my work on Au/Si MLs, 3ω technique was performed to characterize the thermal property of ion-damaged tungsten layer that is operated as the plasma facing components (PFCs) material in fusion reactor (Chapter 3). Because the surface of PFCs experienced high-energy particle fluxes, its surface gets damaged by ion bombardment. What we have shown was that the reduction in thermal conductivity due to introduction of surface impurities from particle fluxes can in fact have a very detrimental effect on the thermo-mechanical properties when it undergoes extreme temperature and steady-state/transient heat fluxes. This work sheds lights on the failure mechanisms of the tungsten PFCs.

Besides measuring thermal properties of thin films, many measurements and studies of heat are still limited by the power resolution of a calorimeter. Our goal then is to develop a calorimeter with an unprecedented power resolution beyond the state-of-art calorimeter. We achieved that goal by demonstrating a NbNx-based calorimeter with a power resolution below picowatt level (Chapter 4), where this device can be exploited to understand thermal transport of a materials that were not possible to quantify with the previous calorimeters. In addition, a more detailed analysis on noises and theoretical understandings of calorimeter power resolution are presented in this chapter.

In Chapter 5, from our comprehension in both the theoretical and practical limitations of calorimeters, we then proceed to push the detection limit of a biocalorimeter to measure heat generation from biological samples. We establish a measurement guidelines and designs for a repeatable and accurate measurements of cells metabolic rate. We are able to measure a long-term metabolic rate of a single cell to few cells with an exceptional detection limit, approximately an order of magnitude improvement from the state-of-art biocalorimeter.

Chapter 2

Interfacial Thermal Transport of A Highly Dissimilar Material System

2.1 Introduction

Thermal transport phenomena in multilayers (MLs) have attracted recent interest due to the pronounced effects of interfacial thermal resistance (ITR) on the overall device performance. For instance, the low thermal conductivity (κ) in MLs caused by ITR could be undesirable in tunnel junctions since inefficient heat dissipation across the junction can cause the degradation of the thin barrier coating and adversely affect device performance [34]. Heat dissipation in MLs used in extreme ultraviolet (EUV) and soft X-ray mirrors can also be a concern [35, 36]. On the other hand, a low κ is preferred for applications such as thermal insulation [37] and thermoelectrics [38–40]. Driven by these important implications, several ML systems with a high interfacial density have been measured and show low thermal conductivity values. Examples include $Ge_2Sb_2Te_5$/ZnS:SiO_2 MLs [41], W/Al_2O_3 nanolaminates [37], Ta/TaO$_x$ tunnel junctions [34], CuPC/Ag MLs [42], Mo/Si MLs [35, 36], and very recently, hybrid organic–inorganic zincone thin films [43]. Nanocrystal arrays (NCAs) [44] and organoclay nanolaminates [45] are also other recently researched materials, which exploit high ITR to produce low κ values of 0.1–0.3 W m^{-1}K^{-1} and 0.06–0.1 W m^{-1}K^{-1} respectively.

MLs also serve as a unique model system for investigating thermal transport across solid–solid interfaces, as thermal properties of MLs can be engineered by selecting an appropriate pair of material systems. Several reports on low thermal conductivity ML systems have shown that ITR dominates the overall behavior of cross-plane thermal transport [34, 35, 37, 41–43]. Costescu et al. reported an ultralow κ of $\sim$0.6 W m^{-1}K^{-1} at room temperature in W/Al$_2$O$_3$ nanolaminates with interfacial density of 0.345 nm^{-1} (ref [37]). They also showed that κ of nanolaminates decreases with increasing interfacial density. Here, following Cahill and co-workers [46], we use "ultralow" to describe a κ value lower than what is predicted by the minimum κ model developed by Cahill et al. [47] Recently, Li et al. [35] reported that the phonon is the dominant heat carrier in Mo/Si MLs, while electron-phonon coupling provides additional thermal resistance in the electron thermal pathway in a thin metal layer.

In addition to MLs, several experiments on the ITR of individual interfaces between two dissimilar materials have shown high ITR in highly mismatched materials [48–53]. Specifically, when the phonon is the dominant heat carrier, the ITR is dictated by the contrast in acoustic properties of the pair materials, which can be characterized by the "Debye temperature ratio" (DTR), or the ratio between the high and low Debye temperatures (θ_D) of the corresponding materials. For instance, Lyeo and Cahill [48] showed that interfaces between materials with high DTRs have high

ITRs such as Pb/Si, Bi/Si, Pb/diamond, and Bi/diamond. The thermal conductance of the Bi/hydrogen-terminated diamond, with a DTR of ∼18.7, was measured to be as low as 8.5 MW $m^{-2}K^{-1}$ at room temperature [48], where the interface between TiN/MgO, both with a similar θ_D, was measured to be 2 orders of magnitude higher, ∼700 MW $m^{-2}K^{-1}$ (ref [49]). This suggests that ITR is highly dependent on the DTR. Also, they showed that Bi (semimetal) and Pb (metal), both "soft" materials, yield a similar thermal conductance when paired with the identical "hard" material such as diamond, which suggests that electrons do not play a significant role in interfacial heat transport in those interfaces [48].

Previous literature discussed above suggests that interfaces between materials with a high DTR would possess a high ITR, and if combined with a high interfacial density in MLs, one would expect a low κ. However, the largest DTR in inorganic ML systems measured to date is about 2.1 for W/Al_2O_3 with the lowest κ of 0.53 W $m^{-1}K^{-1}$ (ref [37]). Kim et al. observed a lower κ in GeSbTe based MLs [41], but the low κ is predominately originated from the GeSbTe and ZnS:SiO_2 layers rather than the interfaces (i.e., the observed κ is still higher than the amorphous limit, or not "ultralow"). A very recent study by Yang and co-workers showed an ultralow κ of 0.13 W $m^{-1}K^{-1}$ in organic/inorganic hybrid MLs [43], presumably also caused by the low Debye temperature in the organic component. Therefore, one could potentially further reduce κ in inorganic MLs with one of the layers made of a low-θ_D material.

To see the effect of large ITR on the thermal conductivity of a multilayer system, the interfacial density must be sufficiently high. One of the main challenges in the past in realizing inorganic MLs with high DTRs lies in the difficulty of making ML films with distinct sub-10 nm periodic thickness, especially for soft materials.

In this work, we achieved MLs with a high interfacial density and a high DTR in Au/Si MLs with sub-10 nm periodic thickness. With a DTR of ~3.9 ($\theta_{Au} = 165$ K, $\theta_{Si} = 640$ K) [54], the thermal conductivity of the Au/Si MLs was found to be as low as 0.33 ± 0.04 W $m^{-1}K^{-1}$ at room temperature, significantly lower than the amorphous limit of either Si or Au. These results are much lower than previously measured MLs with a similar interfacial density but lower DTRs, demonstrating that one can achieve ultralow thermal conductivity in inorganic MLs with a high DTR. In addition, in accordance with a prior theoretical prediction by Reddy et al. [55], our experimental data and analysis show that the Debye approximation, which has been commonly used to estimate the ITR, is not valid for materials with a low θ_D, such as Au. Moreover, because both Au and Si are well-studied materials especially with regards to phonon transport, in comparison to a more complex organic/inorganic ML, the Au/Si ML is a simple system (yet challenging to fabricate) with highly mismatched materials for understanding interfacial thermal transport and achieving ultralow thermal conductivity.

2.2 Experimental Method

The Au/Si MLs were grown at room temperature under high vacuum by DC magnetron sputtering onto Si substrates. The base pressure of the chamber was 5×10^{-8} Torr, and the Ar sputtering gas pressure was fixed at 2.5 mTorr. Sputtering rates for Au at 50 W (~2.5 W cm^{-2}) and Si at 100 W (~5 W cm^{-2}) were 1.1 Å s^{-1} and 0.19 Å s^{-1}, determined by X-ray reflectivity measurements of calibration film sample thicknesses. Portions of 2 nm of Ta and 3 nm of Pd were deposited prior to Au and Si to promote adhesion of the multilayer structure to the Si substrate.

Au/Si MLs are composed of 10 periods with a total thickness of 87 nm, where the layer thicknesses of the Au and Si layers are 5.7 and 3.0 nm, respectively. The layer thickness was determined by the dark-field scanning transmission electron microscope (STEM) imaging of the multilayer cross section (Figure 2.1b). The well-formed periodic structure with a highly conformal coating across the substrate is evident from both the STEM images and the X-ray reflectometry (XRR) data shown in Figure 2.1c. Satellite peaks resulting from finite-size effects appear next to the Bragg-like superlattice peaks. This is an indication that the Au–Si interfaces are very smooth and crystalline coherence is maintained through the structure.

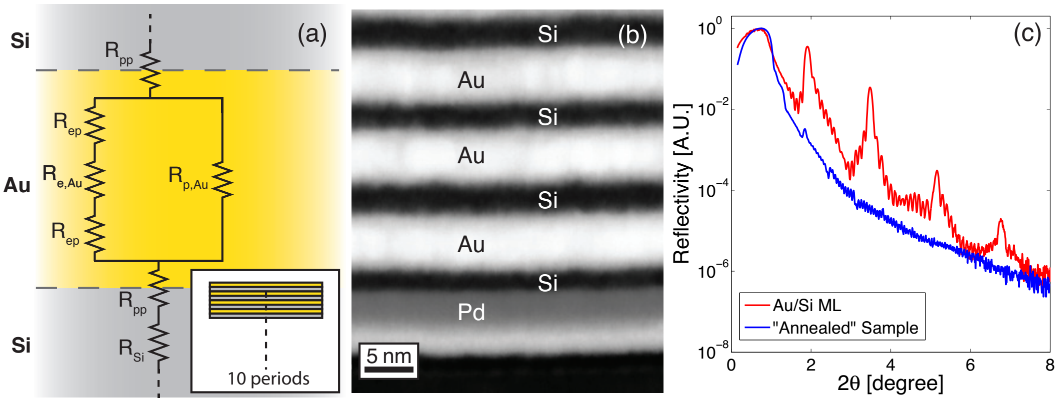

Figure 2.1: (a) A schematic of the thermal resistive network of the Au/Si ML system. Inset: basic schematic of Au/Si MLs. The thermal resistive network composes of thermal resistances of the Si layer (R_{Si}), Au layer, and interfaces (R_{pp}) connected in series. The Au layer has two thermal pathways in parallel: electron and phonon pathways. The electron pathway includes electron–phonon coupling (R_{ep}) and electron-contributed ($R_{\mathrm{e,Au}}$) thermal resistances of Au in series, while the phonon pathway only has a phonon-contributed thermal resistance of Au ($R_{\mathrm{p,Au}}$). (b) Dark-field scanning transmission electron microscope (STEM) images of Au/Si MLs. Each Au and Si layers are 5.7 and 3.0 nm, respectively. (c) X-ray reflectivity (XRR) data of Au/Si ML and the “annealed” sample. Peaks in the XRR plot (c) are an indication of the periodicity in Au/Si ML sample. In the annealed sample, no peaks are shown, which is evidence of degradation of Au–Si interfaces after annealing at 550 K for 24 h.

A frequency domain differential 3ω method was employed [30, 56] to measure the cross-plane κ of the MLs. In a typical 3ω experiment, a thermal wave from Joule heating penetrates into the material, where its penetration depth depends on the thermal diffusivity of the material. Our 3ω heaters were fabricated by the sputtering of Ti (as an adhesion layer) and Au using a stainless steel shadow mask, as shown in Figure 2.3a. To ensure that no electrical current leaks through the measured film, Al2O3 thin film (~235 nm) was deposited as an electrical insulation layer between the heater and the MLs using atomic layer deposition (ALD) at 100 °C. A high-temperature process was avoided because it would anneal the ML samples and cause interdiffusion between layers. In this experiment, we used a current source (Keithley 6221) modulated at 1ω to generate Joule heating on a 3ω metal strip of 2.3 mm long and ~50 µm wide.

The temperature rise across the ML film is isolated from the substrate and insulation layer via a differential method, where the difference in temperature rises between the reference sample (substrate + insulation layer) and the ML sample (substrate + insulation layer + ML film) is taken over a frequency range resulting in a temperature rise contributed by the film. Because the heater width (~50 microm) is much larger than the thickness of the MLs (87 nm), lateral heat spreading is minimal, and the cross-plane measurement is not affected by the anisotropic property of Au/Si ML, as confirmed by our numeric simulation of the heat transfer process. In our experiments, the heater width can vary from sample to sample, leading to slightly different heat fluxes. To accurately determine the temperature rise contributed by the ML film only, a generalized 2D heat conduction model was employed [31, 32]. Note that simply normalizing the temperature rise to account for heater width variation is not strictly accurate since heater width b is within the integral part of the frequency domain 2D heat conduction equation [31]. In this 3ω scheme using 2D heat conduction analysis, the reference sample is measured to obtain the temperature rise as a function of frequency. The heat conduction model is then applied to find κ of both substrate and insulation layers by fitting the model with the measured temperature rise of reference sample (Figure 2.2). These fitted parameters are then applied to the ML samples, leaving only one fitting parameter, κ_{ML}, as shown in Figure 2.3b.

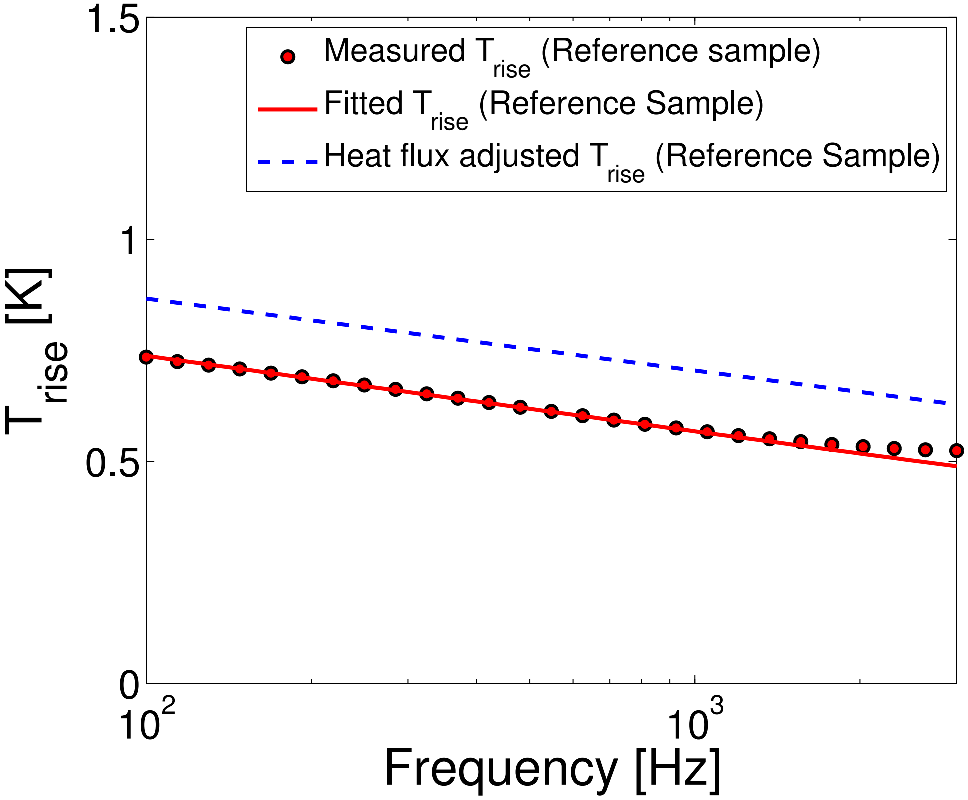

Figure 2.2: Plot of temperature rise T_{rise} as a function of frequency for reference sample (substrate + insulation layer). The red dots are the measured T_{rise} and red line is the fitted T_{rise} using 2D heat conduction model. The blue dash line represents the temperature rise of the reference sample if the heat flux of the corresponding ML sample's heater is used (ML sample = substrate + insulation layer + ML film). The heat flux depends on joule heating power, length and width of the heater.

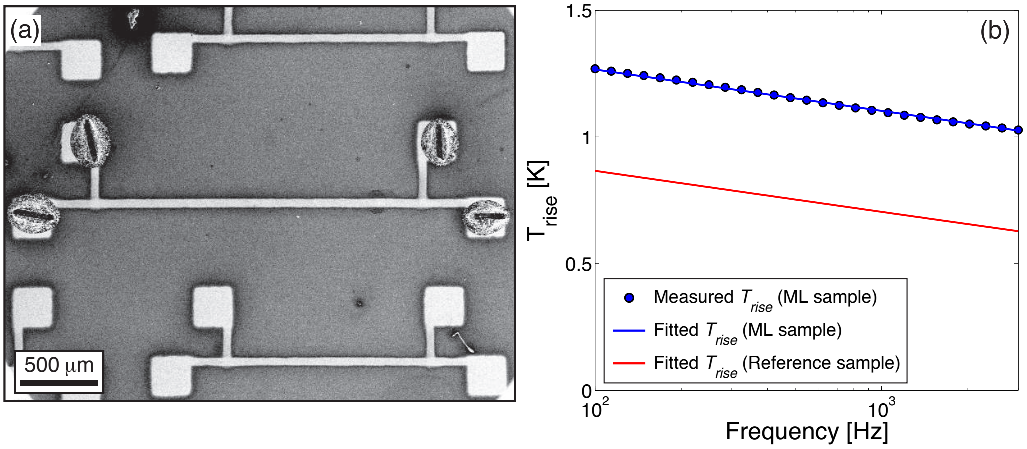

Figure 2.3: (a) A scanning electron microscopic (SEM) image of 3ω heater for κ measurement. (b) Plot of temperature rise (T_{rise}) as a function of frequency obtained from 3ω measurement. Blue dots are an example of measured T_{rise} data of the ML sample, while the blue and red lines are the fitted T_{rise} from the 2D heat conduction model of the reference and ML samples, respectively. The difference between the blue and red lines represents the T_{rise} contributed by the ML film only.

This procedure assumes that the thicknesses and thermal conductivities of substrate and insulation layers in both the reference and the ML samples are identical. Therefore, to minimize variations of these parameters between reference and ML samples, all sample preparations and fabrication processes underwent the same conditions at the same time. The additional interfacial thermal resistances between the insulation layer and the ML film as well as between the ML film and its wetting layer are omitted in the experimental data analysis for simplicity since these resistances are much smaller than the total thermal resistance of the ML film. Within the framework of MLs measurements, extra interfacial resistances can come from: 1) the interface between the adhesion film under the insulation layer (Ti) and the top surface of the ML film (Au) and 2) the interface between the wetting layer (Pd) and the bottom surface of the ML film (Si), where each contact has a Debye temperature ratio (DTR) between 2.3 – 2.5. This range of DTR typically corresponds to interface thermal conductance higher than 100 MW $m^{-2}K^{-1}$. In addition, since differential method is employed, the reference sample will also have additional interface resistances, which to a large extend will cancel out with the additional resistances from the ML samples. To examine the effect of these additional interface resistances in the worst-case scenario, the 2D heat conduction model is used to compare the temperature rise, T_{rise}, of the ML sample with and without the additional interfacial resistances as shown in Figure S2 assuming no addition interfacial resistances are from the reference sample. In other word, no additional canceling in T_{rise} from the reference sample is included. Here, two interfacial resistances, each with interfacial thermal conductance equal to 100 MW $m^{-2}K^{-1}$, are applied to the temperature rise of the fitted Au/Si ML sample at 300 K. The model shows that the additional interfacial resistances account for less than 2% of the total increased T_{rise}, which corresponds to 5.1% in measured κ and is still within the uncertainty of our measured κ. Note that even for Au/Si with a DTR of ∼4, the extracted thermal conductance is approximately 100 MW $m^{-2}K^{-1}$. Therefore, the contribution due to the contact resistances in the ML sample should be even less and is, consequently, omitted in the experimental data analysis used to calculate the thermal conductivity of the ML.

Also, κ measurements were prepared and performed right after MLs fabrication since Au/Si interfaces can deteriorate over time [57, 58]. This is confirmed with the XRR data of freshly fabricated Au/Si ML (red line in Figure 2.5), which shows clear peaks indicating distinct periodic layers between Au and Si. By annealing the Au/Si ML at 550 K in Ar for 24 hours, peaks showing periodicity are absent (blue line in Figure 2.5). In addition, an evidence of the deterioration of the Au/Si ML with time is shown in a 2-year old Au/Si ML (green) where the peaks have broadened and

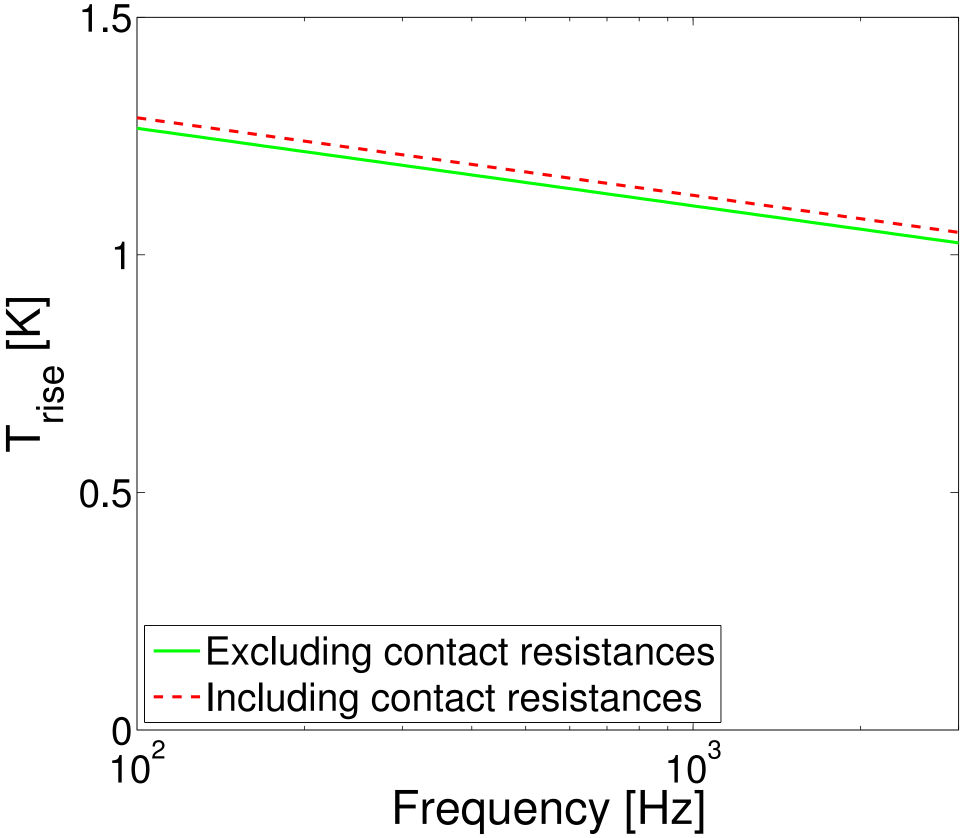

Figure 2.4: A comparison plot of temperature rise T_{rise} as a function of frequency for ML samples when including and excluding additional interfacial resistance in the data analysis. The green solid line is the T_{rise} of the ML sample without considering the interfacial resistances between the ML film and insulation layer/wetting layers. The red dashed line corresponds to the T_{rise} of the ML sample if interfacial resistances are included. The 2D conduction model shows less than 2% increase in T_{rise}.

are less pronounced (Figure 2.5). Therefore, to capture accurate thermal transport properties of ML film with distinct interfaces between Au and Si layers, thermal conductivity measurements were performed right after ML fabrication.

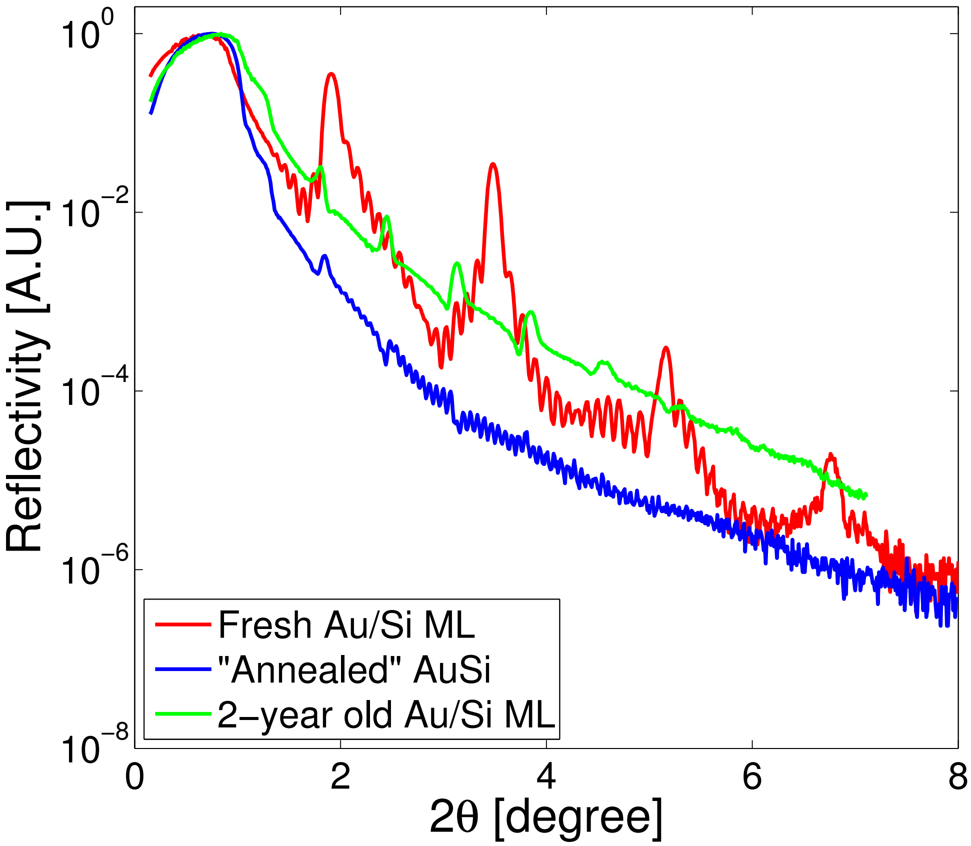

Figure 2.5: XRR data of fresh Au/Si ML (red), "annealed" AuSi (blue), and 2 years old Au/Si ML (green).

2.3 Results

The measured temperature dependent cross-plane thermal conductivity data on Au/Si MLs are summarized in Figure 2.6. ML samples #1 and #2 are from different locations of the same wafer; the measured κ between these two samples are similar, thereby verifying that the Au/Si MLs are homogeneous across the wafer.

At room temperature, the κ of the Au/Si MLs is 0.33 ± 0.04 W m^{-1}K^{-1}, which is even lower than their amorphous thin film counterparts (amorphous lattice thermal conductivity κ_L for Si and Au are 1.05–1.6 and 0.49 W m^{-1}K^{-1}, respectively

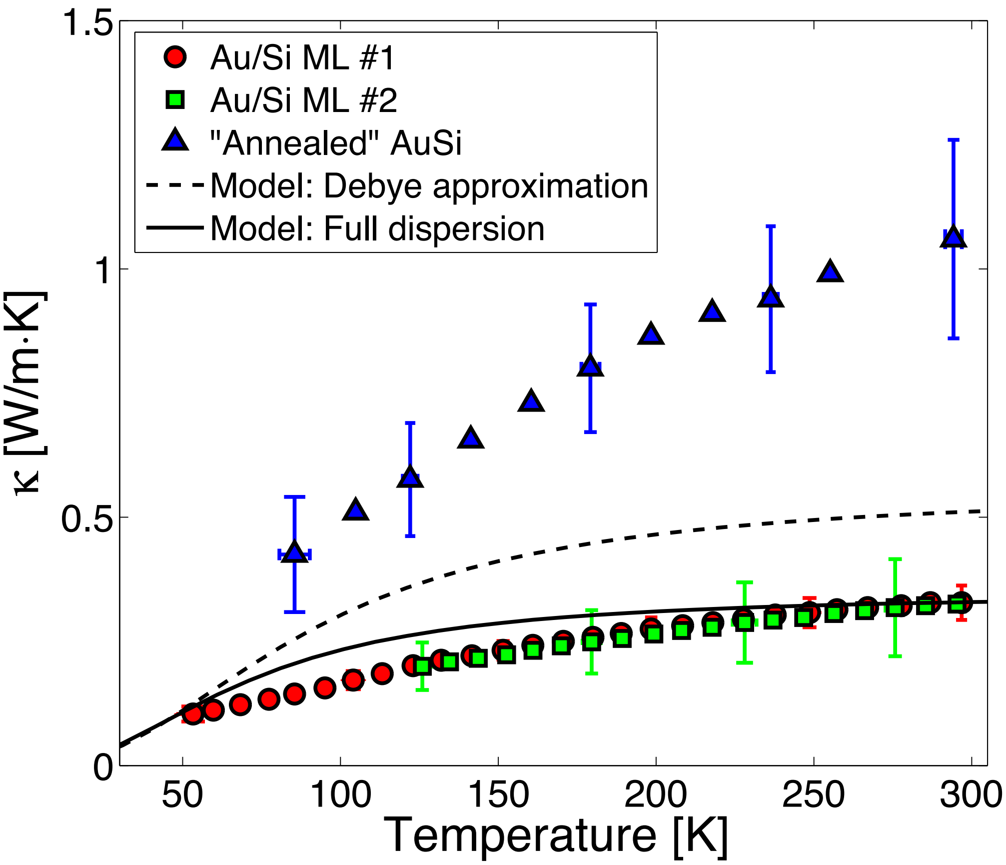

Figure 2.6: Thermal conductivity of Au/Si ML (red circles and green squares) and the "annealed" Au-Si (blue triangle) samples as a function of temperature. A much higher thermal conductivity in the annealed sample, in which the interfaces were absent, demonstrates the importance of thermal boundary resistance to the thermal transport in MLs. The modeling result based on the full phonon dispersion (solid line) agrees with the experimental data much better than that based on the Debye approximation (dash line), suggesting the advantage of using full dispersion for low Debye temperature materials such as Au.

[38, 47, 59–61]). The κ of Au/Si MLs retains an increasing temperature tendency from 50 to 300 K, similar to previously observed measurements on interfacial thermal conductance [48, 49].

The observed low κ in the MLs can be associated with the high ITR between the Au and Si interfaces. To elucidate this premise, another 3ω measurement was performed on a sample of an identical Au/Si ML that has been annealed at high temperature. The annealing process was performed in the Ar environment at 550 K for 24 h, which is sufficient to result in interdiffusion between layers or alloy formation at the interface [57, 58]. As a result, the distinct interfaces between Au and Si in the "annealed" sample are eliminated, as confirmed by the XRR data, where the immense dampening of the Bragg-like peaks exhibits the degradation of the ML (Figure 2.1c). At room temperature, κ of the annealed sample is 1.06 ± 0.20 W $\mathrm{m}^{-1}\mathrm{K}^{-1}$, which is more than three times larger than the MLs. An increase in κ after annealing indicates that high thermal boundary resistance in the original MLs is prompted by the distinct interfaces between Au and Si.

2.4 Modeling thermal properties of Au/Si multilayers

To understand the thermal data of the MLs, a basic thermal network model is implemented to elucidate thermal transport mechanism in the ML structure as shown in Figure 2.1a. The model is simplified by neglecting the Au/Si interdiffusive layer. The effective thermal conductivity of the film then can be described as

$$\kappa = \frac{d_{\mathrm{Au}} + d_{\mathrm{Si}}}{R_{\mathrm{unit}}} \tag{2.1}$$

in which

$$R_{\mathrm{unit}} = R_{\mathrm{Si}} + \left(\frac{1}{R_{\mathrm{ep}} + d/\kappa_{\mathrm{e}}} + \frac{1}{R_{\mathrm{p,Au}}} \right)^{-1} + 2R_{\mathrm{pp}} \tag{2.2}$$

where R_{Si} is the thermal resistance from the Si layer, R_{ep} is the thermal resistance from electron-phonon coupling within the Au layer, κ_{e} is the electron-contributed thermal conductivity of the Au layer, $R_{\mathrm{p,Au}}$ is the phonon-contributed thermal resistance of Au, and R_{pp} is the interfacial thermal resistance (ITR) between Au and Si layers. Equation 2 is an approximation for the ITR, which assumes that the ITR originating from phonons from Au to Si and Si to Au is identical, hence the term $2R_{\mathrm{pp}}$. It is worth mentioning that this assumption is not always accurate since phonon transport across a material interface is asymmetric in nature, which could result in different ITRs as explained by Li et al. [62]

Based on equations (2.1) and (2.2), the ITR of the Au-Si interface (R_{pp}) at different temperatures can be indirectly extracted from the measured Au/Si ML κ values, which can be written as

$$h_{\mathrm{pp,extracted}} = 2\left(\frac{d_{\mathrm{total}}/\kappa_{\mathrm{measured}}}{N_{\mathrm{periods}}} - R_{\mathrm{Si}} - R_{\mathrm{Au}}\right)^{-1} \tag{2.3}$$

where N_{periods} is the total number of periods, d_{total} is the thickness of the ML film, R_{Si} is the calculated thermal resistance of a Si layer, and R_{Au} is the thermal resistance of a Au layer contributed by both electron and phonon pathways

Because both Au and Si layers were sputtered to make thin film, phonon-contributed thermal resistance for an individual thin film layer (R_{Si} and $R_{\mathrm{p,Au}}$) were calculated based on minimum thermal conductivity model for amorphous solid proposed by Cahill [47, 63], which is described as

$$R_{\mathrm{p,Au\ or\ Si}} = \frac{d}{\kappa_{\mathrm{min}}} \tag{2.4}$$

$$\kappa_{\min} = \left(\frac{\pi}{6}\right)^{1/3} k_{\mathrm{B}}\eta^{2/3} \sum_j v_j \left(\frac{T}{\theta_j}\right)^2 \int_0^{\theta_j/T} \frac{x^3 \mathrm{e}^x}{\left(\mathrm{e}^x - 1\right)^2} dx \tag{2.5}$$

$$\theta_j = v_j \left(\frac{\hbar}{k_B}\right) \left(6\pi^2\eta\right)^{1/3} \tag{2.6}$$

, where $\kappa_{\min}$ is the phonon-contributed thermal conductivity of Au or Si, k_{B} is the Boltzmann constant, $\hbar$ is Planck's constant, η is atomic volume, v_j is the group velocity of mode j, and θ is the cutoff frequency in each mode.

To evaluate thermal resistance from electron-phonon coupling of the metal layer, a commonly referenced two-temperature model (TTM) is applied [64]. From Fourier based energy balance, the thermal conductance due to electron energy exchange with phonons can be estimated as $h_{\mathrm{ep}} = \sqrt{Gk_{\mathrm{p,Au}}}$, where G is the electron cooling rate [65]. However, this expression for electron-phonon coupling conductance does not consider size effect of the thin metal. A more rigorous approach, which accounts for finite thickness of the film was presented by Ordonez-Miranda et al. [66]. Even though the thickness of our Au is comparable to the intrinsic electron-phonon coupling length [66], since interface thermal resistance of Au/Si dominates, a simple expression for G is sufficient. Different G values reported for Au at room temperature were between $\sim 2\times10^{16}$ to 4×10^{16} W $\mathrm{m}^{-3}\mathrm{K}^{-1}$ [67–71]. In this paper, a temperature dependent functional form for electron-phonon coupling parameter proposed by Kaganov et al. is applied [72]. Such functional form was fitted and agreed well with the reported experimental value of Au's electron-phonon coupling parameter as demonstrated by Wang and Cahill's work [71], in which

$$G\left(T\right)=g_o\left[\left(\frac{20T^4}{\theta^4}\int_0^{\theta/T}\frac{x^4}{\mathrm{e}^x-1}dx\right)-\left(\frac{4\left(\theta/T\right)}{\mathrm{e}^{\left(\theta/T\right)}-1}\right)\right] \tag{2.7}$$

where g_o is the high temperature limit of electron-phonon coupling rate and θ is Debye temperature of metal. In this paper, G is 2.8 $\times 10^{16}$ W m^{-3}K^{-1} at room temperature. Because electron-phonon coupling does not contribute significantly, using ranges of G values measured by different authors at room temperature only vary the final κ to about ±2%. Li et al. also have shown that two temperature model provides a good approximation comparing to the numerical solutions using the phonon Boltzmann transport equation [35]. Therefore, the two-temperature model with a simplistic functional form for G should be adequate to capture electron-phonon coupling behavior in metal layer at different temperatures.

Since R_{Si} and R_{Au} are based on theoretical calculations, the extracted h_{pp} summarized in Figure 2.7a should be taken as an estimation. Our Au/Si ML shows a similar thermal boundary conductance compared to previous Au/Si experiments [53, 73] and has similar temperature dependency as in other reported works using different material systems [48, 49, 74]. Considering all thermal transport pathways, the ITR between Au and Si has the highest contribution, approximately ~60–75% to the total thermal resistance throughout the measured temperature range (Figure 2.7b). Within the Au layer, free electrons, which are the main heat carrier for bulk Au, are suppressed in the ML, and phonons in the Au film play a more dominant role in heat transport. The majority of thermal resistance in the electron pathway results from electron–phonon coupling ($R_{\mathrm{e}} \ll R_{\mathrm{ep}}$), and its thermal resistance is comparable to the phonon pathway in Au layer. Because Au is regarded as a "soft" material from a phonon standpoint, it inherently has low thermal conductivity if electrons play no role in heat transport, even lower than Si. Therefore, due to suppression of electron transport, there is no thermal pathway that can induce high thermal conduction as observed in bulk Au. To sum up, the combination of phonon-dominated transport in each layer and especially high ITR leads to an ultralow κ in the Au/Si ML. By degrading the interfaces in the annealed sample, the effect of ITR is substantially lessened and the κ of the "annealed" AuSi evidently enhanced.

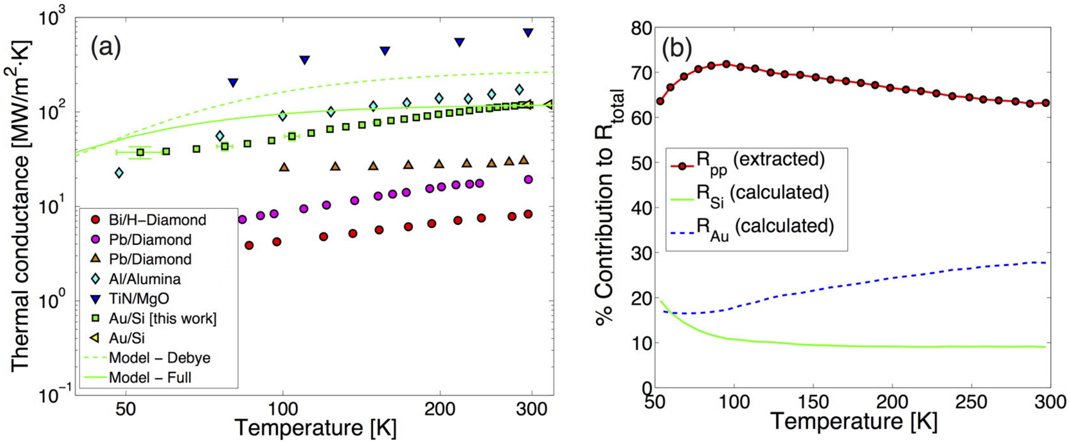

Figure 2.7: (a) Temperature-dependent data of previously measured interfacial thermal conductance in comparison to our extracted interface thermal conductance for Au/Si, which demonstrates a consistent temperature trend as in previous works (refs [48, 49, 73, 74]). The DTR values for Bi/diamond, Al/Al_2O_3, and TiN/MgO are approximately 18.7, 2.1, and 1.6 respectively, while Au/Si has a DTR value of 3.9. As anticipated, the ITR of Au/Si lies between Al/Al_2O_3 and Bi/diamond. The dashed and solid green lines are the thermal conductance of the Au/Si interface calculated by DMM using the Debye approximation and full dispersion, respectively. The temperature-dependent trend for DMM is different from the measured conductance with a larger deviation at lower temperatures, which consequently manifests in the limitation of DMM in predicting ITR. (b) The relative contribution of ITR (R_{pp}), Si layer (R_{Si}), and Au layer (R_{Au}) to the total resistance for each Au/Si ML unit cell at various measured temperature points. The ITR of Au/Si is extracted from the measured κ of Au/Si ML and the calculated Si and Au film's thermal resistance as presented in this paper. Here, ITR is the primary contributor to the total thermal resistance and dominates the transport across the ML throughout the temperature ranges.

We now focus on the understanding of the ITR and its comparison with the experimental data since it dominates the thermal transport in MLs [35,37,66,67]. The diffusive mismatch model (DMM), first proposed by Swartz and Pohl [51], was used to model the thermal boundary conductance. A general form of thermal boundary conductance from materials A to B is defined as [51]

$$\begin{aligned} h_{\mathrm{A}\to\mathrm{B}} &= \frac{\partial q_{\mathrm{A}\to\mathrm{B}}}{\partial T} \\ &= \frac{1}{4}\sum_{j=1}^{3}\int_{\omega} v_{\mathrm{A},j}(\omega)\alpha_{\mathrm{A}\to\mathrm{B}}(\omega)\hbar\omega \mathrm{DOS}_{\mathrm{A}}(\omega)\frac{\partial f_o}{\partial T}d\omega \end{aligned} \tag{2.8}$$

where h is the thermal boundary conductance, v_j is group velocity of mode j, $\hbar$ is Planck's constant, DOS is the phonon density of states, and f_o is the Bose-Einstein distribution function. At the interface between material A and B following the detailed balance, phonon flux from A to B and from B to A must be equal. Phonons from A can either scatter back to A or transmit through B at the interface basing on the transmission probability. Different assumptions on the behavior of phonons as they interact with the interface lead to various formalisms for the transmission probability [51, 75–78]. Within the framework of DMM, it is assumed that, once phonons hit the interface, they become completely diffusive [51]. In another word, phonons lose their memories in both directions and polarizations at the interface. Therefore, from the detailed balance $h_{\mathrm{A}\to\mathrm{B}} = h_{\mathrm{B}\to\mathrm{A}}$, the transmission probability can be defined as [51, 55]

$$\alpha_{\mathrm{A}\to\mathrm{B}}(\omega') = \frac{\sum_j v_{\mathrm{B}}(\omega')\mathrm{DOS}_{\mathrm{B}}\delta_{\omega,\omega'}}{\sum_j v_{\mathrm{A}}(\omega')\mathrm{DOS}_{\mathrm{A}}\delta_{\omega,\omega'} + \sum_j v_{\mathrm{B}}(\omega')\delta_{\omega,\omega'}} \tag{2.9}$$

where $\delta_{\omega,\omega'}$ is the Kronecker delta, v is the group velocity for material A or B, and

DOS is the density of states of material A or B. From equations (2.8) and (2.9), the thermal boundary conductance can be calculated with known phonon dispersion relations.

For DMM calculations, phonon dispersion relations are needed for Au and Si. The Debye approximation, which is a linear approximation of phonon dispersion relation, has been used extensively due to its simplicity [35, 37, 48, 49]. However, the Debye approximation is only accurate near the center of the Brillouin zone (BZ) and deviates significantly at the edge of BZ. Hence, such an estimation is only appropriate at temperatures much lower that the Debye temperature of the material considered. Reddy et al. pointed out the limitation of the Debye approximation and the importance of using full dispersion in DMM calculations [55]. Cahill et al. [37] and others also pointed out that the use of the Debye approximation may lead to an overestimation of the calculated interfacial conductance. In our Au/Si MLs, Au has a very low θ_D ($\theta_D = 165$ K) when compared to most metals. Therefore, Debye approximation could be inaccurate for Au/Si MLs especially at room temperature.

To assess the validity of the Debye approximation, we calculate thermal conductance values using the DMM model with both Debye approximation and full dispersion and compare them with the experimental data. The full phonon dispersion relation is modeled using the Born-von Karman lattice dynamical model [55, 79]. The vibrational properties (eigenfrequencies and eigenvectors at different wavevectors) can then be solved from the secular equation, $|D(\vec{q}) - m\omega^2| = 0$, with known dynamical matrices. The dynamical matrices for the diamond cubic structure derived by Herman [80] and fcc metal derived by Thakur and Singh [81] were applied to calculate bulk (3D) phonon vibrational spectra of Si [82] and Au, respectively. The assumption in using bulk phonon dispersion may not be completely valid at lower temperatures where the phonon wavelengths are longer, which may be a factor contributing to the discrepancy between the model and experimental data at low temperature as we shall see later. Full phonon dispersions calculated in this paper were also verified with previous experimental results (Ref. [83] for Au and Ref. [84] for Si) as shown in Figure 2.8. The comparisons also shows the validity of force constants used in lattice dynamic calculation to determine full dispersion relation.

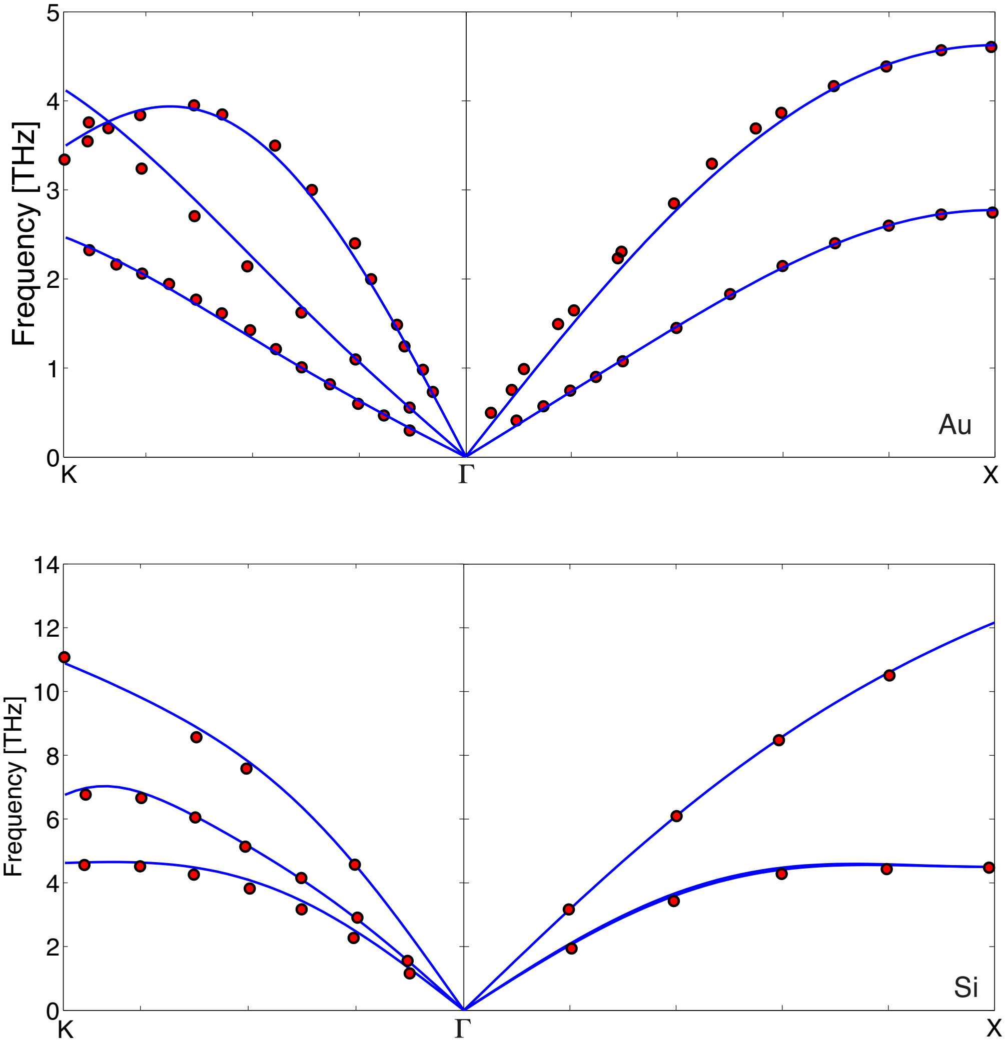

Figure 2.8: Phonon dispersion relation of Au and Si

It should be noted that by using lattice dynamics to calculate phonon dispersion relation, one must assume that the material structure in consideration has a perfect crystallinity, whereas the Au and Si layers of the MLs studied here are amorphous. Therefore, this is a big assumption made in the present model. Nevertheless, in most materials, the DOS of crystallized structures and their amorphous forms are fairly comparable. For instance, in amorphous Si [85], the shape of the DOS widens, and the peaks at different frequencies are not as pronounced as in its crystal structure [86, 87]. Therefore, the overlapping region when considering the transmission probability across the interface could be altered when using the crystalline structure. On the other hand, the average speed of sound of crystalline Si and amorphous Si are similar when the amorphous Si is fully dense [88–91]. The density of an amorphous film relies heavily on the material preparation methods, where the introduction of voids and porosity reduces the material's speed of sound and can range from 53% (by sputtering) [92] to ∼100% (by glow discharge with density nearly identical to crystalline Si [88]) of the speed of sound of crystalline Si [88–91]. In addition, the speed of sound of 2–5 nm thin amorphous Si prepared by ion-beam sputtering to make Si/Mo MLs was measured indirectly and yielded 98% of its bulk's speed of sound [93]. The similar speed of sound between amorphous and crystalline Si suggests indifferences in group velocity in low-frequency phonons but could be different in the high-frequency regime. Nevertheless, one can also recognize that the phonon group velocity and DOS are closely related, as both are directly related to the derivative of the dispersion relations ($\mathrm{d}\omega/\mathrm{d}k$). The fact that DOS between a-Si and c-Si are similar to each other implies that the phonon group velocities between the two are probably similar. Since there is no work regarding the vibrational spectrum and group velocity of amorphous

Au to our knowledge, we assume that the same phenomenon for Si also applies for phonons in Au. Even though the crystalline phonon dispersion cannot completely depict amorphous behavior of the thin film materials of interest, we believe that the full dispersion calculated from the lattice dynamics can still serve as a good approximation for the studied materials and is a more realistic representation compared to the Debye approximation.

From the dispersion relation, group velocity ($v_g = \partial\omega/\partial q$) and DOS are calculated numerically, as shown in Figure 2.9. At very low frequency, the Debye model gives a good approximation for group velocity and DOS in comparison to using full phonon dispersion.

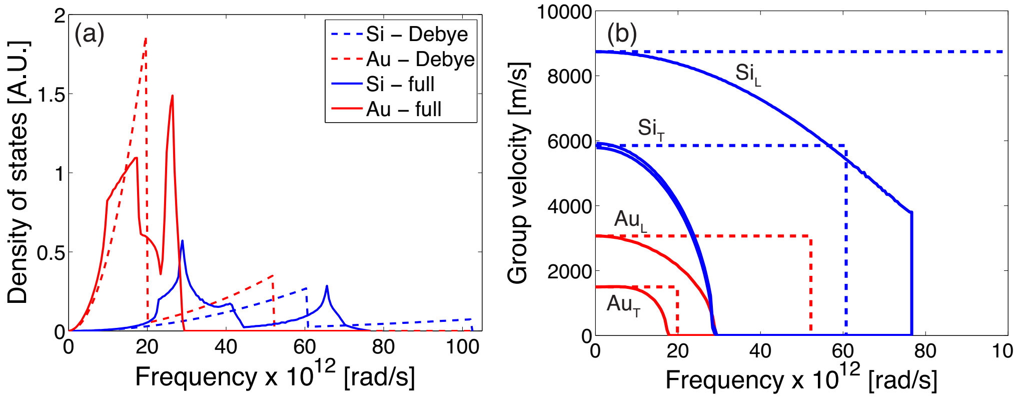

Figure 2.9: Phonon DOS (a) and group velocities (b) with respect to phonon frequency in Au (red) and Si (blue), respectively. Solid and dashed lines are based on full phonon dispersion and the Debye approximation, respectively, which agree well in both DOS and group velocity at low frequency but diverge at high frequency.

Hence, at low temperature where low frequency dominates phonon transport, both Debye approximation and full phonon dispersion are in good agreement with each other. However, at a higher frequency away from the acoustic region in BZ, full dispersion shows a lower group velocity compared to the Debye model, as evidenced in Figure 2.9b, which leads to overestimation in the thermal boundary conductance in the Debye model. In addition, discrepancies in DOS between the Debye and full phonon dispersion models are illustrated in Figure 2.9a. From the full phonon dispersion, van Hove singularities provoked by critical points in BZ are observed at different frequencies and does not follow parabolic trend as in the Debye approximation. From the differences in the calculated DOS and group velocity, we expect that the Debye approximation would overestimate the thermal boundary conductance between Au-Si interfaces. Therefore, using full dispersion to calculate thermal boundary conductance could explain the experimental data better.

By including the thermal conductivity of the Au and Si layers (as mentioned previously), along with the calculated interfacial thermal conductance, we can model the total thermal resistance and the effective thermal conductivity of the MLs based on eq (2.1). Figure 2.6 shows the modeled effective thermal conductivities at different temperatures calculated for Au/Si MLs compared with the measured data. As expected, the Debye approximation is comparable to the full dispersion model at low temperature but overestimates the thermal conductivity at higher temperature by up to 1.6 times at room temperature. The modeling results with the full dispersion shows much better agreement with the experimental data for the entire temperature range of 30–300 K. It should be noted that no free parameter was employed in the calculation using DMM and the full dispersion. Therefore, this analysis indicates that the full dispersion, rather than the Debye model, could better capture the thermal transport across the Au/Si interface where Au has a low Debye temperature.

2.5 Discussions

Below 200 K, there are fairly large discrepancies between the DMM and experimental results. These discrepancies can be interpreted by considering the limitations and assumptions made in the present DMM model. First, as discussed earlier, dispersion relations of crystalline materials are used to model amorphous materials. Second, the model assumes perfect Au–Si scattering interfaces with no interdiffusion. However, roughness, imperfection, and bond strength between Au–Si in our fabricated MLs, which are not captured in the model, can contribute differently to the total thermal resistance [42, 53, 94]. Zhou et al. [94] carried out extensive modeling on the effect of interfacial morphology on ITR and found that interfacial roughness and diffused interface increase the interfacial conductance due to increased interface areas and the "phonon bridging" effect, respectively, whereas in our experiments, the thermal conductivity data below 200 K is lower than what is predicted by the DMM. This suggests that interface roughness or diffused interface is unlikely the cause of the discrepancy, as also evidenced by the clear interfaces observed in the TEM images and XRR peaks shown in Figure 2.1b and 2.1c. However, defects, such as impurities and voids, could still play a role as defect scattering is typically more pronounced in the intermediate temperature region. Third, DMM inherently assumes diffusive thermal transport across interfaces, which is not always true. High-frequency phonons, as opposed to low-frequency phonons, are more likely to be subject to diffusive processes; i.e., not all phonons participate in diffusive scattering. Since DMM stems from the diffusive behavior of phonons across an interface, it provides a better depiction of phonon transport behavior at higher temperatures, where high-frequency phonons play a larger role. Therefore, a more substantial difference between experimental results and DMM in the low-temperature regime, where low-frequency phonons dominate, is observed. Furthermore, Landry and McGaughey [95], based on both theoretical calculations and molecular dynamics (MD), showed that DMM could overestimate the interfacial thermal conductance if there is nondiffusive phonon scattering at interfaces between mismatched materials (Si and "heavy" Si in their case). In addition, the DMM model discussed here does not account for the inelastic scattering of phonons at interfaces, which is typically more pronounced at temperature higher than the material's Debye temperature. In our case of Au/Si ML, since the Debye temperature of Au is low, inelastic scatterings could play a role at an even temperature lower than room temperature. According to MD simulations from Landry and McGaughey's work and others [77, 95, 96] thermal conductivity would increase monotonically with temperature in MLs at high temperature, whereas the elastic DMM model would lead to a plateau of κ vs T (see Figure 2.6). The temperature dependence of our experimental data seems to support the argument of inelastic phonon transmission. However, a further systemic study is warranted to further explore this point. Other than molecular dynamics simulations or analytical models, if the thickness of each layer in the ML structure is very thin, a quantum approach can also provide important insight regarding the underlying physics of metal/dielectric interfacial thermal resistances that the classical approach inadequately elucidates [97, 98].

Finally, to place our measured thermal conductivity of the MLs in perspective, we summarized the thermal conductivity values of various inorganic MLs reported to date, in corresponding to interface density, as shown in Figure 2.10.

The color scale of each data point indicates the magnitude of DTR in accordance to the colorbar. For a particular interface density system, the interface of

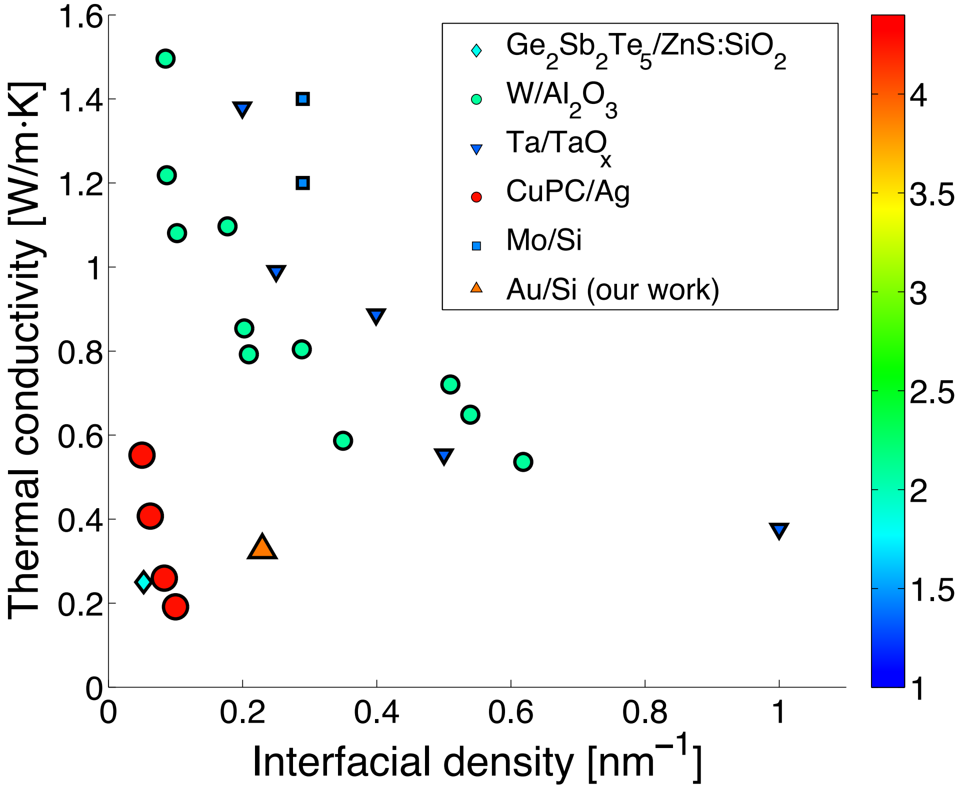

Figure 2.10: Summary of κ values for selected MLs with the corresponding interfacial densities. Data are taken from refs [34, 35, 37, 41]. The magnitude of Debye temperature ratio (DTR) of each data point is shown in the color bar, where red and blue indicate highest and lowest DTRs, respectively. As interfacial density increases, κ of MLs tends to decrease. With the same interfacial density, a material system with higher DTR tends to a have lower κ. One exception is GST/ZnS:SiO_2 ML where the individual layers possess an intrinsically low κ. The Au/Si ML in this work has the highest DTR among inorganic MLs measured to date and consequently shows a much lower κ compared to other MLs with the same interfacial density.

materials with larger DTR tends to have lower thermal conductivity. One exception is for GST/ZnO:SiO_2 where the respective layers already possess low intrinsic thermal conductivity [41]. For an interface density of ~0.2 nm^{-1}, our Au/Si MLs, having the highest DTR, exhibit the lowest thermal conductivity. Based on the trend shown in Figure 2.10, it is expected that even lower thermal conductivity can be expected in MLs with higher interfacial density and larger DTR as previously supported by both experimental and theoretical works [34, 37, 41, 42, 62, 97].

2.6 Conclusion

In conclusion, we demonstrated ultralow thermal conductivity in MLs made of Au and Si with a high interfacial density of approximately 0.2 nm^{-1} (the Au and Si layers are 5.7 and 3.0 nm, respectively). With a DTR of ∼3.9, the Au/Si MLs represent the highest mismatched system in inorganic MLs measured to date. The measured thermal conductivity of 0.33 ± 0.04 W $\text{m}^{-1}\text{K}^{-1}$ at room temperature is significantly lower than the amorphous limit of either Si or Au and is also much lower than previously measured MLs with similar interfacial density but lower Debye temperature ratios. The low Debye temperature of Au prompted us to examine the validity of the Debye approximation used in the theoretical analysis of interfacial thermal conductance. Our assessments suggests, in accordance with prior theoretical predictions, that full phonon dispersion could provide a better depiction of the measured interfacial thermal resistance in comparison to the Debye model. This work suggests that MLs with highly dissimilar Debye temperatures represent a promising approach to engineer thermal transport in inorganic MLs and achieve ultralow thermal conductivity.

Chapter 2, in part, is a reprint of the material in Nanoletters, 2014, Edward Dechaumphai, Dylan Lu, Jimmy J. Kan, Jaeyun Moon, Eric E. Fullerton, Zhaowei Lie, and Renkun Chen. The dissertation author was the primary investigator and the first author of this paper.

Chapter 3

Near-Surface Thermal Characterization of Plasma Facing Components

3.1 Introduction

Plasma facing components (PFCs), such as tungsten (W), are expected to be exposed to both steady-state and transient thermal loads [99–105]. The power density of the steady-state heat loads can be as high as 5–10 MW m^{-2}, while that of the transient heat loads is anticipated to be up to 10 GW m^{-2} for short durations of a few ms during plasma disruptions and $\sim$0.5 ms for edge localized modes [100, 101]. These large thermal loads inevitably lead to an increased surface temperature rise (T_s) on the PFC, measured relative to the temperature of the heat sink, as shown schematically in Fig.(3.1a). For steady-state heat loads, T_s depends on the heat flux (Q_{ss}), thermal conductivity (κ) of the PFC (e.g., W), and the thickness of the PFC

(L), namely:

$$T_s = \frac{Q_{ss}L}{\kappa} \tag{3.1}$$

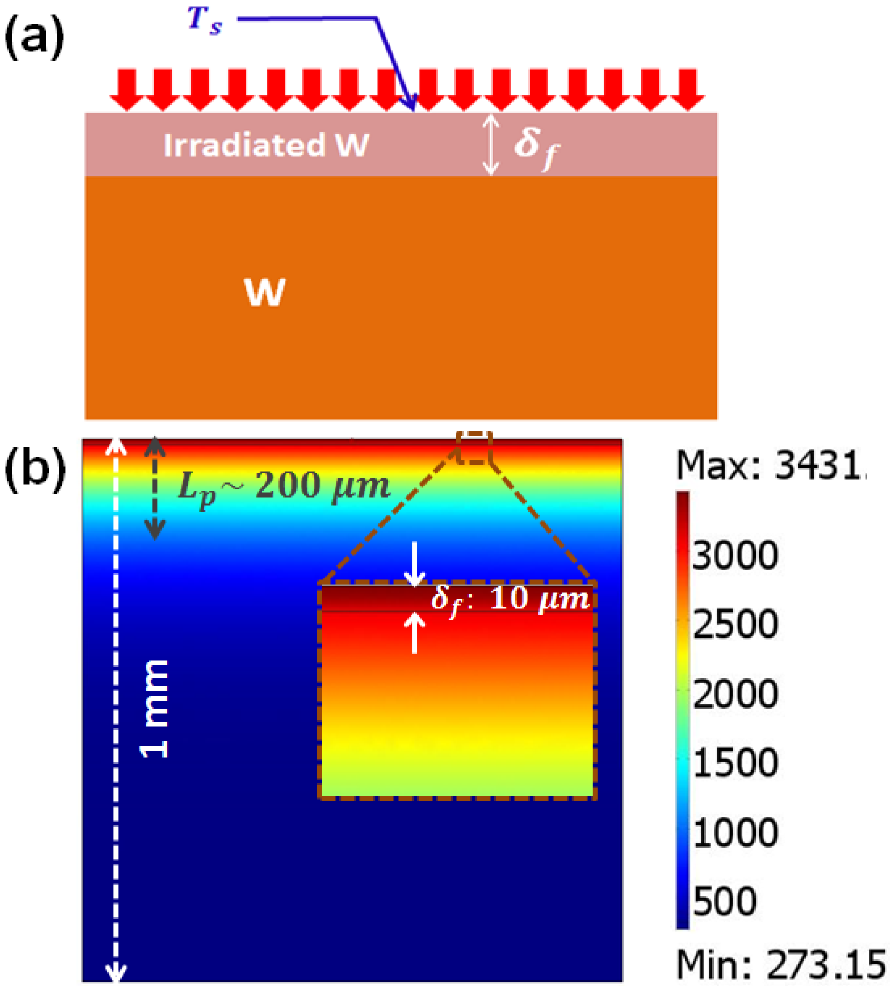

Figure 3.1: (a) A schematic of tungsten with irradiation thickness δ_f. T_s represents the surface temperature and the red arrow indicate the heat load. (b) Simulated cross-sectional temperature profile of W under transient thermal loading (Q_t = 2 GW m^{-2}) at the end of the heat load duration (t = 0.5 ms) when thermal conductivity of the top irradiated layer (δ_f = 10 μm) is half of the W substrate (κ_{film} : κ_{bulk} =1:2). The color represents the temperature in accordance to the color scale on the right. The majority of the temperature gradient occurs within the thermal penetration depth L_{pen} of about 200 μm. Inset: zoom-in temperature profile near the surface, which shows large temperature gradient across the film.

Eq.(3.1) shows that the entire thickness of the PFC contributes to the temperature rise for steady-state heat loads.

On the other hand, in the case of transient heat loads (Q_t) with a short duration of 0.5 to a few ms, the thermal penetration depth (L_{pen}) can be significantly shorter than the overall thickness of PFCs. According to one-dimensional heat diffusion equations [106], L_{pen} is defined as

$$L_p \approx \sqrt{2\alpha t} = \sqrt{\frac{2t\kappa}{\rho C}}, \tag{3.2}$$

where α is the thermal diffusivity, ρ is the density, C is the specific heat of the PFC, and t is the duration of the transient heat load. Based on the thermophysical properties of W, for $t = 0.5$–2 ms, L_{pen} ranges from 200 to 400 μm. As a result, the near-surface regime of PFCs, despite its small thickness, would play an important role in dictating T_S and consequently the thermo-mechanical behaviors.

When subjected to the very high particle fluxes in fusion reactors, the surface of PFCs is well known to experience damages [103–105, 107] . On one hand, plasma bombardment can alter the surface material properties such as morphology and could lead to reduced thermal conductivity, which may also consequently cause a higher surface temperature, inducing larger thermal stresses in the near-surface regime of PFCs, especially in the case of large transient heat loads. On the other hand, high energy particles such as 14 MeV neutrons displace W atoms from their original lattice sites and produce radiation damage in the W. The defects associated with the damage sites (interstitials, vacancies or extended clusters etc.) can act as electron and phonon scattering centers to reduce thermal conductivity of the material.

To illustrate the important effect of near-surface thermal conductivity on the temperature distribution in PFCs when subjected to transient heat loads, we modeled the surface temperature evolution of a hypothetical PFC made of W with a thin near-surface regime 10 μm thick, as shown in Fig.(3.1a). The transient heat load Q_t is 2 GW m^{-2} with a duration of 0.5 ms, which is typical for localized edge modes [100,101]. In this model, the substrate of the PFC has the thermophysical properties of bulk W (including temperature dependent thermal conductivity κ_{bulk} and specific heat C_{bulk}, while thermal conductivity of the near-surface regime (κ_{film}) is varied from 10% to 100% of κ_{bulk}. A time-dependent finite-element code was used to compute the evolution of the temperature for different cases. Fig.(3.1b) plots the cross-sectional temperature distribution in the PFC at the end of the transient heat flux (t = 0.5 ms), for the case with κ_{film}:κ_{bulk} = 1:2. This figure clearly shows that the majority of the temperature gradient occurs within the top 200-μm regime in the PFC, meaning that the transient heat load only penetrates into the PFC by about 200 μm, which is consistent with the result obtained from Eq.(3.2). The inset in Fig.(3.1b) also shows that there is a significant temperature gradient within the 10-μm-thick near-surface regime because of its lower κ.

Fig. 2 shows the time evolution of the surface temperature for various values of κ_{film}. The figure shows that T_S is getting higher as κ_{film} is reduced, as expected. Also, the maximum T_S occurs at t = 0.5 ms for all the cases. The inset in Fig. 2 plots the maximum T_S vs. κ_{film}, further demonstrating increased T_S as a result of lower κ_{film}. For instance, if κ_{film} was somehow reduced to 10% of that of bulk W, T_S would be as high as ∼4000 K, which would exceed the melting point of W (the model did not take phase change phenomenon into account).

The modeling result shown above highlights the importance of the near-surface

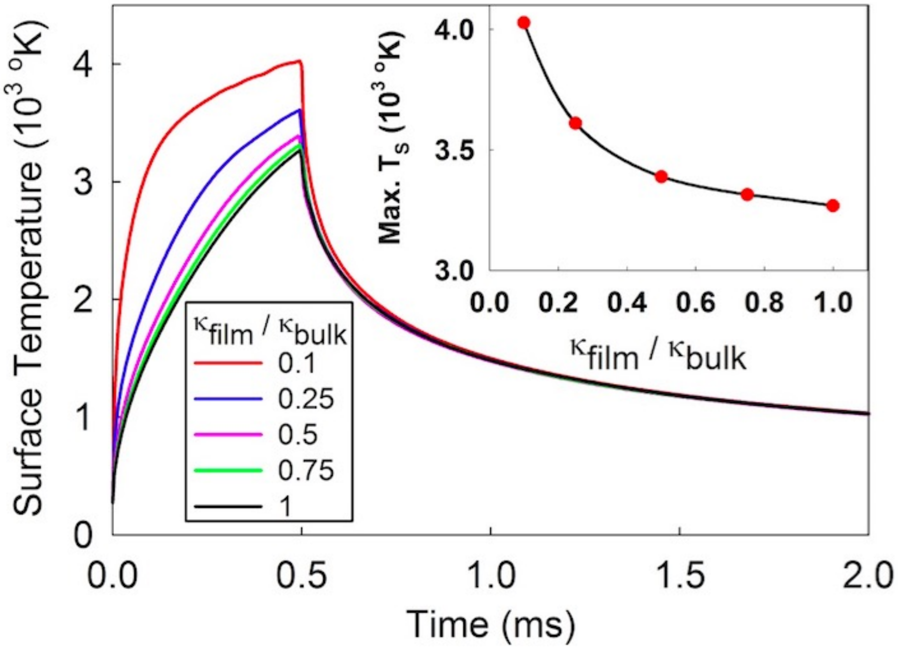

Figure 3.2: Time evolution of surface temperature T_s under an applied transient heat flux (Q_t = 2 GW m^{-2} and t = 0.5 ms) for samples with various $\kappa_{\rm film}$ values. Inset: Maximum T_s vs.$\kappa_{\rm film}$ values, showing increasing T_s with lower $\kappa_{\rm film}$.

thermophysical properties of PFCs on the surface temperature, especially in the case with large transient heat loads. The higher surface temperature may pose severe challenges for the operation of fusion reactors. It may exceed the melting point of W and directly cause the failure of the material. It could also lead to very large thermal stress in the near-surface regime and consequently lead to failure via delamination or cracking. Therefore, understanding the thermal properties of the thin damaged regime is vital in assessing the thermomechanical behaviors of PFCs.

As the damaged regime is only nanometers (implantation depth) to microns (diffusion distance) thick, conventional steady state thermal conductivity measurement techniques are not applicable. In this work, we describe the application of an advanced thermal characterization technique referred to as the ‘3ω method’ to measure the thermal conductivity of the micro-sized near-surface damaged regime of PFCs. Using W as a model PFC material, we measured the thermal conductivity of the thin (~1 μm thick) ion beam displacement-damaged regime on W samples. Our measurements demonstrated more than a 50% reduction in thermal conductivity of the damaged near-surface regime compared to pristine W (from ~179 W $m^{-1}K^{-1}$ to 73.5 ± 23.2 W $m^{-1}K^{-1}$. Therefore, our measurement provides not only a quantitative thermal conductivity value for future PFC designs, but also offers insights into thermo-mechanical properties of such materials.

3.2 Experimental

In this work, we use W as the model material for PFCs. The materials used in these experiments were polycrystalline Plansee ITER Grade W disks of 6 mm in diameter and 2 mm thick. The surfaces were mechanically polished to a mirror finish, and then the samples were cleaned in an acetone ultrasonic bath and annealed at 1273 K for 1 hr to decrease the amount of intrinsic defects and remove impurities. Damage production in W through Cu ion irradiation was performed at room temperature on the tandem ion accelerator at Ion Beam Materials Laboratory (IBML) in Los Alamos National Laboratory (LANL). To produce a uniform damage profile in W, three energies of Cu ions (500 keV Cu^+, 2 MeV Cu^+, and 5 MeV Cu^+) were used sequentially in the experiment with different fluences. The power density of Cu ion irradiation is ~0.01 MW m^{-2}, much smaller compared to the plasma disruptions, which is on the order of 100 MW m^{-2} to 1 GW m^{-2} for power flux during transient in confinement devices. Here in this work, we employed the ion irradiation with low power density in order to mimic neutron displacement damage rather than any plasma heating effects. Fig.(3.3) shows the predicted damage profile based on Monte Carlo simulations by SRIM simulation codes [108], where the threshold displacement energy of 90 eV (as recommended in Ref. [109]) was used for W atoms. Fig.(3.3) shows that the uniform damage thickness is approximately 1 μm beyond which the damage level drops off gradually. For the simplicity of the data analysis, we approximate the damaged region as a single uniform layer in this work.

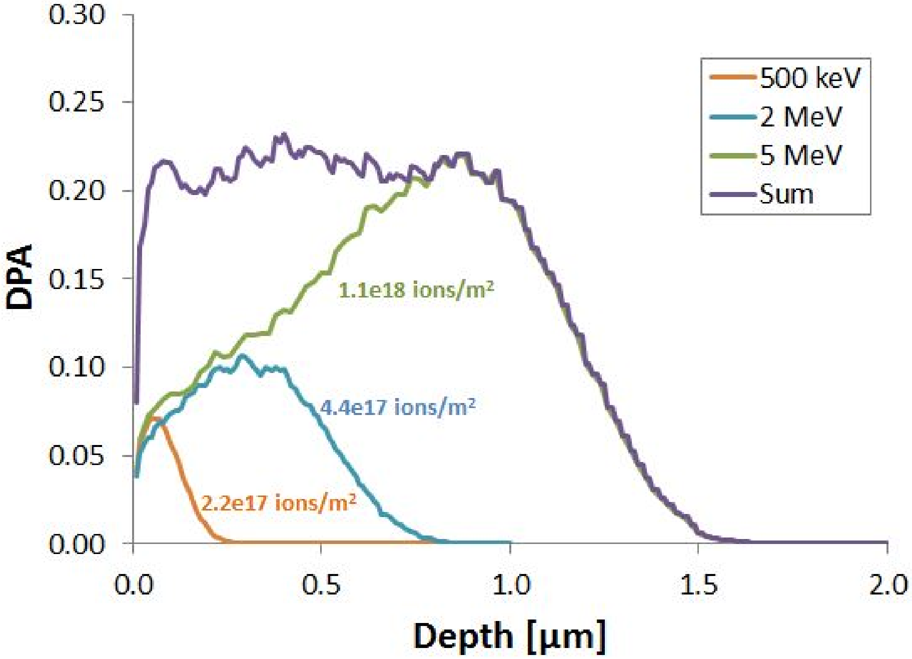

Figure 3.3: The DPA depth profile of the W sample irradiated by Cu ions. Multiple irradiations with different energy and fluence levels were used to produce a nearly flat DPA profile within the top 1 μm layer.

For 3ω measurements, the sample preparation involved fabricating a thin metallic heater strip on top of the W samples (Fig.(3.4a)). In this experiment, heaters on both pristine and ion irradiated W samples were processed at the same time with the same recipe to minimize error in the differential method described below. For electrically conductive samples, such as W, a thin insulation layer must be deposited on top of the sample to avoid electrical leakage from the heaters to the sample (Fig.(3.4a)). This was achieved by depositing a ∼60-nm thick Al_2O_3 insulation layer using the atomic deposition layer (ALD) technique at 250°C. The micron-sized heaters were then fabricated using e-beam lithography and lift-off processes. Briefly, the Al_2O_3 coated samples were first spin-coated with photoresist (PMMA A9) and subsequently patterned using e-beam lithography. Ti (25 nm) and Au (∼200 nm) were deposited by sputtering, which, followed by a liftoff process, yields the 3ω heater, as shown in Fig.(3.4b).

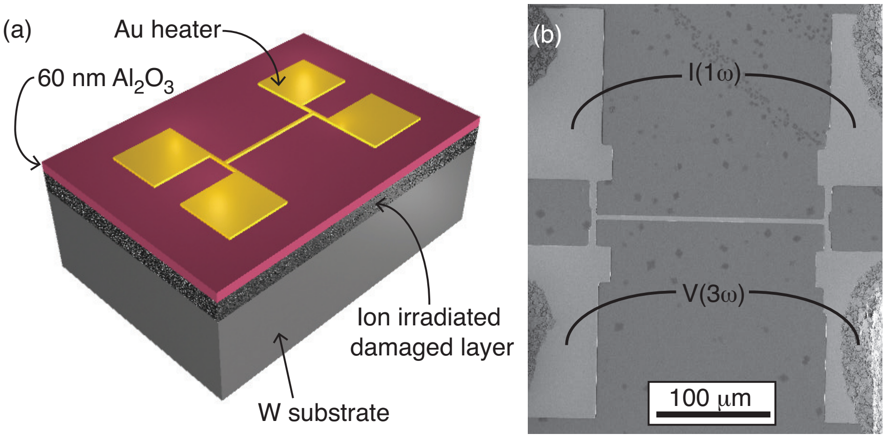

Figure 3.4: (a) Schematic diagram of a device for 3ω measurement for the ion damaged layer (∼1 μm thick) in W. An insulation layer of Al_2O_3 is deposited using ALD to prevent electrical leakage between the Au heater and the W sample. (b) A top view scanning electron microscopy (SEM) image of the device. During the 3ω measurements, a current ($I(\omega)$) is applied across two of the electrodes connected to the narrow metal strip while the 3rd harmonic voltage ($V(3\omega)$) is measured between the other two electrodes.

The 3ω measurements, as described in Chapter 1, were performed in a vacuum chamber to minimize heat loss due to convection. By using a lock-in amplifier (Stanford Research SR 830), $V_{3\omega}$ can be measured and distinguished from other voltage signals. Since the $V_{1\omega}$ is typically much larger than $V_{3\omega}$, the $V_{1\omega}$ signal must be eliminated to accurately detect 3ω voltage. This can be achieved by connecting a matching resistor with identical resistance in series with the 3ω metal strip and using a differential amplifier to subtract the common-mode 1ω and other parasitic signals [30].

In this experiment, a small heater width of $\sim$4 μm was employed for the following reasons: (1) a narrower heater results in a higher heat flux (per unit area), thereby leading to a higher T_{rise} that is measurable by the lock-in amplifier; and (2) a narrower heater also allows the use of AC current with a higher frequency, which leads to a shorter thermal penetration depth and consequently a relatively larger contribution to T_{rise} from the thin damaged regime. In this particular case, the heater width ($\sim$4 μm) is comparable to the thickness of the damaged layer ($\sim$1 μm). Therefore, the generalized 2D analysis, as described above in Chapter 1, is needed to accurately model the heat transfer process and extract the thermal conductivity values from the measurement data [31,32].

To apply the 3ω method to measure the thermal conductivity of the near-surface regime, we employ a differential method [32,39,56], in which two samples, one without and the other with the ion-displacement damage, were measured. The first measurement on the pristine W sample, called the 'reference' sample, was performed to obtain the thermal conductivity values of the W substrate and the insulating layer (Al_2O_3) by fitting the measured T_{rise} to the 2D heat conduction model. Fig.(3.5) shows an example of the measured T_{rise} data (symbols) as a function of modulation frequency on a reference W sample, along with the fitting result (dash line) using the generalized 2D heat conduction. The best fit yields the κ values of the W substrate and the Al_2O_3 insulation layer to be 179 ± 4 and 1.2 W $m^{-1}K^{-1}$ respectively at room temperature. With the measured κ values of the W substrate and the Al_2O_3 layer, the second measurement on the irradiated W sample was then used to determine the only remaining unknown parameter, the thermal conductivity value of the damaged thin film. Fig.(3.5) also shows the measured and fitted T_{rise} data on the irradiated sample at 300 K, with the κ value of 73.5 W m^{-1}K^{-1} yielding the best fitting result.

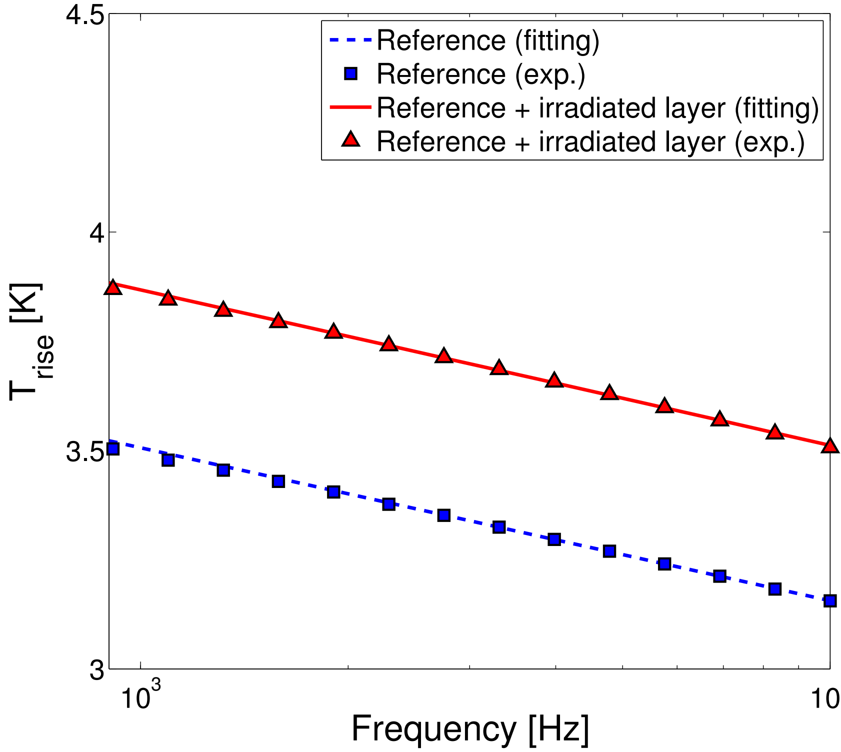

Figure 3.5: Experimental temperature rise with fitting results of the reference (pristine) W sample and the irradiated W sample. The range of the modulation frequency was chosen to be from 900 Hz to 10 kHz based on the associated thermal penetration depth. The blue squares represent the experimental T_{rise} and the blue dash line is the fitting using a 2D heat conduction model for the reference sample. The fitting yields thermal conductivity values of the W substrate and the insulation layer, which was then used to model T_{rise} of the irradiated sample (red solid line) to fit the measured data (red triangles) and yield the thermal conductivity of the irradiated layer.

The uncertainty mainly originates from a fairly small uncertainty (about 1.8%) in the measurements of the temperature rise due to the periodic heating. Because the temperature drop across the irradiated layer (∼0.36 K) is only about 10% of the total temperature rise of the irradiated sample (~3.6 K) due to its thin structure and relatively high thermal conductivity, modest uncertainties in the temperature rises of the reference sample (~ ±1.8% or ±0.065 K at 300 K) and irradiated sample (~ ±1.8% or ±0.058 K at 300 K) can cause a relatively large uncertainty in the calculated difference between these two, which ultimately leads to a relatively large uncertainty in the final thermal conductivity value determined by the 3ω method. This is an inherent challenge for the 3ω method related to the particular sample geometry and thermal conductivity values.

3.3 Results and Discussing on Thermal Conductivity of A Ion-Damaged W Layer

The measured κ of the ion irradiated W layer at different temperatures are plotted in Fig.(3.6), along with κ of the pristine W sample. The ion irradiation dosage for the measured damaged sample was 0.2 displacement per atom (dpa). The measured κ values of the pristine W sample agree very well with published data from NIST [110] within the measured temperature range, thereby validating the measurement technique. For the irradiated W, the room temperature thermal conductivity (73.5 ± 23.2 W $\mathrm{m^{-1}K^{-1}}$) is reduced from that of pristine W (179 ± 4 W $\mathrm{m^{-1}K^{-1}}$) by nearly 60%. The reduction in thermal conductivity is likely caused by the defects formed during ion beam irradiation. For W exposed to similar levels of Cu ion irradiation, formation of voids and nanometer size defects has been observed [107]. These defects can serve as scattering centers for the transport of heat carriers (primarily electrons in W), thereby reducing the thermal conductivity. The reduction in

κ in the near-surface regime can present challenges for thermal management of PFCs during transient thermal loading, as discussed earlier.

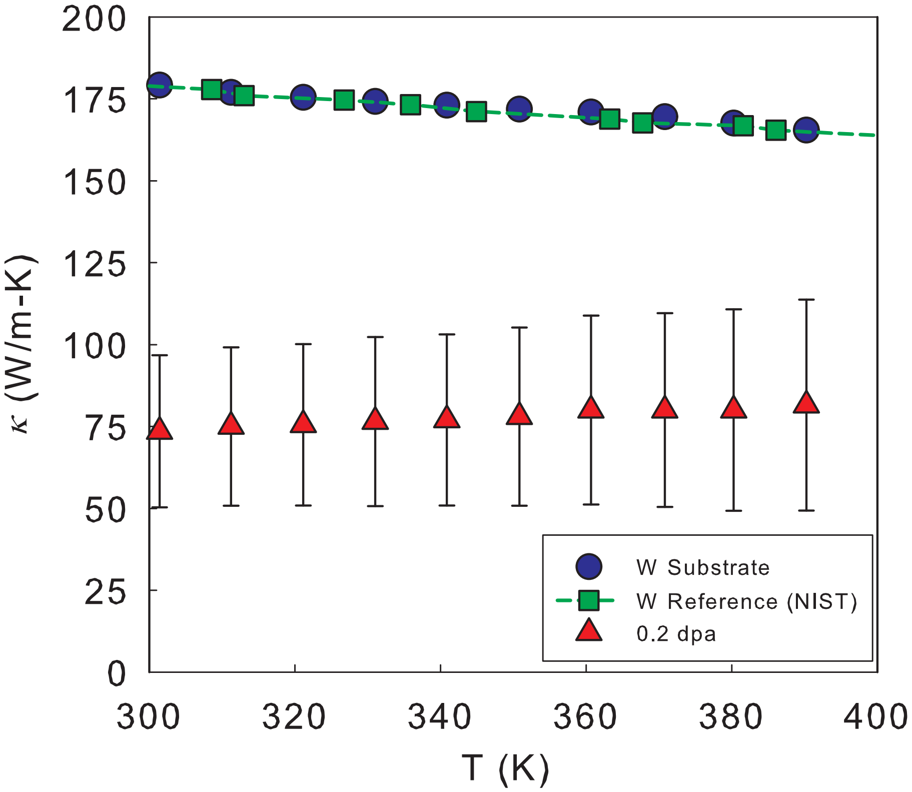

Figure 3.6: Thermal conductivity of pristine W and an ion damaged W layer (with 0.2 dpa dosage) from 300 to 400 K, along with the standard value of W published by NIST. The error bar represents uncertainties in the measurements, primarily due to temperature measurement and the determination of the temperature coefficient of resistance (TCR) of the heaters. The error due to the uncertainty from the damaged layer thickness is not included. The thermal conductivity of the ion irradiated film is about 60% lower than that of pristine bulk W, and is nearly temperature independent, suggesting the effect of defects introduced during ion irradiation.

Defects introduced during the ion irradiation process also alter the temperature dependence of thermal conductivity. In bulk pristine W, as electrons are the main heat carriers, the thermal conductivity can be approximated from the Wiedemann-Franz law, $\kappa_e = \mathrm{L}\sigma T$, where L is the Lorentz number and σ is electrical conductivity [54].

Therefore, as temperature rises, increased electron-phonon scattering rate in W leads to a decreasing κ with temperature, as evident in our measurements (Fig.(3.6)). On the other hand, for the ion irradiated W samples, κ of the damaged layer is relatively constant from 300 to 400 K (Fig.(3.6)), which is indicative of impurity scattering that is absent in the pristine bulk structure, because defect scattering is mainly influenced by the size, mass, and density of defects/impurities, but not temperature. Assuming impurities and electron-phonon scatterings are uncorrelated, Matthiessen's rule [54] ($\tau^{-1}_{\text{total}} = \tau^{-1}_{\text{impurity}} + \tau^{-1}_{\text{electron-phonon}}$, where τ^{-1} is the scattering rate) suggests that the impurity scattering in the damaged W also plays an important, if not the dominant, role in carrier and thermal transport in W.

It is also worth comparing our result to that in the literature. Previously, Peacock and co-workers [111, 112] used the laser flash method to measure thermal conductivity of neutron-irradiated W samples, and reported a κ value of ~152 and W $m^{-1}K^{-1}$ for samples with 0.2 and 0.6 dpa irradiation dosages, respectively. Compared to their results, the values obtained from the present 3ω measurement are considerably lower. The origin of this discrepancy could be due to possible different irradiation conditions, where their samples were irradiated at 200 C with neutrons instead of ions [111,112], and possibly the different measurement techniques involved. Therefore, a systematic study, such as the one involving various ion irradiation conditions, is needed in order to understand the effect of ion irradiation on thermal transport properties in the near-surface regime.

Chapter 3, in part, is a reprint of the material in Journal of Nuclear Material, 2014, Edward Dechaumphai, Joseph L. Barton, Joseph R. Tesmer, Jaeyoon Moon, Yongqiang Wang, George R. Tynan, Russ P. Doerner, and Renkun Chen. The dissertation author was the primary investigator and the first author of this paper.

Chapter 4

Achieving Sub-Picowatt Resolution Calorimetry

4.1 Introduction

Calorimetry plays an important role in a multitude of applications, such as probing fundamental thermodynamics of materials [113–115] and biochemical reactions [116], studying thermal transport phenomena especially at microscopic level [2, 3, 18, 19, 44, 117–119], high-throughput drug screening in pharmaceutical industries [95,120], infrared thermal imaging [21], and so on. While commercially available calorimeters have been improved significantly and now possess a resolution as good as ∼10 nW [116], there is a continued interest to further improve the resolution to meet a myriad of scientific and technical needs, such as measuring heat conduction through single-chain DNA [121] and single molecular wires [122], and studying single cell metabolic rate [123] (typical single cell metabolic rate is of the order of picowatts [124]). Recently, Narayanaswamy and coworkers demonstrated the highest calorimetric resolution at room temperature using a bi-material cantilever (0.9 ± 0.3 pW) [125]. On another front, Reddy and coworkers have shown that ∼4–5 pW resolution can be achieved in both platforms based on bi-material cantilevers [126] and resistive thermometry [27]. The resistive thermometry-based approach may be advantageous in some applications because it is easier to integrate into devices and can operate within a wide temperature range. The pending question, therefore, is whether one can achieve sub-pW resolution using the resistive thermometry platform.

4.2 Theoretical Analysis of Power Resolution for Resistive Thermometry-based Calorimeter

To identify important parameters in the design of high-resolution calorimeter using resistive thermometry, we first examine the power resolution of a calorimeter, Q_{res}, which can be defined as

$$Q_{res} = G \cdot NET, \tag{4.1}$$

where NET is the noise equivalent temperature and G is the total thermal conductance between the calorimeter and the ambient. Therefore, two key factors leading to high-resolution calorimetry are low G and low NET. In the case of calorimetry platforms based on resistive thermometers, these two factors hinge on two intrinsic properties of the thermometry material, namely, the thermal conductivity (κ) and temperature coefficient of resistance (TCR). To illustrate this point, we consider a calorimeter using a uniform suspended beam as the thermometer, as shown in Figure 4.1(a). Assuming the entire sensing beam has a resistance of R_s, TCR of α_s (defined as $\frac{dR}{R_s dT}$, and has a current of I_s applied on it, then the NET (at the center of the beam) is related to the noise-equivalent voltage (NEV) by

$$NET = \frac{2\sqrt{2}NEV}{I_s R_s \alpha_s} \tag{4.2}$$

where NEV is the noise-equivalent voltage of the sensing beam, the factor of $\sqrt{2}$ accounts for the conversion from root-mean-square values of the voltage to amplitude values of the temperature (assuming modulated heating current [28]) and the factor of 2 accounts for the fact that the temperature of the middle pad of the beam is twice the average temperature across the entire suspended sensing beam (R_s).

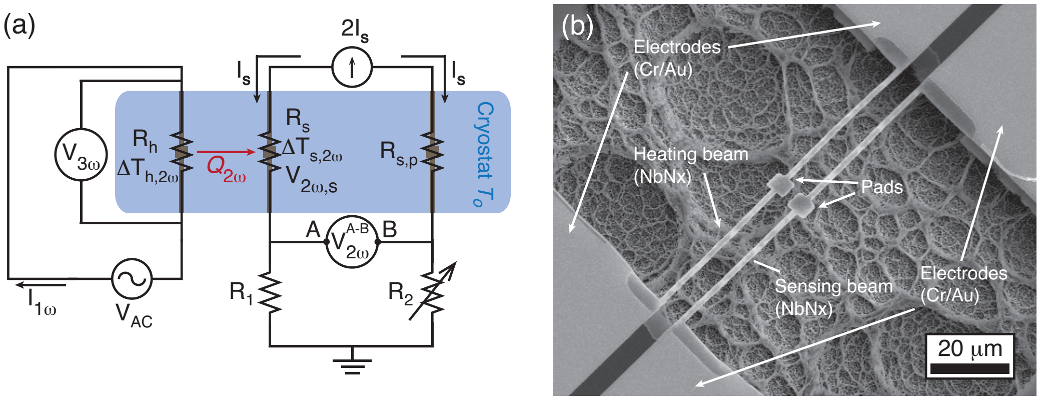

Figure 4.1: (a) Schematic of the measurement setup with modulated heating scheme on the (left) heating side and the Wheatstone bridge circuit to measure the temperature on the sensing side. (b) SEM image of the device with two suspended NbNx beams for heating and sensing, respectively.

The NEV in Eq.(4.2) is constrained by both intrinsic and extrinsic noises of the thermometer. However, in the case when modulated heating is employed, the noise will be primarily limited by the Johnson noise because the modulated heating significantly reduces $1/f$ noise caused by thermal drift [27, 127] and the bridge-based differential scheme effectively cancels the correlated temperature fluctuation [128]. By implementing these two schemes, one can construct a resistive thermometer with NEV close to the Johnson noise level (namely, $\sqrt{4k_B T R_s \Delta f}$), as demonstrated previously by Sadat et al. [27, 127] and us [28].

Here, we consider the Wheatstone bridge shown in Fig. 4.1(a) to measure the temperature change of the sensing side (R_s) by measuring its resistance change (δR_s). Assuming the bridge is initially balanced and all the four resistors have the same resistance of R_s. When there is a heat flux modulated at 2ω transferred to the sensing side, the corresponding change in the resistance is δR_s, as shown in Fig. 4.2.

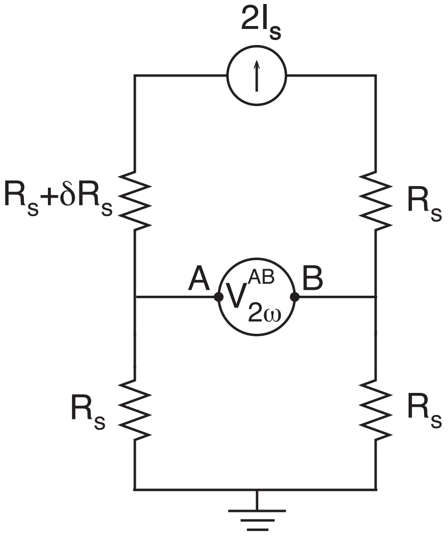

Figure 4.2: A Wheatstone bridge with four identical resistors to measure a small change in the resistance of the sensing beam (δR_s)

The 2nd harmonic voltage across the nodes A and B resulted from heating modulated at 2ω is:

$$V_{AB} = V_A - V_B = \left(\frac{R_s}{2R_s + \delta R_s} - \frac{1}{2}\right) 2I_s \left(\frac{(2R_s + \delta R_s)\, 2R_s}{4R_s + \delta R_s}.\right) \tag{4.3}$$

Because $\delta R_s \leqslant R_s$, Eq.(4.3) can be simplified to:

$$V_{AB} = -\frac{1}{2} I_s \delta R_s \tag{4.4}$$

The factor of 1/2 on the right hand side of Eq.(4.4) is a result of this particular bridge configuration. Based on Eq.(4.4), we can then relate the NEV (measured from A to B) to the noise equivalent resistance (NER) of the sensing beam via:

$$NER = 2\frac{NEV}{I_s}, \tag{4.5}$$

which is corresponding to a NET on the middle pad of the beam via:

$$NET = 2\sqrt{2}\frac{NER}{R_s \alpha_s}, \tag{4.6}$$

where the factor of $\sqrt{2}$ accounts for the conversion from rms values of the voltage to amplitude values of the temperature and the factor of 2 accounts for the fact that the temperature of the middle pad of the beam is twice of the average temperature across the entire suspended sensing beam (R_s).

Substituting Eq.(4.5) into Eq.(4.6), one yields:

$$NET = 4\sqrt{2}\frac{NEV}{I_s R_s \alpha_s}. \tag{4.7}$$

Note that the extra factor of 2 in Eq.(4.7) compared to Eq.(4.2) is due to the particular bridge configuration and different definitions of NEV. In Eq.(4.7), NEV is defined as the voltage noise across the nodes A and B in the bridge, whereas in Eq.(4.2), NEV is defined as the voltage noise across R_s.

Now consider the same bridge shown in Fig. 4.2, and assume the noise on each resistor is Johnson noise, it can be shown that the overall noise measured between the nodes A and B is the same as the noise of a single resistor, namely,

$$NEV_{AB} = NEV_{R_s} = \sqrt{4k_{\mathrm{B}}TR_s\Delta f}, \tag{4.8}$$

where Δf is the bandwidth of the measurement.

By substituting Eq.(4.8) into Eq.(4.7), it can be shown that the NET is related to the Johnson noise measured between nodes A and B via

$$NET = \frac{8\sqrt{2k_BTR_s\Delta f}}{I_sR_s\alpha_s}. \tag{4.9}$$

Equation (4.9) shows that NET can be improved when the sensing current I_s is higher. However, there is a limit on the applied sensing current, because a high I_s would lead to an undesirably large temperature rise on the thermometer. The maximum allowed temperature rise of the calorimeter due to the sensing current is written as

$$\Delta T_{\max} = \frac{I_s^2R_s}{2G}. \tag{4.10}$$

Substituting Eq. (4.10) into Eq. (4.9), one yields

$$NET = \frac{8}{\alpha_s}\sqrt{\frac{k_BT\Delta f}{G\Delta T_{\max}}}. \tag{4.11}$$

Therefore, according to Eq. (4.1), the Q_{res} limited by the Johnson noise is

$$NET = \frac{8\sqrt{G}}{\alpha_s}\sqrt{\frac{k_B T \Delta f}{\Delta T_{\max}}}. \tag{4.12}$$

Equation (4.12) clearly shows that the heat current resolution critically depends on G and TCR of the thermometry materials, when other conditions being the same. Therefore, it is desirable to make calorimeters based on a thermometry material with a high TCR and a low κ.

Among many thermometry materials, metals, such as Pt, have been widely employed, for instance, in earlier calorimeters used for nanoscale thermal measurements [26,27,129], due to the ease of fabrication and integration into instrumentations (e.g., with low resistivity). Its main drawback, however, is its high κ and a relatively modest TCR (~0.15%/K for Pt). Therefore, Pt and other metals are not necessarily the best thermometry material of choice for high-resolution calorimetry.

In my thesis work, we developed a calorimeter with an unprecedentedly high resolution using a high-performance thermometry material based on niobium nitride (NbNx), which exhibits both a high TCR and a low κ. NbNx has previously been used as the resistive thermometer for sensitive calorimetry by Bourgeois and coworkers [113, 130–132], and has shown a high TCR value up to 0.9%/K with a resistivity of ~10–20 mΩ·cm at room temperature [133–135]. At cryogenic temperature, NbNx has an even higher TCR (~5.3%/K at 77 K) [133–135]. Even though NbNx has a higher resistivity than Pt, the resistivity is not factored into the Q_{res} of a calorimeter (Eq.(4.12)). Unlike metals, NbNx also has a low κ (as determined to be ~1.1 W m^{-1}K^{-1} from our study, which will be later described in this chapter). We demonstrated that the resistive thermometry-based calorimetry can be improved substantially by using the novel devices derived from NbNx films.

4.3 Fabrication of the NbNx-based Resistive Calorimeter

To demonstrate the sensitivity of the NbNx based calorimeter, we fabricated two suspended parallel beams made of NbNx, one for heating and the other for sensing, as shown in Fig. 4.1(b). Each NbNx beam is 80 ± 20 nm thick, 1.54 ± 0.03 μm wide, and 105.2 ± 0.1 μm in total length. NbNx electrodes on the unsuspended region are insulated from the substrate with a 100-nm-thick silicon nitride layer, and are covered with a Cr/Au film for metallization.

NbNx was deposited via reactive sputtering using a Nb target in a gas mixture of nitrogen and argon. The stoichiometry of the film is dictated by the partial pressure of N_2 and Ar gases. For our devices, the partial pressure ratio was 8:1 (N_2:Ar) and the total sputtering pressure was 10 mTorr. A more detailed discussion of reactive sputtering of NbNx is described in Ref. [133].

Summary of fabrication steps:

1. Deposit parylene or SiNx on a Si wafer.
2. Deposit NbNx by reactive sputtering. Annealed NbNx in an N_2 environment.
3. Perform photolithography process #1: for electrode and beam patterning.
4. Deposit Cr and Au by sputtering. Then lift off in acetone.
5. RIE etch NbNx (and parylene) having Au as the etching mask on the beam.
6. Perform Photolithography #2: for opening window to etch Cr/Au on the beam.
7. Wet etch Cr and Au. Remove photoresist.

8. Deposit parylene (to protect NbNx when performing Si etching using XeF_2.

9. Perform Photolithography #3: for patterning of window and beam protection mask during Si etching.

10. Etching Si with XeF_2 . This process also etches SiNx and thin layer of parylene.

11. Remove photoresist with O_2 plasma etching. (parylene will also get etched).

4.4 Noise Equivalent Temperature of the NbNx-based Resistive Calorimeter

The temperature rise of the sensing NbNx beam is measured using a Wheatstone bridge circuit, where the sensing beam is paired in conjunction with another on-chip NbNx beam with almost identical resistance (Fig. 4.1(a)). The power spectral density of the noise across node A and B is measured to be near the Johnson noise at sufficiently high frequencies, in which the $1/f$ noise plays a minimal role, as shown in Fig. 4.3.

Because the $1/f$ noise becomes more pronounced when the frequency is below 2 Hz and the signal attenuates notably at higher frequencies (>4 Hz), we chose a frequency of 4 Hz in our measurement, in which both the $1/f$ noise and the signal attenuation are minimal.

Next, the resistance and TCR of the NbNx beams were determined from the four-point current-voltage measurements within the temperature range of 40–300 K, as shown in Fig. 4.5. The resistance increases at lower temperature, indicating a semiconducting behavior. In the sputtered NbNx film, which is of the amorphous phase,

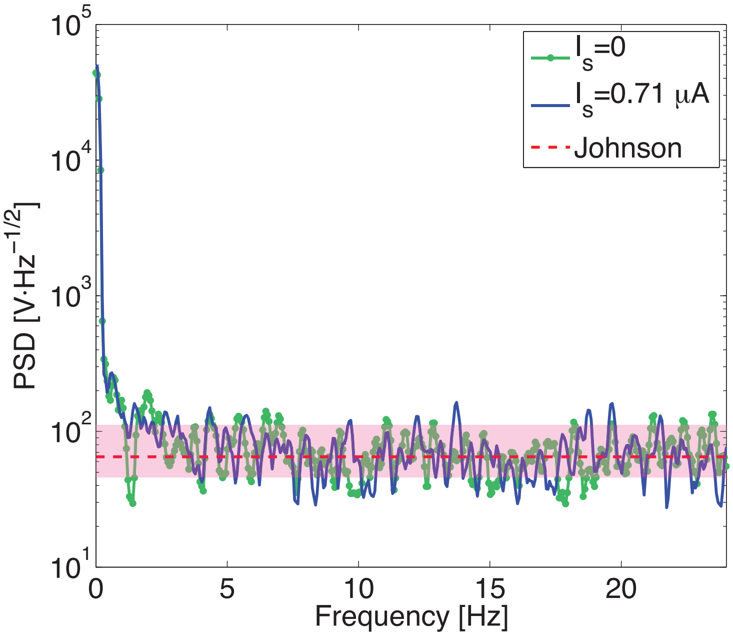

Figure 4.3: Power spectral density (PSD) of the noise measured across node A-B shown in Fig. 4.1(a). The green dotted line and the blue solid line represent the PSD when the applied current (I_s) is zero and 1.3 μA (typical sensing current applied in this study), respectively, showing no apparent difference in the noise spectrum when applying the sensing current due to the suppressed shot noise in the current source [28, 127]. At sufficiently high frequencies (above 3 Hz), the noise levels are close to the Johnson noise (horizontal dashed line).

the electron conduction can be described using the Mott's variable range hopping model, namely,

$$R = R_o \exp\left[\left(\frac{T}{T_o}\right)^{1/n}\right], \tag{4.13}$$

where R_o is a constant, T_o is the characteristic Mott's temperature, and n is 4 for a typical 3D bulk material [136]. As shown in Fig. 4.5, Eq. (4.13) fits our resistance data of the NbNx beam very well with fitting parameters determined to be $R_o = 81.35\ \Omega$, $T_o = 1.19 \times 10^6$ K, and $n = 4$.

By taking the derivative of R with respect to T according to Eq.(4.13), the

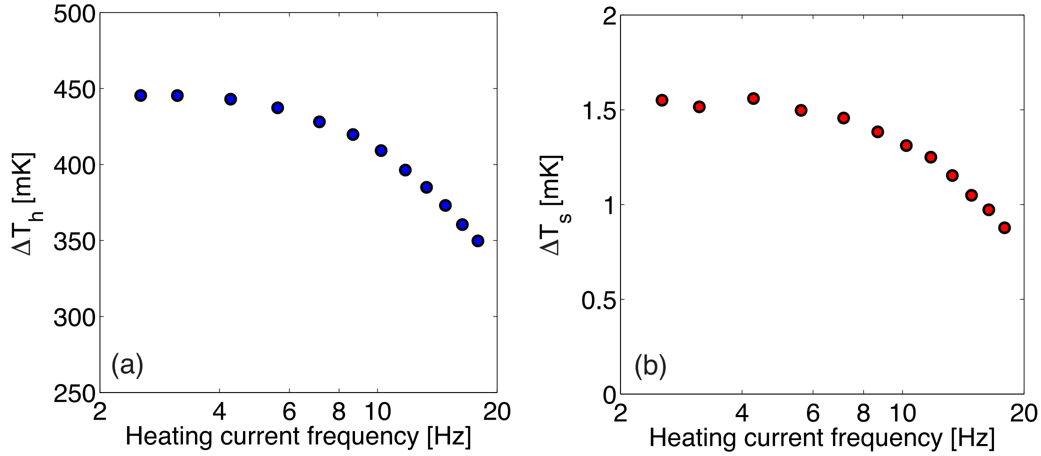

Figure 4.4: (a) Measured heating side temperature as a function of frequency (blue circles). (b) Measured sensing side temperature as a function of frequency (red circles). Signal attenuation depends on the thermal penetration depth, where $L_p\ 1/\sqrt{f}$. Hence, signals are attenuated at high frequency. For our device, at $f = 6$ Hz, the signal will attenuate roughly 10% and drop off quickly at higher frequencies. Therefore, we selected 4 Hz in our NET measurements to obtain the power resolution of the device with minimum signal attenuation.

TCR is determined from

$$TCR = \frac{1}{R}\left(\frac{R_o T^{\frac{1}{n}-1}}{nT^{1/n}}\exp\left[\left(\frac{T}{T_o}\right)^{1/n}\right]\right) \tag{4.14}$$

The temperature dependent TCR is plotted in Fig. 4.5 as well. The TCR of the NbNx beam is consistent with NbNx film prepared by reactive sputtering studied previously [133–135]. At room temperature, TCR of NbNx is 0.67%/K ($\mathrm{R}_{300\mathrm{K}}$ = 230 kΩ). At lower temperature, TCR (resistance) of niobium nitride beam increases dramatically to as high as 7.08%/K (28.1 MΩ) at ∼45 K.

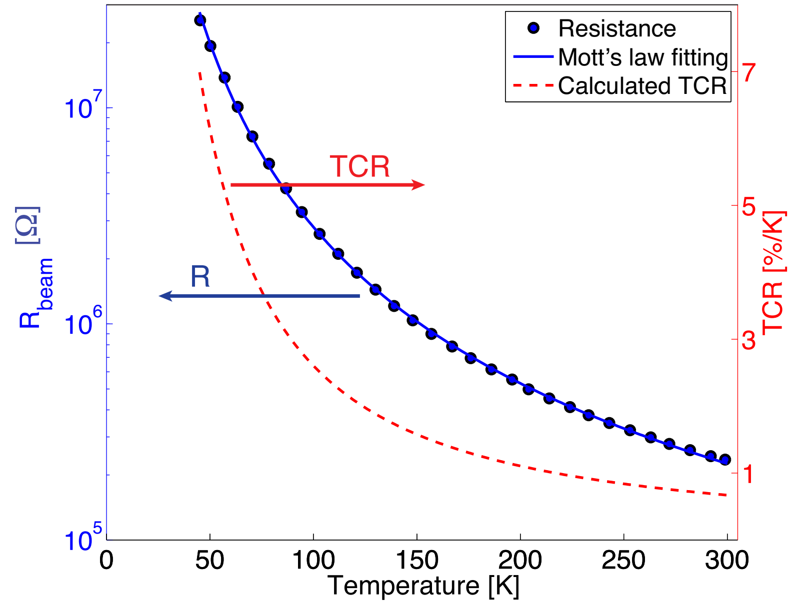

Figure 4.5: Resistance and TCR as a function of temperature. Blue circles are measured resistance of the heating beam. Blue line is the fitting using Mott's law. Red dashed line is the calculated TCR from the fitted $R(T)$. The TCR is 0.67%/K at room temperature and increases at lower temperatures.

4.5 Thermal Conductance Characterization of the NbNx-based Resistive Calorimeter

Consider the heat conduction model in the suspended heating beam and assuming negligible heat loss from the heating beam to the ambient (described in detail later), one could recognize the parabolic temperature distribution along the heating beam, namely,

$$\Delta T_h(x) = \frac{q''}{2\kappa_b A_b} x(2L_b - x), \tag{4.15}$$

where $q'' = \frac{I^2 R_h}{2L_b} = \frac{Q}{2L_b}$ is the heat flux per unit length of the beam in [W m^{-1}].

Therefore, the average temperature of the beam, which is also the effective temperature measured in our experiments for the AC schemes (in the low frequency limit), is,

$$\Delta\overline{T_h} = \frac{q'' L_b^2}{3\kappa_b A_b} = \frac{Q L_b}{6\kappa_b A_b} = \frac{Q}{3G_b}. \tag{4.16}$$

In other word,

$$G_b = \frac{Q}{3\overline{\Delta T_h}}, \tag{4.17}$$

where G_b is defined as $2\kappa_b A_b / L_b$, which is the effective conductance from the center of the beam to the substrate (note: it is not the conductance of the single beam). From measurements of $\overline{\Delta T_h}$ and at different known applied heating power, Q, to the beam, one can extracted G_b.

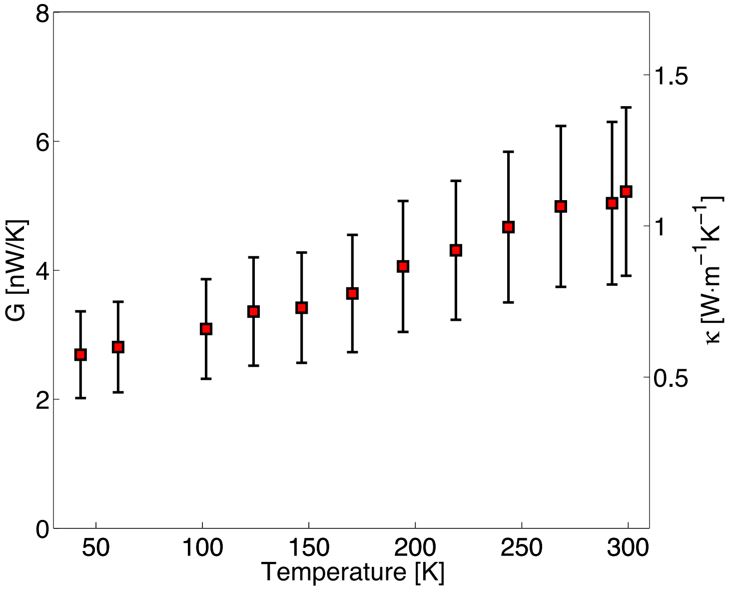

Figure 4.6: Thermal conductance (G) and conductivity (κ) of the beam as a function of temperature. At 300 K, G is 5.22 nW/K ($\kappa = 1.11 \pm 0.28$ W m^{-1}K^{-1}) and decreases with temperature. The shown error bars are only for the κ data and are primarily due to the uncertainty in the film thickness.

To determine the thermal conductance (G) and conductivity (κ) of the NbNx beam with the modulated heating scheme, we used the setup shown in Fig. 4.1(a). As shown in the figure, an alternating current modulated at 1ω is applied to the heating beam to generate joule heating ($P = I^2R$), which results in a 2nd harmonic heat flux, $Q(2\omega)$. Since the heat flux $Q_{2\omega}$ is directly proportional to temperature, the heating side temperature (ΔT_h) is also modulated at 2ω. Therefore, by measuring the 3rd harmonic voltage across the beam, ΔT_h can be extracted via temperature-resistance relation of the NbNx beam. The ΔT_h of the middle pad on the heating side can be determined from

$$\Delta T_h = \frac{3V_{3\omega}}{I_{1\omega}} \left(\frac{dR}{dT}\right)^{-1}, \tag{4.18}$$

which accounts for the fact that the average temperature of the beam is 2/3 of the temperature of the middle pad [28,137]. Then, G_{beam} can be calculated from $G_{beam} = Q/2\Delta T_h$. Again, note that $\Delta T_h \neq \overline{\Delta T_h}$. Figure 4.6 shows the measured temperature dependent thermal conductance of the NbNx beam from 40 to 300 K. At 300 K, the measured G is 5.22 nW/K, which corresponds to κ of the NbNx beam of 1.11 ± 0.28 W $\mathrm{m}^{-1}\mathrm{K}^{-1}$.

To substantiate our assumption on negligible heat loss from the heating beam to ambient, we measured the average temperature of self-heated microfabricated beams composes of suspended SiNx and Pt thermometer as shown in Fig. 4.7 and compared to results to a theoretical model that takes the heat loss into account. In this experiment, SiNx beams of varying lengths (100, 200, 400 μm) coated with Pt for self-heating and temperature sensing were utilized for the comparison

The heat loss along the beam is modeled by a constant heat transfer coefficient, h, from the beam to the ambient. The heat transfer equation along the beam thus follows the fin model (Fig. 4.7):

$$\kappa A \frac{d^2T}{dx^2} - hP\left(T - T_o\right) + \frac{Q}{L} = 0, \tag{4.19}$$

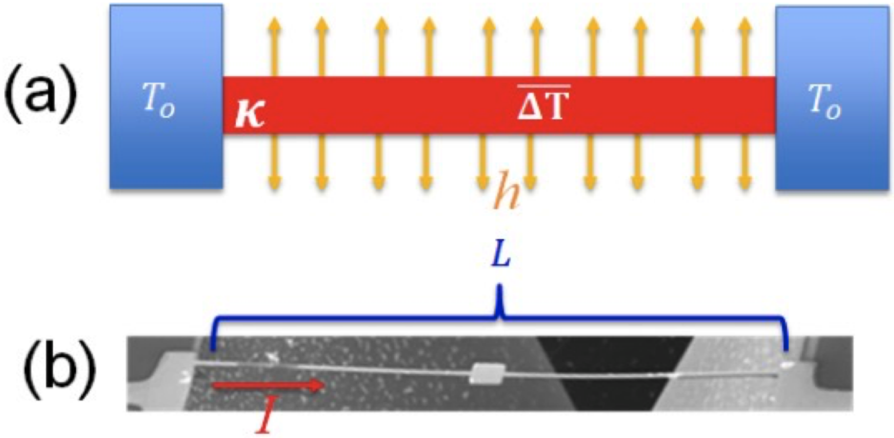

Figure 4.7: Thermal conductivity (κ) and heat transfer coefficient (h) determination of the SiNx beams. (a) Schematic of the thermal fin model. (b) A suspended beam of total length L self- heated by applying a current I.

where A is the cross sectional area, L is the length of the beam (note that $L = 2L_b$), T is the temperature along the beam, T_o is the ambient temperature, h is the heat transfer coefficient, P is the perimeter of the SiNx surfaces, and Q is the electrical power dissipated in the beam.

In the case when the heat loss in negligible ($h = 0$):

$$\begin{aligned} \Delta T = T - T_o &= \frac{Qx}{2\kappa A}\left(1 - \frac{x}{L}\right), && (4.20) \\ \overline{\Delta T} &= (QL) \,/\, (12\kappa A), && (4.21) \\ \frac{Q}{\overline{\Delta T}} &= \frac{12\kappa A}{L}. && (4.22) \end{aligned}$$

Whereas assuming heat loss in not negligible ($h \neq 0$) [106]:

$$\Delta T = \frac{Q}{hPL}\left[1 - \frac{\sinh(mx) + \sinh(m(L-x))}{\sinh(mL)}\right], \tag{4.23}$$

where

$$m = \sqrt{\frac{hP}{\kappa A}} \tag{4.24}$$

and subsequently,

$$\overline{\Delta T} = \frac{Q}{hPL}\left[1 - \frac{2(\cosh(mL)-1)}{mL\sinh(mL)}\right], \tag{4.25}$$

$$\frac{Q}{\overline{\Delta T}} = \frac{hPL}{\left[1 - \frac{2(cosh(mL)-1)}{mL\sinh(mL)}\right]} \tag{4.26}$$

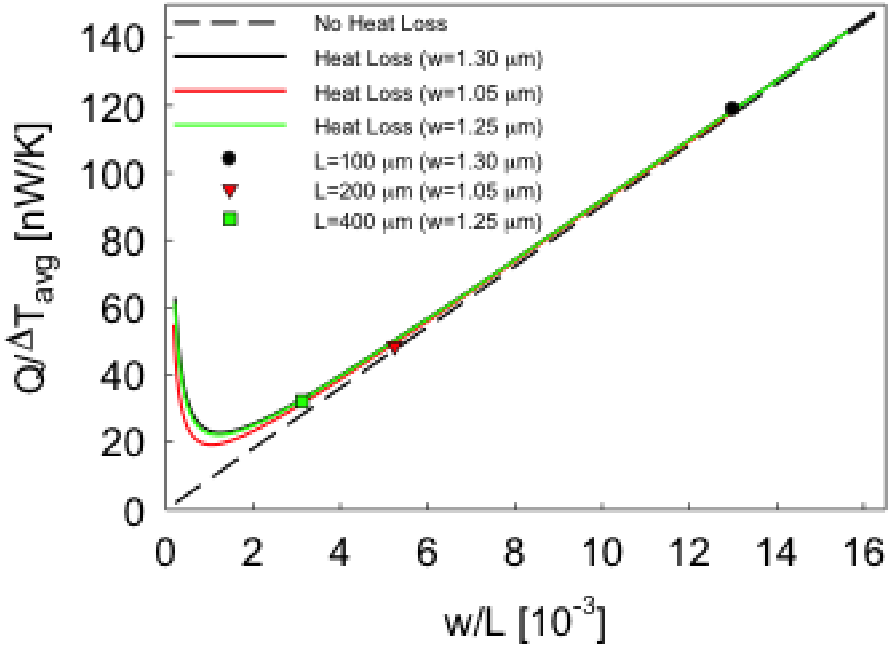

Figure 4.8: Heating power over average temperature rise vs. width over length for suspended beams with and without heat loss, solid and dashed lines, respectively. Three microfabricated beams of different lengths (100, 200, 400 μm) were measured (solid dots) and compared to theoretical curves with fitted thermal conductivity and heat transfer coefficient.

Figure 4.8 shows heating power over average beam temperature vs. beam width divided by length. These beams are the suspended SiNx beam with Pt thermometer [28]. For short beam lengths (<200 μm), the negligible and non-negligible heat loss models converge, validating the simplified thermal analysis. For longer beams, however, heat loss becomes increasingly significant, such that neglecting heat loss can lead to an overestimated temperature rise.

From the analysis (Fig. 4.8), it was shown that the heat loss is negligible in devices with $L = 100\ \mu m$ (or $L_b = 50\ \mu m$). Therefore, these short-beam suspended devices were chosen in this study for thermal measurements in order to ensure accurate thermal analysis (in addition to the fact that the short-beam devices have smaller thermal time constant and higher roll-off frequency). To directly verify negligible heat loss from the beams in the short-beam devices, we fabricated suspended devices with the same beam length ($L_b = 50\ \mu m$) but containing pads with serpentine Pt lines in order to measure temperature of both the beams and the pads (Fig.4.9).

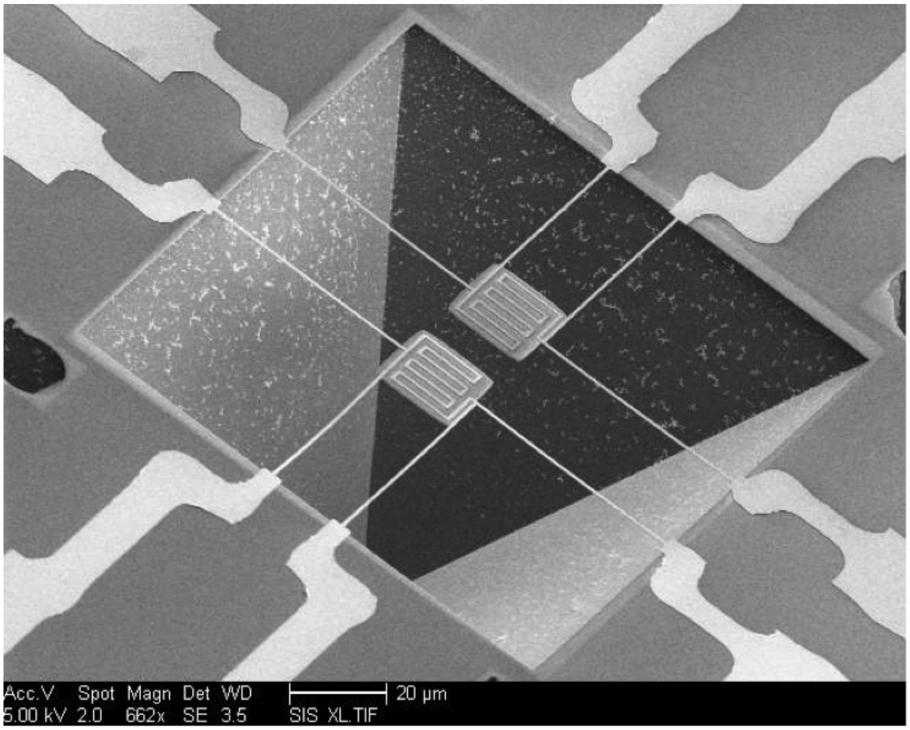

Figure 4.9: SEM image of microfabricated short-beam ($L_b = 50\ \mu m$) suspended device with pads containing serpentine Pt lines.

The average temperature rise of the self-heated beams, non-self-heated beams, and the suspended pads were measured and are plotted in Fig.(4.10). It can be shown that, for beams with negligible heat loss, the average temperature rise for the self-heated and non-self-heated beams is 2/3 and 1/2 of that for the pad, respectively, as we observed experimentally Fig.(4.10). Therefore, we have verified experimentally that the heat loss from devices with $L_b = 50\ \mu m$ is negligible at room temperature.

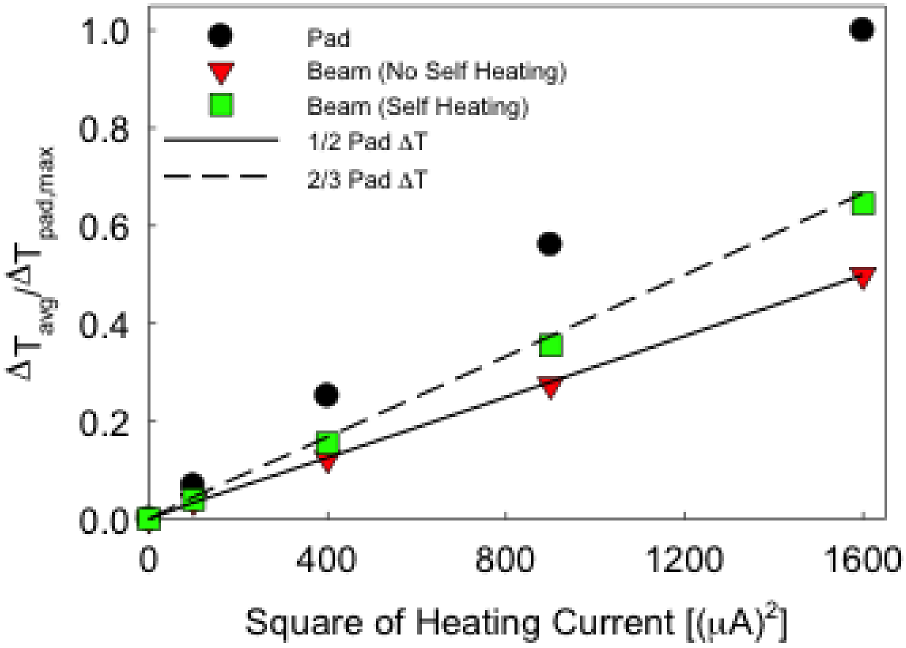

Figure 4.10: Average measured temperature rise of suspended pad and suspending beams for two cases, self-heating (green square) and no self-heating (red triangle). Dashed and solid lines represent 2/3 and 1/2 of the pad temperature rise (black circle), respectively.

4.6 Power resolution of Our NbNx Calorimeter

In comparison to characteristic Pt thin films [118, 127], the TCR and κ of the NbNx beams are about four times higher and eight times lower, respectively. Hence, assuming the same device geometry and the same $\Delta T_{\max}$, the NbNx based calorimeter is expected to be approximately ten times better in power resolution, according to Eq. (4.12). (Note $Q_{res} \propto \frac{\sqrt{G}}{TCR}$)

To experimentally demonstrate the superior power resolution of the NbNx based calorimeter, we used the same setup shown in Fig. 4.1(a) to measure the small heat flux (modulated at 2ω) transferred from the heating beam to the sensing beam via thermal radiation. The temperature rise of the sensing beam, which also oscillates at 2ω, can be determined from [28]

$$\Delta T_s = \frac{2\sqrt{2}V_{2\omega}}{I_s R_s \alpha_s}, \tag{4.27}$$

where $V_{2\omega}$ is the measured 2ω voltage from the sensing beam, and I_s is the sensing current (in DC) applied to the bridge. The amplitude of the current was chosen such that the maximum temperature rise, $\Delta T_{\max}$, on the sensing beam is the same as in our prior study on Pt based calorimeter (~10 K) to facilitate a direct comparison between NbNx and Pt. The bandwidth (Δf) of the measurement was set to be 7.8 mHz, also the same as in our prior study [28].

Figure 4.11 shows the power resolution of the calorimeter. When the heat flux transferred to the sensing side is very low, the measured temperature is within the noise floor (or NET), which is determined to be about 50 μK.

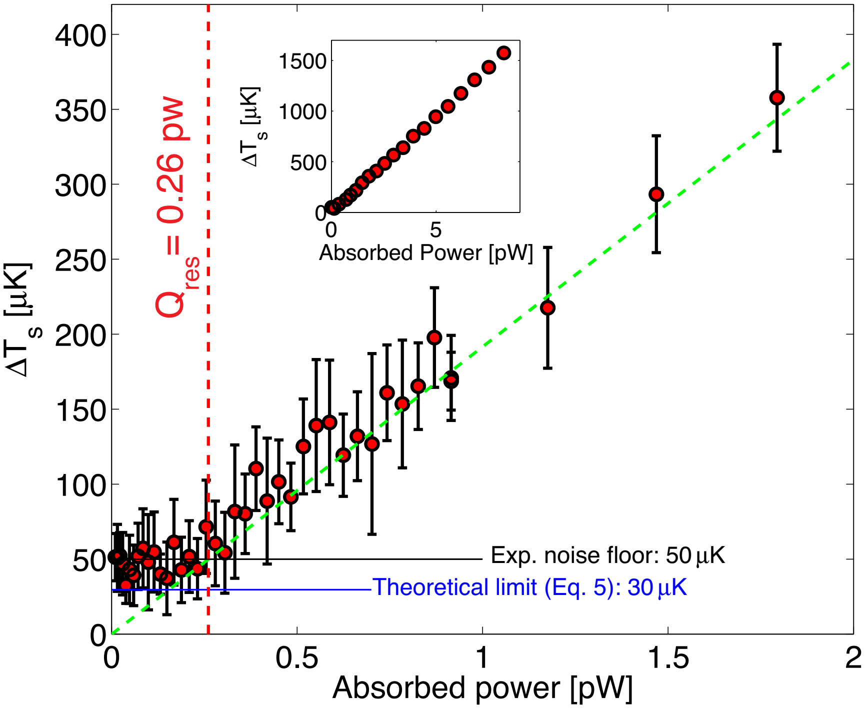

Figure 4.11: Measured sensing side temperature as a function of the heat power transferred to the sensing beam. The red circles are the measurement ΔT_s at a given absorbed power and the error bars represent the standard deviation. The noise floor of the ΔT_s measurement (NET) is approximately 50 μK, which is close to the theoretical instrumental limit of our resistive thermometer (30 μK, determined from Eq. (4.11)). The NET of 50 μK corresponds to a calorimetry resolution (Q_{res}) of only 0.26 pW, as shown by the red vertical dashed-line.

The NET values with different applied sensing current (I_{DC}) and frequency also demonstrates that a smaller current and lower frequency yield a larger NET.

In Fig.4.12, the NET is higher when the heating power is modulated at a lower frequency, which is resulted from larger $1/f$ thermal drift at lower frequency. As shown in these plots, for heating frequency of 1.5 Hz, the NET is approximately 75 μK, higher than the NET of $\sim$50 μK at 4 Hz. Likewise, NETs at higher frequencies (8 Hz and 18 Hz) are lower, getting closer to the Johnson noise limit, but the signal attenuation is significant at these frequencies (as shown in Fig. 4.4).

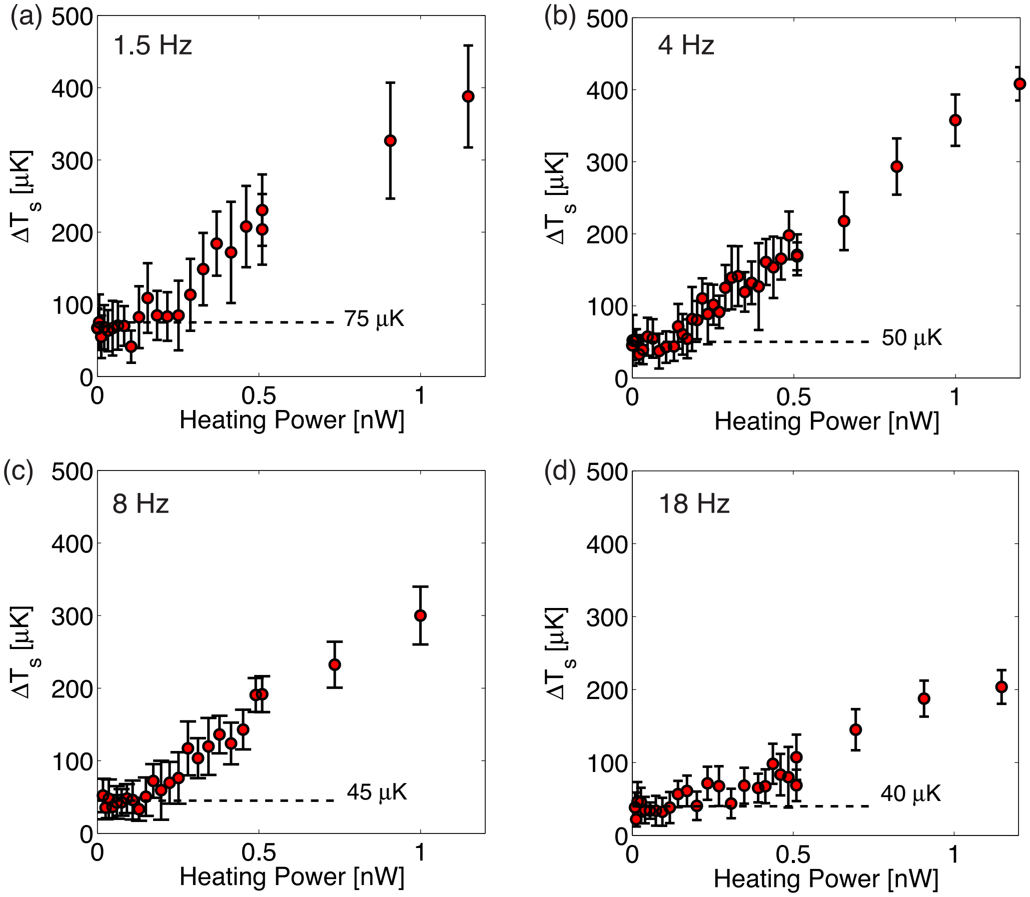

Figure 4.12: Sensing side temperature with different joule heating power to determine the NET at different frequencies: (a) 1.5 Hz, (b) 4 Hz, (c) 8 Hz, and (d) 18 Hz.

As shown in Fig.4.13, since $NET \propto 1/I_s$, a lower NET is expected with a higher sensing current. Our measurements indeed showed that when the sensing current was doubled, the NET was reduced by approximately half (from 90 μK to 45 μK).

With the measured NET of ∼50 μK and G of 5.22 nW/K of the beam, the Q_{res} for the NbNx device is determined to be ∼0.26 pW. In comparison to Pt resistive thermometry with similar geometry and $\Delta T_{\max}$, which exhibits a resolution of 2.5 pW [28], our device demonstrated an order of magnitude improvement in calorimetry resolution, which is consistent with our prior expectation based on the TCR and κ of the NbNx beam. Compared to the state-of-the-art calorimeters, namely, bi-material cantilevers [125] and Pt resistive thermometers [27,28], the device demonstrated here shows an unprecedented resolution using the simple resistive thermometry platform, thanks to the high TCR and low κ of the NbNx thermometer.

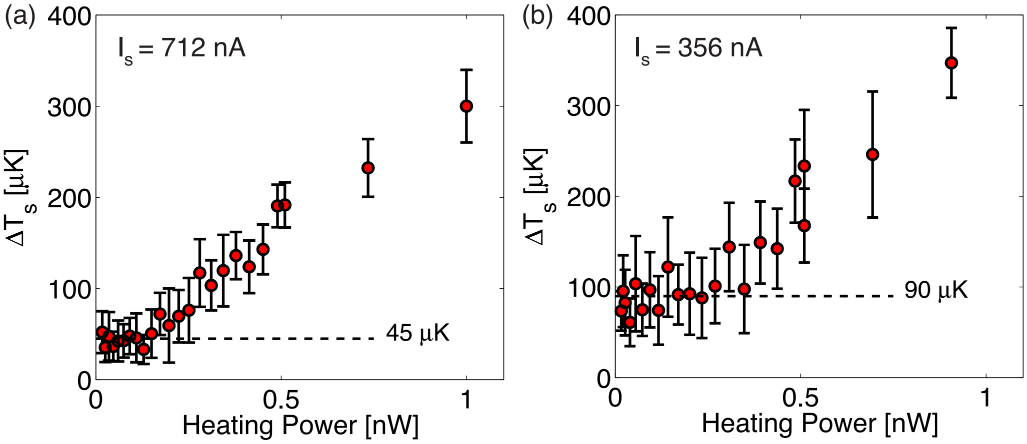

Figure 4.13: Measured sensing side temperature rise vs. heating power at different applied sensing current of (a) 712 nA and (b) 356 nA.

4.7 Conclusion

We demonstrated a calorimeter with a power resolution of 0.26 pW, which is the lowest among the calorimeters reported to date. Similar to previous works [27,28], the intrinsic and extrinsic noises in resistive thermometry are minimized to Johnson's noise level by employing a modulated heating technique and a Wheatstone bridge circuit. The substantial improvement in resolution is attributed to the NbNx thermometry material, which exhibits a high TCR and a low κ. The platform described here will find wide-range applications, where high-resolution calorimetry is desirable, such as nanoscale heat transport and biological phenomena including single cell metabolic rate measurements.

Chapter 4, in part, is a reprint of the material in Review Scientific Instruments, 2013, Jianlin Zheng, Matt Wingert, Edward Dechaumphai, and Renkun Chen. The dissertation author was the primary investigator and the co-first author of this paper.

Chapter 4, in part, is a reprint of the material in Review Scientific Instruments, 2014, Edward Dechaumphai and Renkun Chen. The dissertation author was the primary investigator and the first author of this paper.

Chapter 5

Calorimetry for Biological Applications

5.1 Introduction

Cell metabolism is fundamentally linked to various essential biological processes such as cell growth, differentiation, motility, survival, death, etc. Cell metabolic rate can be measured with calorimeters that directly detect the heat production due to cell metabolism. However, past experiments that investigated the calorimetric property of cells is predominantly performed with bulk amount of cells, where the average measured property of an ensemble of cells is assumed to represent the property of a single cell. Moreover, recent studies, which utilized a drastic advancement in instrumentations and technologies, reveal inhomogeneous characteristics of individual cells among the cell populations [138–141]. Metabolic rate thus differentiates one cell type from the other. Even among a given cell type, not all cells are metabolically homogeneous. Minority cells, which go undetected in bulk measurement as depicted in Fig.(5.1), can be crucial to the function of bulk cells as a whole.

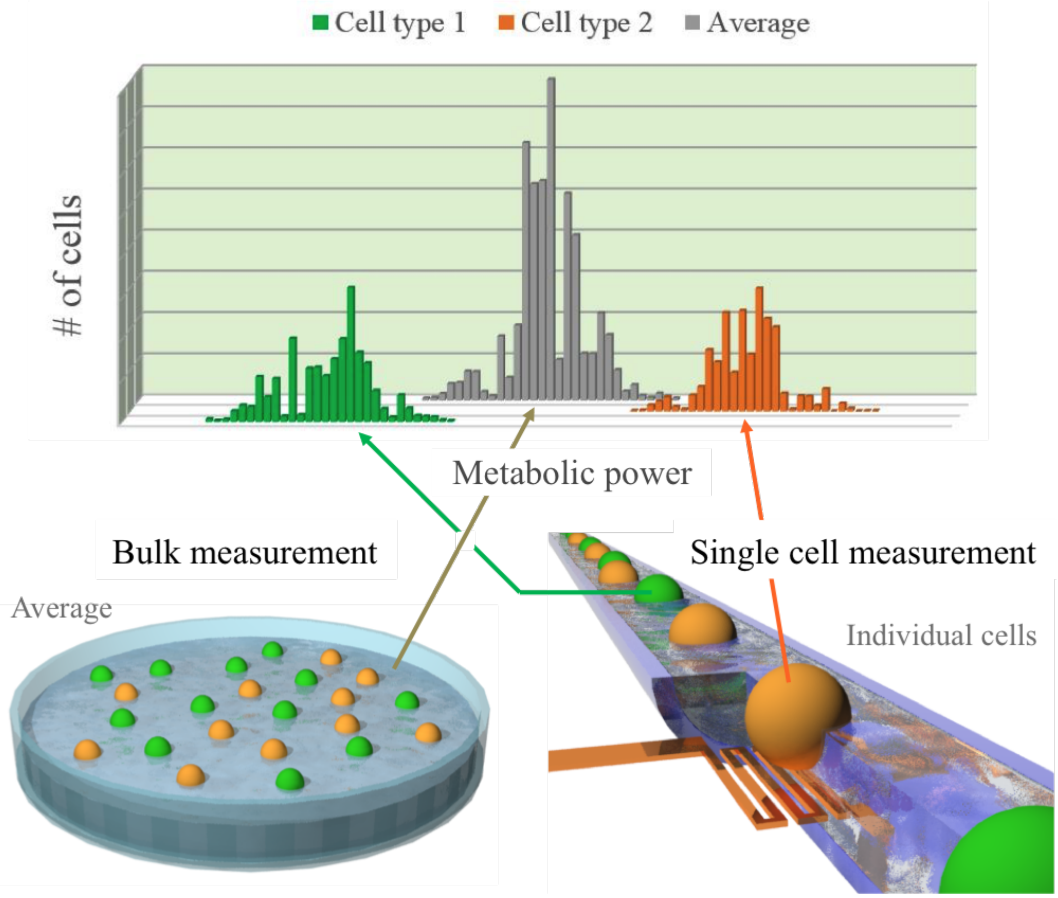

Figure 5.1: A hypothetical comparison between metabolic rate measurements of bulk and single cells. A bulk measurement, which assumes homogeneous properties, could be misleading because it displays an average value (gray bar graph), whereas the single cell measurement can distinguish two population types with vastly different values (orange and green color). Many research works have shown heterogeneity within a cell population, where the 'subordinate' population could be crucial to the function of the whole ensembles. Therefore, this level of details in probing properties of single cell is necessary for a deeper understanding of single cell metabolism.

One notable example elucidating the importance of single cell metabolic rate measurement is cancer. Cancer is well known for its heterogeneity. For instance in kidney tumor, researchers have found that the exome among 20 cancer cells are vastly diverse [138]. Because of the varying properties within one colony of cancer cells, targeted therapy is extremely challenging [142–145]. Therefore, understanding each individual cancer cells is crucial in unraveling the mystery of cancer. Moreover, the major difference between cancer cells and normal cells is their metabolic rates. Due to the transformation in metabolic process in cancer cells such as from mitochondrial oxidative phosphorylation to aerobic glycolysis known as the Warburg effect [146], many biomedical researches have focused on comprehending the metabolic process of a cancer cell and finding methods to reverse the metabolic activity back to a normal cell [146–154]. An instrumentation that can provide a facile measurement of the metabolic rate of individual cancel cells would provide timely feedback for evaluating the various metabolic regulation methods. Undoubtedly, one can potentially harness this difference in metabolic rates between normal and cancer cells for cancer diagnostics.

Currently, several single cell metabolomics measurement techniques are employed to measure metabolites such as mass spectrometry and fluorescence technique in single cells, particularly cancer cells [139, 155–160]. Even though these techniques are useful in grasping the metabolic process of single cells, they are invasive, expensive and time-consuming. For example, in the fluorescence technique, one has to find a specific cell binder that has proper fluorescence property that can be activated with metabolites from the cells [155, 158, 160]. As stated, because cancer cells are not homogenous, finding a specific binder that is also generalized for the majority of certain types of cells is challenging. Moreover, exerting the chemicals into the cells can potentially contaminate the cells and influence the obtained results. Another popular method in many laboratories, the single- cell mass spectrometry technique [139, 156–159], is an invasive process where the technique requires metabolites to be extracted, which damages the cell during the preparation process [158]. Mass spectrometry is then performed to measure the amount of metabolites from the extracted sample. Such invasive process makes it infeasible to monitor cell metabolic activities in real time when responded to different environmental stimuli (e.g., temperature) and interrogations (e.g., drugs) [158].

Direct calorimetry, on the other hand, can probe the metabolic rate quantitatively in terms of amount of generated heat power. One main advantage of calorimetry over the other metabolomics techniques discussed above (fluorescence and mass-spectroscopy) is it is a label-free technique that can continuously monitor living cells in well-controlled fluidic (cell culture) environments. This is advantageous considering living organisms are dynamic in nature. In fact, metabolic rates of ensembles (bulk amount) of cells have been measured in the past using calorimeters, which revealed important insights of cell metabolism, for instance, the correlation between metabolic rates vs. cell size (namely, the allometric scale [124, 161, 162]), and the difference in metabolic rates between normal and cancer cells [149–152, 163, 164].

However, there is no calorimeter to date that is sensitive enough to measure single cell metabolic rates (long term measurement in minutes range, which is a more useful measurements than a short term measurement) as summarized in Fig.(5.2). Although, some groups have reported few cells metabolic rate measurements such as brown fat cells but still need to stimulate them to obtain sufficient metabolic rate for the device to detect [171]. As shown in Fig.(5.2), the state-of-the-art closed chamber calorimeters, either commercially available or developed in laboratories, possess the power resolution as low as 4.2 nW, which was demonstrated by Roukes group [116]. However, this resolution is based on a short-term noises from Johnson noise and/or white noise, where long-term signal drifts are not considered. When thermal drift is considered, the minimum detectable power of biocalorimeters reported could be as high as ∼ 50 nW. The metabolic rate of single cells, however, ranges from 1 pW to few nW depending on the types and sizes of cells (e.g, brown fat adipose cells have one of the higher rates at 950 pW [166], while typical human cells have a rate around ∼60 pW). It is clear that the resolution of today's calorimeters has to be improved by at least an order of magnitude to be able to resolve metabolic rate of a wide range of cells (Fig.(5.2)). More importantly, a biocalorimeter should be able to demonstrate a long-term stability for at least few hours for it to be useful.

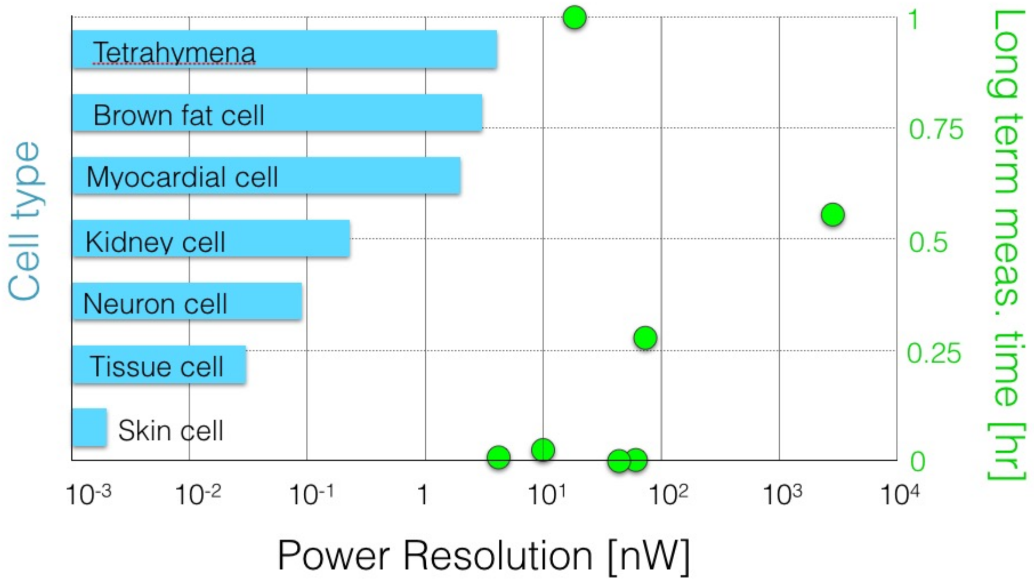

Figure 5.2: Metabolic rate of single cells in comparison to the sensitivity of reported closed-chamber biocalorimeters based on short-term noise (from raw data of the reported literatures from references [116,165,167–172]), not a long term minimum detectable power. Measurement time to monitor metabolic rate of cells requires at least several hours. Therefore, long-term noise or drift should provide a more accurate representation of the minimum detectable power of a biocalorimeter, which has not yet been demonstrated.

Given the potential to probe each individual single cell and a strong dependence of cell behavior to the metabolic process, single-cell biocalorimeter with pW to nW resolution will open up a wide range of possible fundamental research to answer biological questions and provide an excellent platform for future biomedical applications. It is this vast potential as well as the one to two-order of magnitude gap in heat resolution that motivate us to develop single cell biocalorimeters. As the first stepping stone toward single cell metabolic rate measurement, in this work, we began with improving the long-term sensitivity of biocalorimeter to nanowatt-sensitivity.

5.2 Recap on Sensitivity of Calorimeter

As discussed in Chapter 1, the sensitivity of the calorimeter relies on two factors: 1) the thermal conductance of the calorimeter to the thermal reservoir (G), and 2) the minimum detectable temperature (ΔT_{min}). In other word, $Q_{\mathrm{min}} = G \times \Delta T_{\mathrm{min}}$.

To minimize Q_{min}, parasitic heat loss must be minimized. The parasitic heat loss can come from 3 different heat transfer modes: conduction, convection, and radiation. In this chapter, how the heat loss from each heat transfer modes are reduced will be discussed. The other element toward enhancing Q_{min} is to have a low detectable ΔT limit. ΔT_{min} depends on both the signal to noise ratio (short term ΔT_{res}) and the long term T stability influenced by thermal drift (long term $\Delta T_{\mathrm{drift}}$). A simple approach to minimize thermal noise and drift will be explored in this chapter.

Developing calorimeter to measure metabolic rate of cells poses different challenges in comparison to developing calorimeter to study nanoscale materials such as our previous work on NbNx calorimeter. In biocalorimeter, the criteria that must be met are:

1. The calorimeter must be compatible with cells. For that reason, the mi-

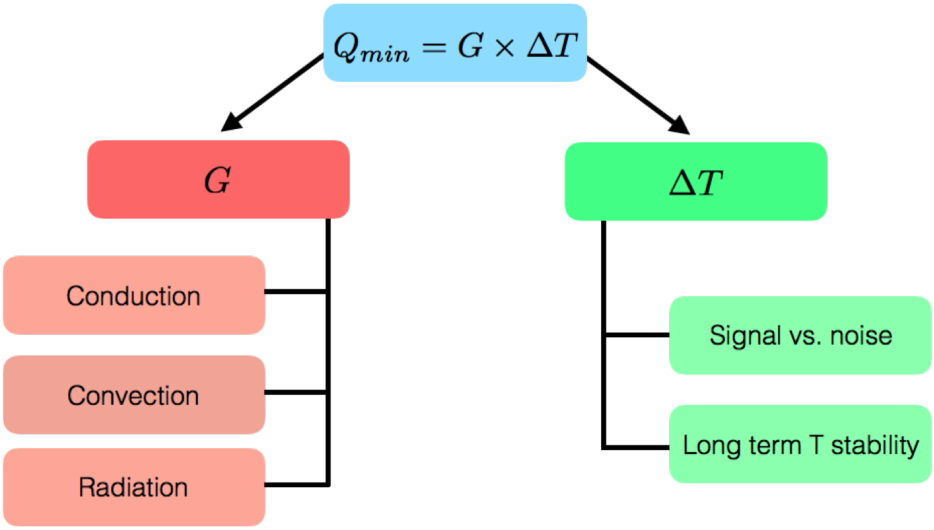

Figure 5.3: Factors in developing high resolution calorimeter

crofluidics platform must be integrated into the design such that the chamber can nurture cells.

2. The set-up must have a capability to visualize the cells inside the microfluidics during the measurement.

3. The thermal signal from cells is non-modulated (assuming cells do not generate frequency dependent heating). Therefore, we cannot use modulated temperature detection with lock-in at a specific frequency as we did to eliminate other noises in our NbNx device. Therefore, the set up for the metabolic rate measurement must have a very high temperature stability such that the ΔT_{min} is not influence by the environment or outside temperature.

4. The geometry of the biocalorimeter will be dictated by the size of the cells of interest. Because a typical cell size ranges from one μm to hundreds of μm, the cross-sectional area will be much larger than most chip-based calorimeter, which increases G due to larger conduction heat loss.

5. To reduce the heat loss due to conduction, the length of the biocalorimeter

must be longer.

6. The entire microfluidic system must be a closed-loop fluidic circuit and vacuum-tight since high vacuum is necessary to eliminate convective heat transfer as will be discussed later in this chapter.

As a proof of concept demonstration, we started with monitoring the metabolic rate of Tetrahymena Thermophilia mainly due to its high metabolic rate (bulk microcalorimetric measurements reported ∼3-5 nW per cell [173–176]) and ease in culturing since they can survive in a wide range of conditions [177, 178]. Our design of biocalorimeter hinges on the size of Tetrahymena, which is approximately $40 - 50$ μm in diameter.

5.3 Low Conductance biocalorimeter: Suspended Microfluidic-based Calorimeter

To minimize conduction, a 1D suspended structure is employed similar to our work on NbNx [29]. For a single beam, the thermal conductance due to conduction G_{cond} is

$$G_{cond} = \frac{\kappa A_c}{L} \tag{5.1}$$

Our cross-sectional area is restricted by the size of Tetrahymena. Therefore, the cross-sectional geometry of the microfluidics channel is designed to be approximately 50 μm by 40 μm in height and width. To reduce G_{cond}, the biocalorimeter is fabricated from parylene, since parylene has an intrinsically low thermal conductivity. Although, if the microfluidics channel is filled with medium (which has water as its main ingredient), the conductive heat loss will be dominated by the medium.

From a heat conduction point of view, a longer beam yields a lower the thermal conductance ($G_{cond} \propto 1/L$). However, as the length of the beam is longer, the surface area of the suspended microfluidic channel will increase. This larger surface area will lead to larger heat loss along the surfaces from convective and radiative heat transfer modes. A convective heat transfer can be simply removed by placing the device inside a high vacuum environment. In our experiment, our chamber system can bring the pressure down to below 5×10^{-6} Torr, which is more than sufficient to eliminate convection [116]. However, the radiative heat loss is more challenging to reduce because radiative heat transfer requires no medium, and only depends on the emissivity properties of the beam and the temperature of the environment and the sample. In short, the radiation heat transfer coefficient [W m^{-2}K^{-1}] can be expressed as:

$$h_{rad} = \epsilon\sigma\left(T_s + T_\infty\right)\left(T_s^2 + T_\infty^2\right), \tag{5.2}$$

where ϵ is the emissivity of beam, σ is the Stefan-Boltzmann constant, T_s is the temperature at the surface of the beam, and T_∞ is the surrounding temperature. In a case when $T_s - T_\infty$ is small, the radiation heat transfer coefficient can be approximated as

$$h_{rad} = 4\epsilon\sigma T_{\text{avg}}^3, \tag{5.3}$$

where T_{avg} is the average temperature between the beam and the surrounding. The heat loss from radiation can be generally estimated as $G_{rad} = h_{rad}A_s$, where A_s is the surface area. Consequently, the heat loss from radiation will increase linearly with increase in length assuming the cross-sectional parameter is constant throughout the beam. Comparing the effect of L on G_{cond} and G_{rad}, $G_{cond} \propto 1/L$ and $G_{rad} \propto L$ for a 1D suspended beam. Therefore, heat loss from radiation needs to be taken into account. Although, these two heat transfer modes are coupled together and a specific case in thermal analysis needs to be considered, where the total thermal conductance is not simply a summation of G_{rad} and G_{cond}.

The effective thermal conductance of the device when there is a point heat source in the middle of the beam can be estimated to model G when there is a cell in the middle. For simplicity in order to gain an insight on the heat loss of the suspended microfluidics calorimeter, a suspended beam with a uniform cross-sectional area having a point heat source as the boundary condition as shown in Fig.(5.4) will be analyzed here.

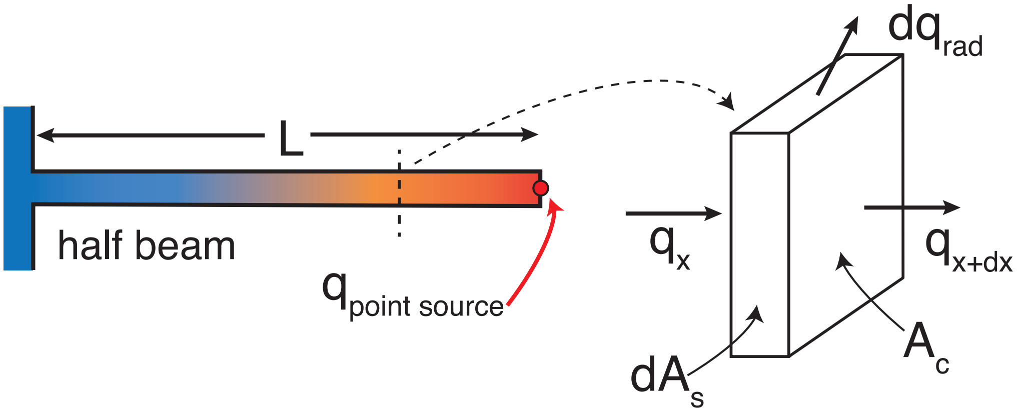

Figure 5.4: A Schematic of the 1D suspended beam with a uniform cross-section experiencing a point source

From the conservation of energy law, the energy balance for the differential element (Fig.(5.4)) can be written as

$$q_x = q_{x+dx} + dq_{rad}, \tag{5.4}$$

where

$$\begin{aligned} q_x &= -\kappa A_c \frac{dT}{dx}, && (5.5)\\ q_{x+dx} &= q_x + \frac{dq_x}{dx}dx \\ &= -\kappa A_c \frac{dT}{dx} - \kappa \frac{d}{dx}\left(A_c \frac{dT}{dx}\right) dx, && (5.6)\\ dq_{rad} &= h dA_s (T - T_\infty), && (5.7) \end{aligned}$$

where q_x is the heat transfer rate [W] into the differential element, q_{x+dx} is the heat transfer rate [W] out of the differential element, κ is the thermal conductivity of the beam, A_c is the cross-sectional area of the beam, h is the radiation heat transfer coefficient [W m^{-2}K^{-1}], dA_s is the differential surface area of the element, T is the temperature of the element, and T_∞ is the ambient temperature.

By substitute Equations (5.5), (5.6), and (5.7) into Eq.(5.4), the new expression can be written as,

$$\cancel{-\kappa A_c \frac{dT}{dx}} = \cancel{-\kappa A_c \frac{dT}{dx}} - \kappa \frac{d}{dx}\left(A_c \frac{dT}{dx}\right) dx + h dA_s (T - T_\infty), \tag{5.8}$$

then divide all sides by κdx to get

$$0 = -\frac{d}{dx}\left(A_c \frac{dT}{dx}\right) + \frac{h}{\kappa dx} dA_s \left(T - T_\infty\right). \tag{5.9}$$

Assuming A_c is a constant, the $dA_s = P dx$, where P is the cross-section parameter, then the equation can be simplified and rearranged as

$$0 = \frac{d^2 T}{dx^2} - \frac{hP}{\kappa A_c}\left(T - T_\infty\right). \tag{5.10}$$

Now, let $T(x) - T_\infty = \theta(x)$, which means $\frac{d\theta}{dx} = \frac{dT}{dx}$. Eq.(5.14) can be rewritten as

$$\begin{aligned} 0 &= \frac{d^2\theta(x)}{dx^2} - \frac{hP}{\kappa A_c}\theta(x) && (5.11)\\ 0 &= \frac{d^2\theta(x)}{dx^2} - m^2\theta(x), && (5.12) \end{aligned}$$

where $m = \sqrt{\frac{hP}{\kappa A_c}}$. Eq.(5.12) is a linear, homogeneous second-order differential equation with a general solution in the form of:

$$\theta(x) = C_1 \mathrm{e}^{mx} + C_2 \mathrm{e}^{-mx}, \tag{5.13}$$

and

$$\frac{d\theta(x)}{dx} = mC_1 \mathrm{e}^{mx} - mC_2 \mathrm{e}^{-mx}. \tag{5.14}$$

As shown in Fig.(5.4), the boundary conditions are:

a) at $x = 0$, $\theta(0) = 0$.

b) at $x = L$, $\frac{d\theta(x)}{dx} = \frac{q}{\kappa A_c}$. When applying boundary condition from a), then $C_2 = C_1$. Boundary condition (b) is applied to solve for C_1 and C_2 by substitute (b) into Eq.(5.14):

$$\frac{q}{\kappa A_c} = mC_1 \mathrm{e}^{mL} - mC_2 \mathrm{e}^{-mL}, \tag{5.15}$$

Then,

$$\begin{aligned} C_1 &= \frac{q}{\kappa A_c m\left(\mathrm{e}^{mL} - \mathrm{e}^{-mL}\right)}, && (5.16)\\ C_2 &= -\frac{q}{\kappa A_c m\left(\mathrm{e}^{mL} - \mathrm{e}^{-mL}\right)}. && (5.17) \end{aligned}$$

Therefore, the analytical solution for the temperature profile of a suspended beam with a point source at a boundary can be rearranged and expressed as

$$\theta(x) = \left(\frac{q}{\kappa A_c m}\right)\left(\frac{\mathrm{e}^{mx} - \mathrm{e}^{-mx}}{\mathrm{e}^{mL} + \mathrm{e}^{-mL}}\right) \tag{5.18}$$

The analysis above resembles a fin model having a point source at the end of the beam. However, on our device, the point sources are composed of two beams. For a beam with a cell in the middle and a metabolic rate of Q_c, half of the Q_c will go to one of the half beam and the other goes to the other half beam due to symmetry. In other word, $q = Q_c/2$ in Eq.(5.18) and L **is the half length of the total length** of the suspended microfluidic bridge. The temperature profile of half of the beam (from the edge with $T = T_\infty$ to the middle of the bridge) is

$$\theta(x) = \left(\frac{Q_c/2}{\kappa A_c m}\right)\left(\frac{\mathrm{e}^{mx} - \mathrm{e}^{-mx}}{\mathrm{e}^{mL} + \mathrm{e}^{-mL}}\right), \tag{5.19}$$

where the analytical solution is plotted in Fig.(5.5).

Because of the the surface conductance (hA_s), θ as a function of position x is not linear. When the cell is in the middle, $x = L$ (which is also $\theta_{\max}$), then

$$\theta_{\max} = \left(\frac{Q_c/2}{\kappa A_c m}\right)\left(\frac{\mathrm{e}^{mL} - \mathrm{e}^{-mL}}{\mathrm{e}^{mL} + \mathrm{e}^{-mL}}\right). \tag{5.20}$$

Therefore, the thermal conductance G resulted from a point source from heating power of a cell in the middle of the beam (or end of the half beam) is

$$G = 2m\kappa A_c\left(\frac{\mathrm{e}^{mL} + \mathrm{e}^{-mL}}{\mathrm{e}^{mL} - \mathrm{e}^{-mL}}\right), \tag{5.21}$$

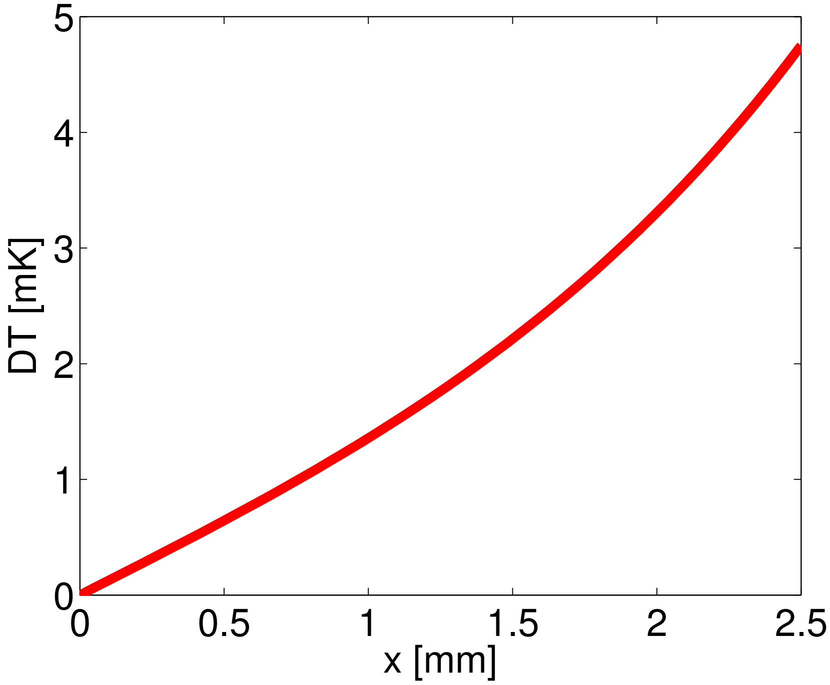

Figure 5.5: Analytical solution to a suspended beam with a uniform cross-section and a point source boundary condition. In this calculation, the total length is 5 mm (half length is 2.5 mm), width of the beam is 50 μm, height of the beam is 50 μm, ϵ is 0.5, κ is 0.6 W m^{-1}K^{-1}, T_∞ is 303.15 K, and Q_c is 10 nW.

in which $m = \sqrt{\frac{hP}{\kappa A_c}}$.

The thermal conductance as a function of different half beam length resulted from a point source is plotted in Fig.(5.6) to get a visual sense of the effect of radiation. The conductance calculated here does not represent the actual calorimeter, butt to provide a coarse insight on the thermal problem we are looking at. In Fig.(5.6), the width of the beam is 50 μm, height of the beam is 50 μm, κ is 0.6 W m^{-1}K^{-1}, and T_∞ is 303.15 K,

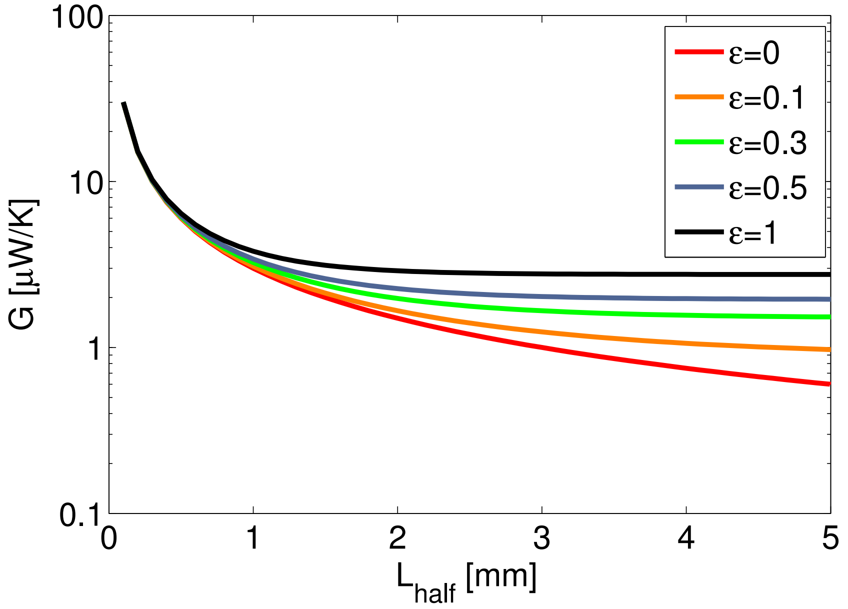

Figure 5.6: G of a 1D calorimeter as a function of different designed half length (L_{half}) for different emissivity values.

5.4 Designing Biocalorimeter and Microfluidics

Our biocalorimeter design is illustrated in Fig.(5.7). The design composes of a suspended microfluidics, a platinum heater line, and a 4 junctions Bi/Pt thermopiles.

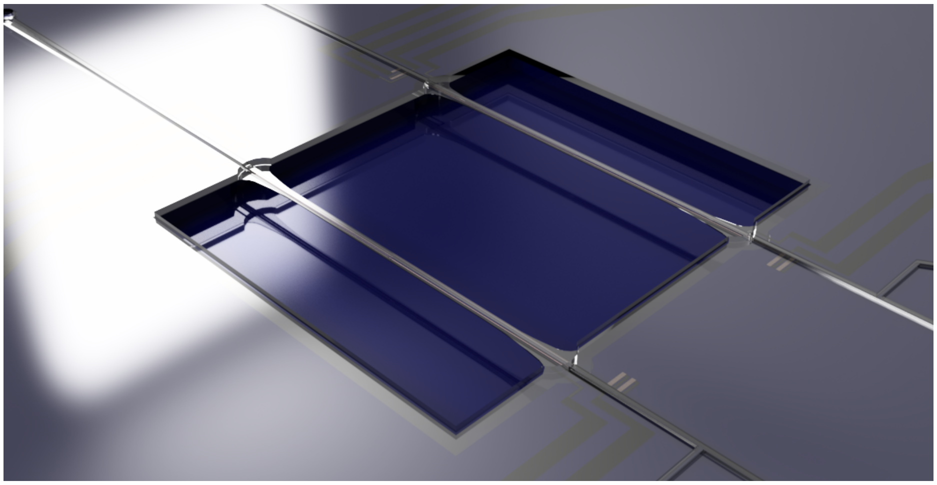

Figure 5.7: A schematic of the biocalorimeter

There are many types of thermometers that can be employed in a biocalorimeter such as Pt or NbNx that we have used previously. However, one of the drawbacks in resistive-based thermometer is that one needs to apply large enough current to get a sufficient sensitivity, which leads to heating of the suspended microfluidics channel due to Joule heating. On the other hand, thermopile-based thermometer does not pose such problems. For that reason, in this work, we selected Bi/Pt as our thermopile materials, in which Bi also has a relatively high Seebeck coefficient, while platinum is simple to process because it is inert to many chemicals and gases.

Thermopile-based thermometer generates voltage when there is a difference between the reference junction and the sensing junction. How much the thermopile generates voltage depends on the Seebeck coefficient of the materials.

For thermopile, the theoretical temperature resolution (ΔT) depends on the Seebeck coefficient and Johnson noise, where

$$\begin{aligned} \Delta T_{res,theoretical} &= \frac{\text{Johnson voltage noise}}{\text{Voltage generates by thermopile}} \\ \Delta T_{res,theoretical} &= \frac{\sqrt{4k_{\mathrm{B}}RT\Delta f}}{nS_{junc}}, \end{aligned} \tag{5.22}$$

where S_{junc} is the Seebeck coefficient between a junction, n is the number of junctions, and R is the total resistance of the thermopile. Eq.(5.22) shows that large Seebeck coefficient between a junction, number of junctions, and low electrical resistance will lead to a finer temperature resolution. Therefore, an ideal materials for thermopile thermometer should have large power factor, $PF = \frac{S^2}{\rho}$, where ρ is the electrical resistance of the material. Note that ΔT_{res} is proportional to $\frac{\sqrt{R}}{S}$). Examples of materials with large power factor are bismuth telluride, antimony telluride, bismuth antimony telluride, etc. In our biocalorimeter, Bismuth has a fairly high Seebeck ($\sim$50–70 μV/K) compare to most metal-based thermopile.

Although, in instrumentations, due to small generated voltage signals from the thermopile alone, these thermopile signals are needed to be conditioned through external circuits such as low noise amplifiers. The minimum short term electrical noises can then be dominated by op-amp or other circuitry instead of Johnson noise. Therefore, careful instrumentation and design to minimize noises from electronics must be carried out. One important consideration when determining what is the smallest short-term signal one can confidently detect is: **the true minimum noise or ΔT_{res} must be characterized from the signal output**, not from short-term white noise (such as Johnson noise) or input noise measurements.

As mentioned previously, the convective heat loss must be eliminated and can be realized by placing the sample in a high vacuum environment. Another challenge in implementing vacuum to the sample is the integration between microfluidic platform and the vacuum set up. How the microfluidic set up is isolated from the vacuum is summarized in Fig.(5.8). A custom-made clamp made from our CNC machine acts as a fluidic interface to supply fluids from outside of the chamber to the sample and a sample holder to press the sample for a good thermal contact between the sample and the temperature-controlled stage.

To input fluids, PEEK tubes are connected to a syringe (manual or automatic). The tube is extended into the chamber through our custom-made vacuum feedthrough (Fig.(5.9)). The feedthrough is sealed with ultra-high vacuum epoxy, which turns into ceramic after curing.

The PEEK tube from the feedthrough is then connected to the clamp (Fig.(5.10)).

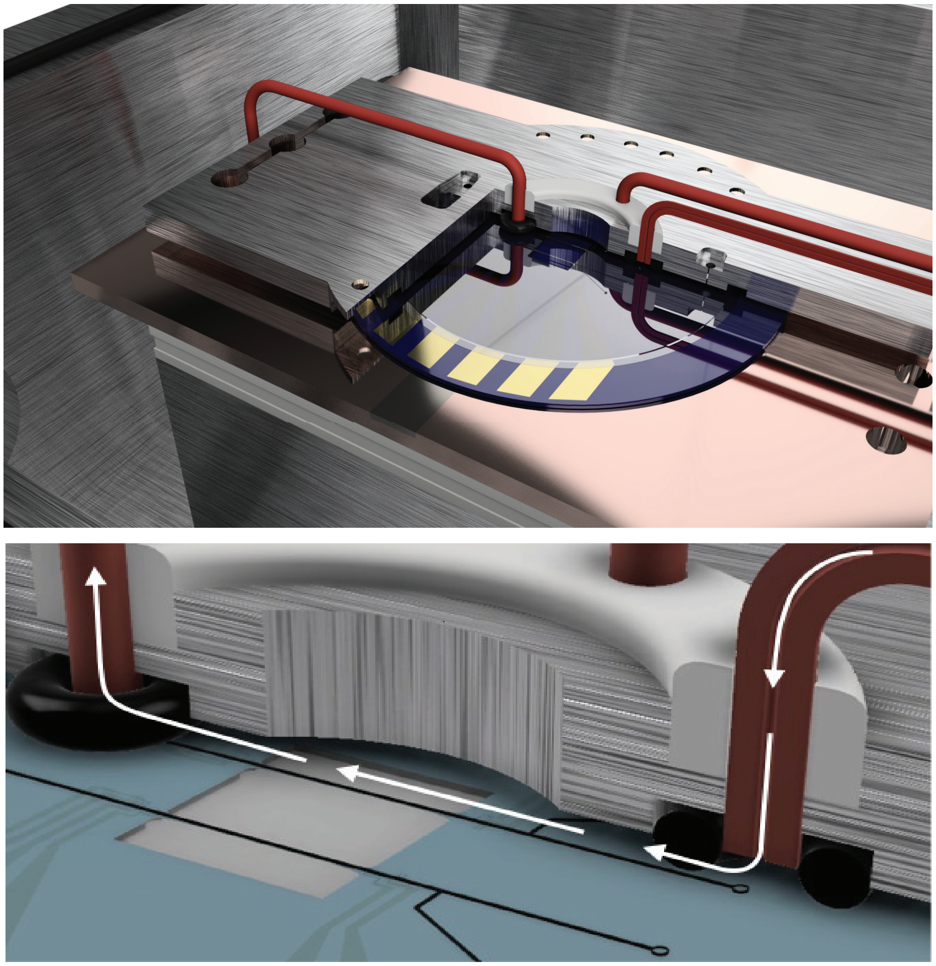

Figure 5.8: Vacuum-compatible microfluidic set-up

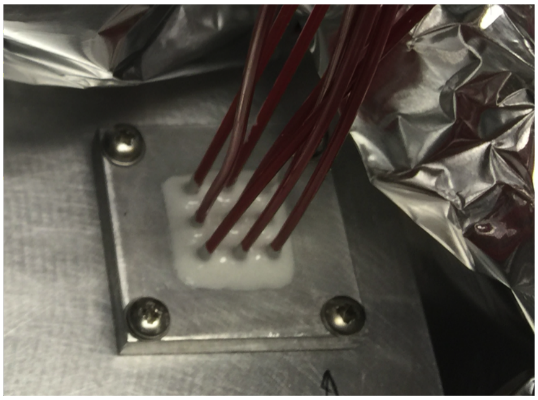

Figure 5.9: High-vacuum microfluidics feedthrough

To seal the tubes (or fluidic pathway) from the vacuum, o-ring is used to interface fluidics between the clamp and the sample. The clamp is then pressed/hold in place by the screws, which produce downward pressures to the o-rings. The compressed o-rings then deform and seal the interfaces between the sample (SU-8 inlet/outlet) and the PEEK tubes that are connected to clamp.

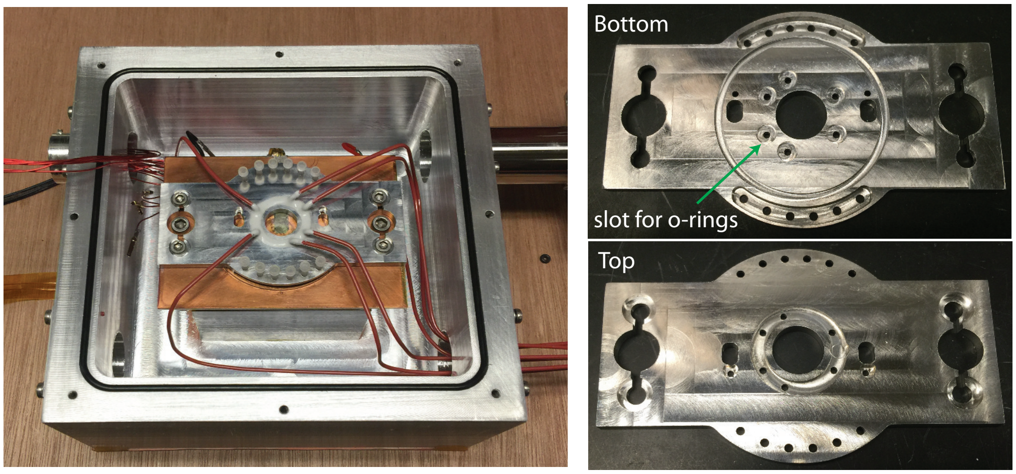

Figure 5.10: Clamp for holding the sample and for vacuum-compatible microfluidics set-up

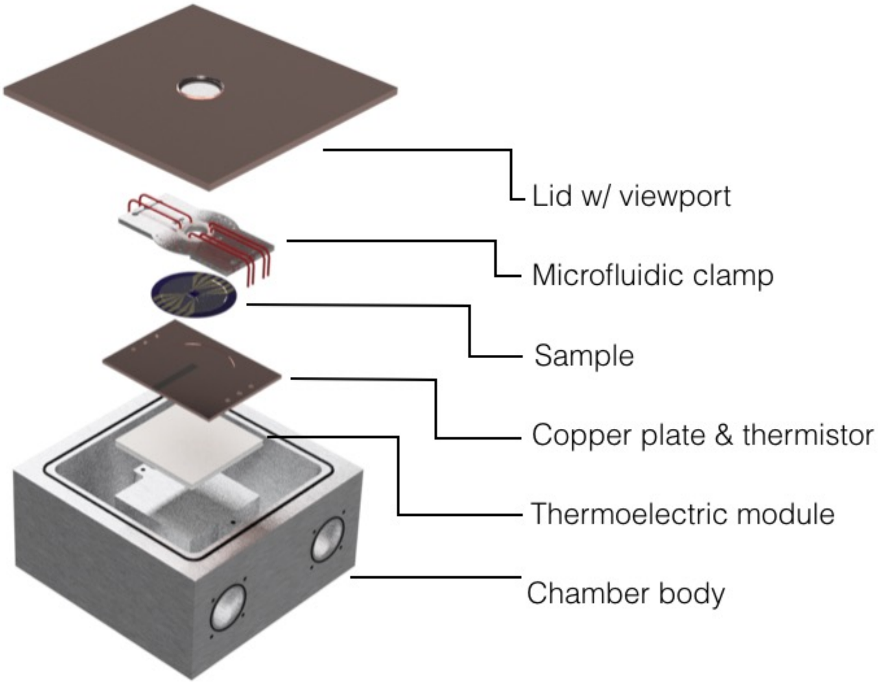

Figure 5.11: An illustration of the vacuum-compatible microfluidics set-up

With this vacuum-compatible microfluidics set up (illustrated in Fig.(5.11)), the pressure inside the chamber is measured to be below 5×10^{-6} Torr, which demonstrates that our set up can achieve high vacuum and convective heat loss can be eliminated. Fig.(5.12) shows a single Tetrahymena cell swimming inside a suspended microfluidic channel under vacuum environment. Note that the cell is alive and medium does not evaporates under vacuum because of the vacuum-tight closed-microfluidics channel system.

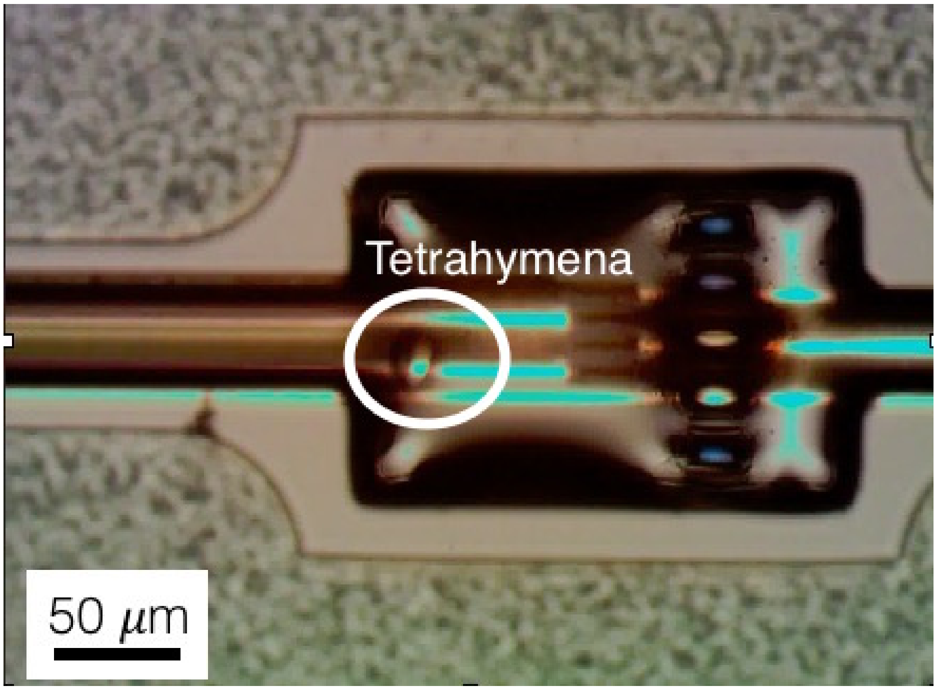

Figure 5.12: An individual Tetrahymena inside a suspended microfluidic channel under vacuum.

5.5 Engineering Long-Term Sub-mK Temperature Stability Platform

In order to be able to detect small temperature changes from the cell, we first must understand the nature of the temperature or heat signal from cells. Metabolic rate of a cell is not a modulate signal, which is analogous to DC signal in electrical circuit. This also points to the fact that we cannot "lock-in" a frequency to eliminate external noises. Because of this, the instrumentation implemented in our biocalorimetry must be able to shield the external electrical and temperature noises from the environment as much as possible.

The simplest way to seclude the calorimetric electrical signal from the external noises is to use an amplifier such that the amplified signal is larger. Although, because the signal from the cell is not modulated and the signal we can retrieve is DC, then $1/f$ will dominate. As the name $1/f$ noise implied, the noise gets larger as the signal approaches DC limit. One of the ways to reduce $1/f$ electrical noise is to use a "autozero/chopper" amplifiers [179] such as CS3001, LTC1100, etc. The "autozero/chopper" amplifiers are designed such that it suppresses $1/f$ noise. To amplify a voltage signal, a non-inverting op-amp scheme is used (Fig.(5.13)) using CS3002 amplifier.

The gain of the circuit in Fig.(5.13) can be calculated as Gain $= 1 + \frac{R_2}{R_1}$, where $R_1 = 100\Omega$ and $R_2 = 75k\Omega$, which resulted in gain of 751. A low pass filter is also implemented in this scheme where the cut off frequency, f_c, is defined as $f_c = 1/(2\pi[R_1\|R_2]C_2)$. Having C_2 of 15 nF, f_c is about 106 kHz. A gain as high as 751 enable us to distinguish electrical signal from the calorimeter from the external

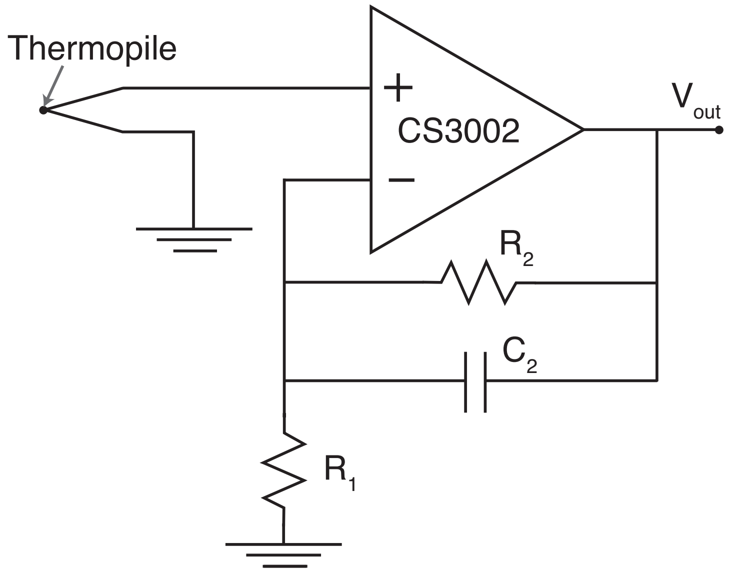

Figure 5.13: Non-inverting op-amp scheme

noises that are not part of the circuit. However, there are also other sources of noises or drift that we have to consider such as how instruments and amplifiers are influenced by the external temperature drift. The effect comes from the temperature dependent properties in materials where resistance can change with temperature or EMF voltage drop due to Seebeck effect.

A typical building temperature drifts about 1 to 3 degree celsius even when controlled by HVAC unit. Such ambient temperature drift can distort our electrical signal greatly especially since the voltage signal generate from the device is minute, where all instruments and amplifiers have input offset voltage drifts in conjunction with temperature changes. Even one of the most stable low voltage amplifiers such as CS3001, LTC1100, or AD524 has an input office voltage drift of roughly 50-500 nV/°C, in which the signal drift from ambient temperature is comparable if not higher than the voltage signal generated from 1 mK change in the sensing chamber. (The input offset voltage drift is the offset voltage before the signal is amplified.) Besides the voltage drift from the instruments or amplifiers, metal contacts at the wires at different connection points can also greatly effect the voltage drift since each contact (unless the materials are exactly the same and all reference junctions have the same temperature) will generate small voltage drop as a result of Seebeck effect and a change in temperature.

To make sure that the ambient temperature fluctuation has a minimal effect on the electrical signal generated from the biocalorimeter, we put the circuit inside the measurement chamber (Fig.(5.14)), which is temperature regulated down to milliKelvin range and is also in high vacuum. In addition, the electrodes on the wafer (sample) can be connected directly to the amplifier without having to have multiple wire connections that can easily introduce unwanted noises/signals.

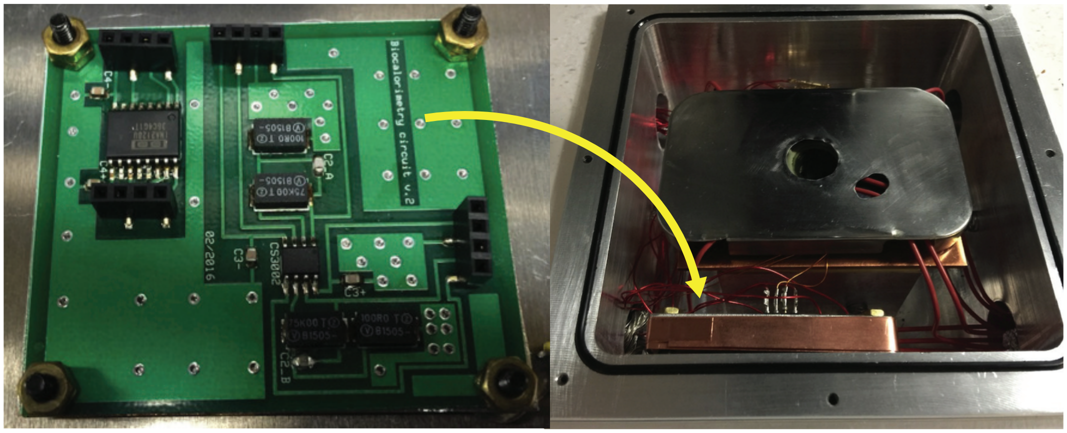

Figure 5.14: Images of the circuit board in the chamber

Even with a low-noise/drift electronics, the temperature of the calorimeter can still drift. The thermal drift can originate from (Fig.(5.15)) 1) the thermal drift at reference junctions and 2) the thermal drift from the chamber, which resulted in the radiative heat transfer on the suspended beam since the radiation depends on the temperature of the sample and the environment (chamber) temperature.

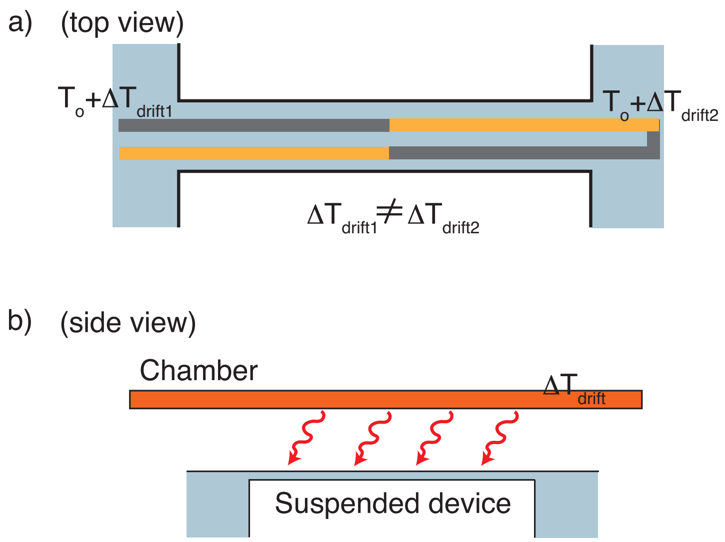

Figure 5.15: Sources of thermal drift. Thermal drifts originated from temperature fluctuation of the environment around the device. For example, (a) in a non-ideal case, the temperature at reference junctions could be different because the temperature of the thermal reservoir is not completely uniform. In addition, the temperature fluctuation of the chamber can effect the temperature stability of the beam via radiation especially since radiation plays an important role in parasitic heat loss of our device (b)

In an ideal case, the entire thermal reservoir is isothermal (temperatures at the reference junctions are identical) . However, when the temperature at the junction is no longer T_o, then the signal will also drift in corresponding to how much the junction temperature changes. To minimize this type of thermal drift, using high thermal conductivity wafer and substrate is advised such as silicon or copper since high κ material can spread the heat well and drive the temperature along the sample to be uniform. The sample (made from Si wafer) is placed on top of a copper plate that is temperature controlled by a thermoelectric module shown in Fig.(5.16). The thermoelectric module is controlled by a temperature controller, Stanford Research PTC10, which has an adjustable PID controller that can maintain at least 1 mK temperature stability at a local temperature point. Thermal grease for high-vacuum is also applied to ensure good thermal contact at the wafer.

In addition, the chamber should be isolated from the outside/ambient temperature fluctuation even though there is a vacuum around the sample. The isothermal condition will prevent any drift causes by radiation between the chamber to the sample. In our set-up, we immerse the chamber into a container filled with microencapsulated PCM (phase change material) powder from Microtek. Microencapsulated PCM is a dry powder composes of phase change material that is encapsulated inside thin polymer layers. Phase change material is great at maintain a constant temperature at the phase transition temperature because a large amount of energy is required to change the temperature at the transition point. Therefore, the PCM is kept at a near melting point such that the temperature is retained at the transition temperature. In addition, the microencapsulated PCM also has a low thermal conductivity, which helps to insulate the chamber from any outside change.

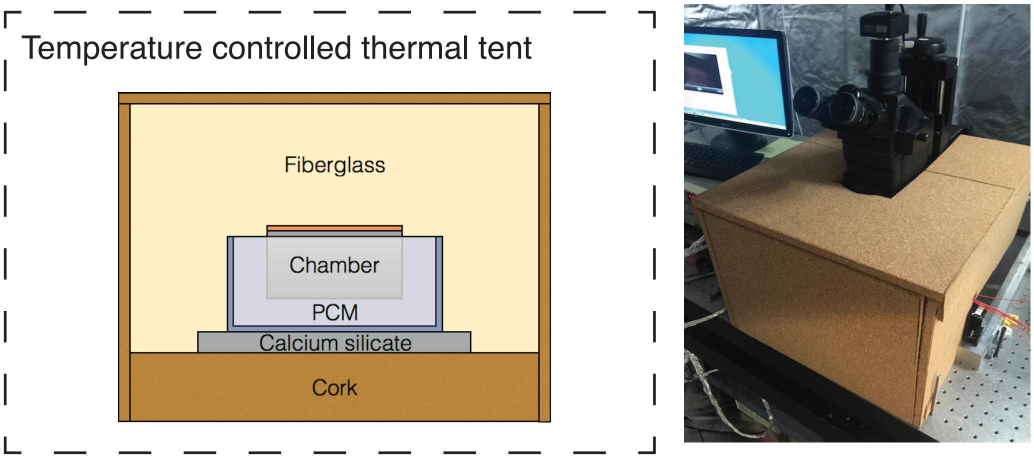

Figure 5.16: Highly stable temperature control set up

Fiberglass is also covered the entire chamber to further insulated the chamber. Not only that, the entire set-up, including the chamber and instruments such as temperature controller, nanovoltmeter, thermocouple readers, and optical table, is inside a thermal tent with a convective heater that can control the temperature of the tent to within ±0.5 °C. Fig.(5.16) illustrates and summarizes our temperature control set-up.

Besides an extensive temperature control to establish an isothermal environment, the temperature of the lid is also controlled by a heating pad with 1 mK stability. To even further reduce the influence from radiative heat transfer, two doped ITO glasses are placed on top of the clamp to act as IR radiation shields between the lid and the suspended microfluidics. Infrared range is important in radiative heat transfer for surfaces near room-temperature and doped ITO glasses have shown to have high reflectance in infrared range [180]. A quick estimation of the dominant wavelength in radiation for a surface with a temperature of T is to look at the Wien's displacement law, where $\lambda_{\max} T = 2898$ μm·K. For $T = 300K$, the dominant wavelength is 9.66 μm.

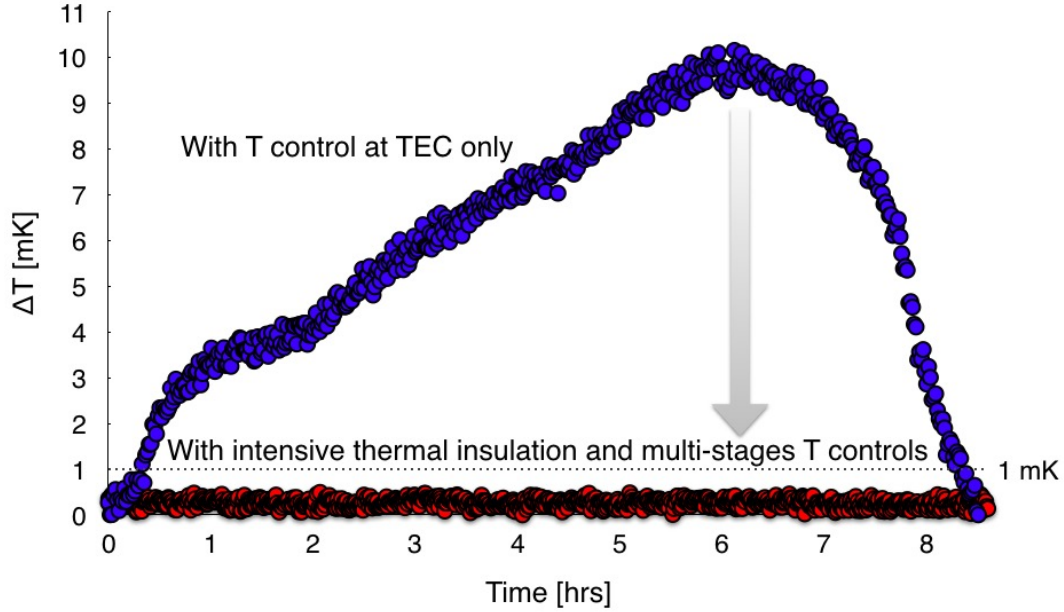

Figure 5.17: Long-term temperature stability of our device in different set-up. The blue circles represents the temperature drift over time when a device is mounted on a copper plate with temperature controlled by TEC under vacuum. The red circles are temperature drift of our device in a highly insulated set up with multiple temperature controlled stages.

The reduction in thermal drift with our extensive temperature controlled setup is shown in Fig.(5.17). With **all** of these temperature controlled features, we are able to demonstrate a long-term temperature stability down to sub-mK for at least 8 hours. The long-term temperature stability is essential in biological measurements, where the assessment time can last longer than an hour.

5.6 Fabrication Processes for Metabolic Cytometer

1. Clean wafer

2. Coat the 1st parylene layer by CVD.

3. Pattern the 1st metal layer using a standard photolithography process. Then deposit platinum thin film via sputtering. Lift off with RR41 at 350 K. This 1st metal layer is for thermopile and heater.

4. 2nd metal patterning to pattern bismuth. Bismuth is deposit by sputtering.

5. Pattern electrodes with a standard photolithography. Au is deposit by sputtering.

6. Coat the 2nd parylene layer

7. Pattern microfluidic channel using AZ P420.

8. Deposit the 3rd parylene layer.

9. Pattern etching window for suspended microfluidic channels and the inlet/outlet hole. Au is patterned and used as the etching mask when etching parylene. Parylene is etched by O_2 reactive ion etching.

10. Pattern SU-8

11. Remove sacrificial PR with PGMEA.

12. Etch silicon under the microfluidic channels to suspend the channels with XeF_2.

13. Expose electrodes by etching out top parylene on the electrode area with O_2 RIE.

SEM images of our biocalorimeter is shown in Fig.(5.18).

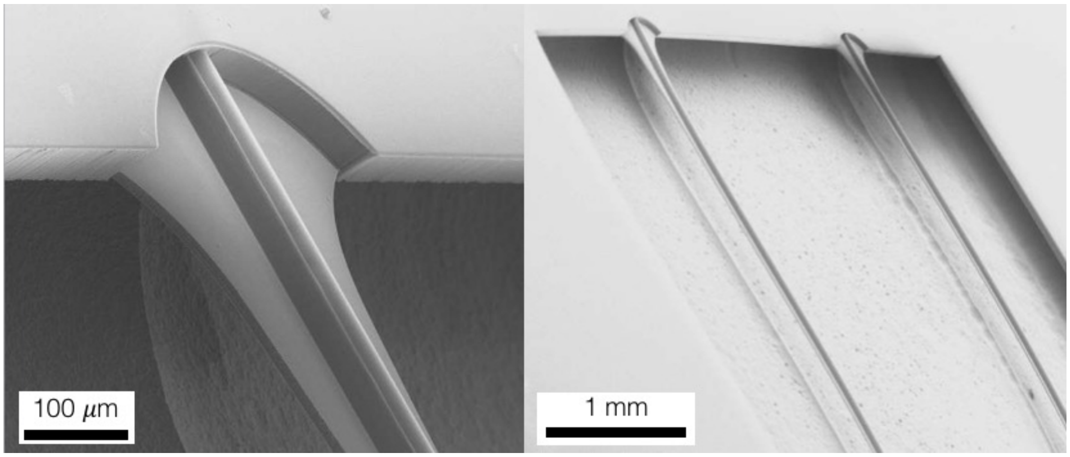

Figure 5.18: SEM images of the biocalorimeter

5.7 Device Characterization

The thermal conductance of the biocalorimeter (G) is measured by applying a DC current to the Pt heater/thermometer to generate joule heating. From joule heating, the average and the middle temperature of the beam will change depending on G. The temperature is determined from measuring the change in resistance of the Pt thermometer, where a change in temperature will alter the resistance because of the temperature coefficient of resistance of the platinum. The resistance of Pt is determined by 4-point resistance measurement, in which a low AC current is applied across two probes and the first harmonic voltage is measured across the Pt strip. From resistance change and known TCR, one can obtain average temperature as a function of applied joule heating power. At different applied joule heating power, the voltage drop across thermopile (which measures the temperature difference between the middle of the beam to the thermal reservoir) is also recorded in order to determine the total Seebeck coefficient of the thermopile.

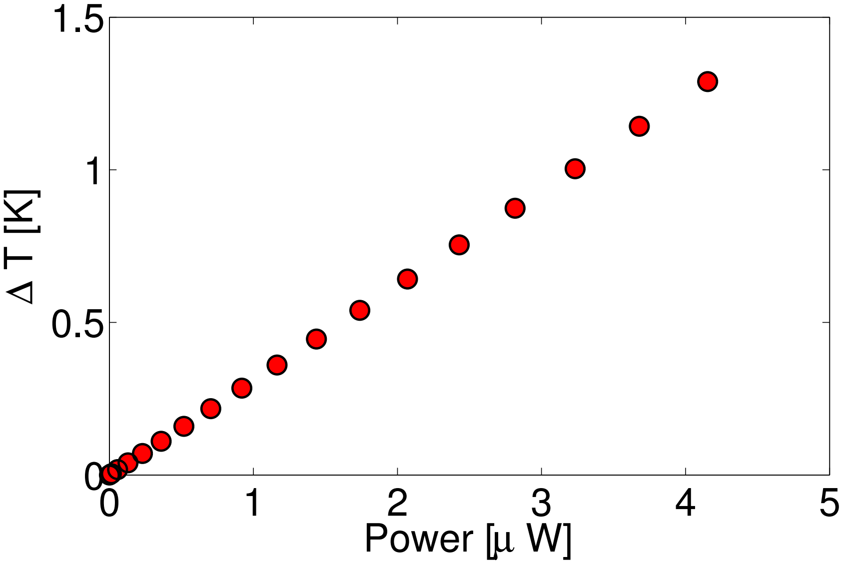

Figure 5.19: An example of a G measurement

A thermal analysis is then performed using finite element analysis (FEA) to simulate average temperature rise of the suspended microfluidics channel as a function of applied current. Finite element analysis is employed mainly because the true geometry of our biocalorimeter is not a simplistic 1D beam with a constant cross-sectional area. Hence, FEA should provide a more accurate analysis for any given geometry. The FEA results are fitted with the experiments by using κ and ϵ as the fitting parameters. Note that κ is known and can be determined from a sample with short suspended microfluidic channel, where the length is very small and radiation heat loss is negligible (see Chapter 4 for details). From fitted ϵ and κ, we can calculate the conductance in a case where there is a point source in the beam with FEA by applying a known point source to the middle of the beam and quantify the temperature differences between the chamber and thermal reservoir as shown in Fig.5.20. Then G is calculated from $G = Q/\Delta T$. Instead of point source, one can also apply a volumetric heating source to the middle sensing chamber determine G. Since the length of the beam is relatively long in comparison to the size of the sensing chamber, an analysis with a point source or a volumetric heat source should be approximately the same.

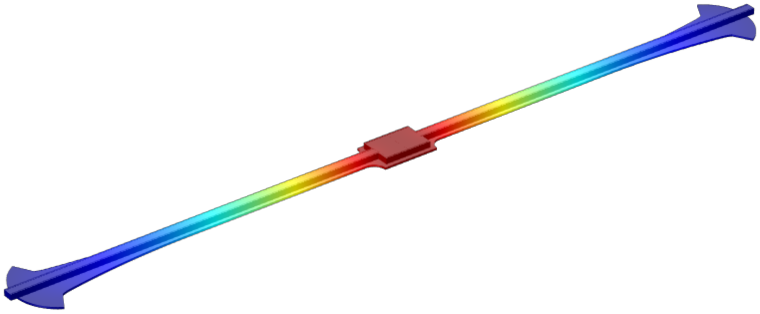

Figure 5.20: An example of a FEA to determine G by simulating temperature profile resulted by a cell-like heat source in the middle of the beam

FEA also calculates temperature profile along the suspended microfluidic channel. From the measurement and FEA calculation, one can solve for the temperature rise in the middle of the beam. By correlating the middle temperature of the beam and the voltage change (ΔV) of thermopile, Seebeck coefficient of the Bi/Pt can be determined, where $S = \Delta V / T_{\mathrm{mid}}$.

In summary, the procedure to obtain G is:

1. Applied DC current to generate Joule heating along the suspended microfluidics channel.

2. Measure changes in resistances with 4-point probe technique to determine change in average temperature ΔT_{avg}. The voltage drop across thermopile is also measured to characterize Seebeck coefficient later.

3. From applied power and ΔT_{avg} data, FEA is used to fit the experimental data by having κ and ϵ as the only fitting parameters.

4. With fitted κ and ϵ, the G is then calculated by applying the power source at the sensing chamber (to simulate metabolic rate of cell) and extracted ΔT_{calc}. Then solve for $G = Q/\Delta T$.

5. From FEA, the relationship between T_{avg} and T_{mid} can be established. The Seebeck coefficient can then be solved by associating ΔT with $\Delta V_{\mathrm{thermopile}}$.

5.8 Experiments and Results

As mentioned previously, to demonstrate our device, we selected Tetrahymena thermophilia SB210 as our biological sample due to its relatively high metabolic rate and ease in performing cell culturing. Before inputing Tetrahymena, we characterized our calorimeter and the thermal conductance was determined to be 2.9 μW/K. The ΔT_{min} of this particular device is $\sim$0.6 mK. This gives the power detection limit of 1.75 nW, with a long-term stability of more than 8 hours. The power resolution of our biocalorimeter based on short-term noise is only 0.84 nW, which is also has the finest resolution in comparison to previously reported biocalorimeter.

In this device, the total Seebeck coefficient for the device was 189 μV/K, which resulted in S of 47.25 μV/K for a Bi/Pt junction. Note that a small deviation from bulk Seebeck can be attributed to the film purity during sputtering. Plus, the Seebeck coefficient of a thin film has shown to be depended on the film deposition method and thickness.

In a cell metabolic rate measurement, a suspended microfluidics channel is filled with medium. The temperature of the device is allow to stabilize after filling the medium for at least 30 minutes before Tetrahymena cells are injected. We then slowly inject a cell with medium at a rate of approximately 1 μL per minute. The plot in Fig. 5.21 shows our measurement results of Tetrahymena metabolic rate at different time.

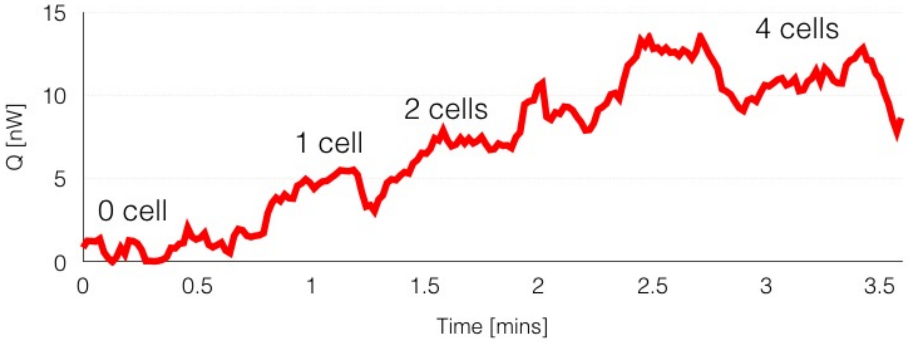

Figure 5.21: Metabolic rate monitoring of Tetrahymena

Since Tetrahymena can swim, the cell tends to move and sometimes resulted in several cells in the sensing chamber as shown in Fig. 5.21.

5.9 Conclusion and Outlook

We have demonstrated an unprecedented long-term detectable power resolution below 2 nW, which delivers a great step toward monitoring metabolic rate of single cells.

Because about half of the parasitic heat loss comes from thermal radiation, one can coat the suspended channel with a material with low emissivity at room temperature such as ITO or AZO, since these transparent conductive oxide films have high reflectance for photons with wavelength larger than micron size [180]. The important wavelength that needs to be reflected, if the temperature of the device is around 300 K, is ∼10 μm according to Wein's displacement law. By suppressing radiative heat loss, the thermal conductance should lower to ∼1.5 μW/K. In addition, the majority of the conductive heat loss comes from medium. By removing medium along the beam and create a medium bubble to nurture the cell, or reducing the cross-sectional area of the medium channel, the thermal conductance, when radiative heat loss is suppressed, can be reduced down to ∼500 nW/K.

The next step is to reduce the minimum detectable temperature. The drift can be further reduced by using a differential scheme, where identical suspended microfluidics channels are fabricated and one of the channels functions as a control. If the ambient drift between these identical suspended microfluidics channels are correlated, then these signals can be subdued by subtracting them. In addition, Bi/Pt thermopile can be replaced with a material pair with a much higher thermopower such as Bi_2Te_3/Sb_2Te_3. Electronics can also be further refined to reduce $1/f$ and instrumentation noises. By improving these aspects, one should be able to bring the minimum detectable temperature down to at least 0.1 mK. Therefore, the possible power resolution can be as fine as 50 pW, which will open up many opportunities in biomedical applications where a wider range of cells can be measured at single cell level.

Chapter 5, in part, is in a manuscript in preparation, Sahngki Hong, Edward Dechaumphai, Ratneshwar Lal and Renkun Chen. The dissertation author was the co-first author of this paper.

Chapter 6

Conclusion

This dissertation presented the applications of a calorimetry technique to investigate fundamentals of micro/nanoscale thermal transport and the development of high-resolution calorimeters for thermal and biological applications. The general overview of principles of calorimetry was introduced in Chapter 1. In a subsequent chapter (Chapter 2), the 3ω method was employed to measure the thermal conductivity of Au/Si multilayers in order to understand thermal transport across a highly mismatched interface. We demonstrated an ultralow thermal conductivity, κ, of 0.33 $\pm$ 0.04 W m^{-1}K^{-1} at room temperature with a high interfacial density of $\sim$0.2 interface nm^{-1}. The low thermal conductivity in Au/Si MLs was explained and modeled using the diffuse mismatched model (DMM) with full phonon dispersion. Our Au/Si MLs shows the lowest κ amongst inorganic MLs with κ dominated by interfacial thermal resistance. Similarly, 3ω method is utilized to characterize the near-surface regime of tungsten damaged by ion irradiation used in plasma facing components (PFCs) in fusion reactors (Chapter 3). Our experiment revealed a nearly 60% reduction in thermal conductivity in comparison to the pristine tungsten. Because PFCs undergoes an extreme steady and transient heat fluxes, our finite element analysis shows that the low κ at the near surface-regime can have a very undesirable effect to the mechanical structure of the PFCs.

The second part of this dissertation (Chapter 4 and 5) focuses on developing high-resolution calorimeters. In Chapter 4, we demonstrated the finest power resolution of the resistive calorimeter of 0.26 pW based on niobium nitride thermometer and a modulated heating with a differential scheme. From our understanding of niobium nitride-based calorimeter, we extended our calorimetry technique to biological applications. For the first time, we carried out a high vacuum platform that is compatible with the suspended microfluidics channels for detecting heat generation from cells. By minimizing parasitic heat loss and implementing high temperature stability system to the biocalorimeter, we were able to demonstrate an unprecedented both short-term and long-term power detection limit from the state-of-the-art closed-chamber biocalorimeter. This allows us to monitor metabolic rate of individual living cells cultured inside the suspended microfluidics channels.

In conclusion, the works presented in this dissertation demonstrated the applications of using calorimetry technique to study micro/nanoscale thermal transport and the approaches to push the limit of calorimeter detection limit to unlock new applications for calorimeters especially in the biomedical field.

Bibliography

[1] Avram Bar-Cohen. Thermal management of microelectronics in the 21st century. In *Electronic Packaging Technology Conference, 1997. Proceedings of the 1997 1st*, pages 29–33. IEEE, 1997.

[2] David G Cahill, Wayne K Ford, Kenneth E Goodson, Gerald D Mahan, Arun Majumdar, Humphrey J Maris, Roberto Merlin, and Simon R Phillpot. Nanoscale thermal transport. *Journal of Applied Physics*, 93(2):793–818, 2003.

[3] David G Cahill, Paul V Braun, Gang Chen, David R Clarke, Shanhui Fan, Kenneth E Goodson, Pawel Keblinski, William P King, Gerald D Mahan, Arun Majumdar, et al. Nanoscale thermal transport. ii. 2003–2012. *Applied Physics Reviews*, 1(1):011305, 2014.

[4] Li Shi, Chris Dames, Jennifer R Lukes, Pramod Reddy, John Duda, David G Cahill, Jaeho Lee, Amy Marconnet, Kenneth E Goodson, Je-Hyeong Bahk, et al. Evaluating broader impacts of nanoscale thermal transport research. *Nanoscale and Microscale Thermophysical Engineering*, 19(2):127–165, 2015.

[5] Mark H Kryder, Edward C Gage, Terry W McDaniel, William A Challener, Robert E Rottmayer, Ganping Ju, Yiao-Tee Hsia, and M Fatih Erden. Heat assisted magnetic recording. *Proceedings of the IEEE*, 96(11):1810–1835, 2008.

[6] Amy M Marconnet, Matthew A Panzer, and Kenneth E Goodson. Thermal conduction phenomena in carbon nanotubes and related nanostructured materials. *Reviews of Modern Physics*, 85(3):1295, 2013.

[7] Tao Tong, Yang Zhao, Lance Delzeit, Ali Kashani, M Meyyappan, and Arun Majumdar. Dense vertically aligned multiwalled carbon nanotube arrays as thermal interface materials. *IEEE Transactions on Components and Packaging Technologies*, 30(1):92, 2007.

[8] Virendra Singh, Thomas L Bougher, Annie Weathers, Ye Cai, Kedong Bi, Michael T Pettes, Sally A McMenamin, Wei Lv, Daniel P Resler, Todd R Gattuso, et al. High thermal conductivity of chain-oriented amorphous polythiophene. *Nature nanotechnology*, 9(5):384–390, 2014.

[9] Jungwan Cho, Zijian Li, Mehdi Asheghi, and Kenneth E Goodson. Near-junction thermal management: Thermal conduction in gallium nitride composite substrates. *Ann. Rev. Heat Transfer*, 18, 2014.

[10] Zhong Yan, Guanxiong Liu, Javed M Khan, and Alexander A Balandin. Graphene quilts for thermal management of high-power gan transistors. *Nature communications*, 3:827, 2012.

[11] HS Philip Wong, Simone Raoux, SangBum Kim, Jiale Liang, John P Reifenberg, Bipin Rajendran, Mehdi Asheghi, and Kenneth E Goodson. Phase change memory. *Proceedings of the IEEE*, 98(12):2201–2227, 2010.

[12] Geoffrey W Burr, Matthew J Breitwisch, Michele Franceschini, Davide Garetto, Kailash Gopalakrishnan, Bryan Jackson, Bülent Kurdi, Chung Lam, Luis A Lastras, Alvaro Padilla, et al. Phase change memory technology. *Journal of Vacuum Science & Technology B*, 28(2):223–262, 2010.

[13] Matthias Wuttig and Noboru Yamada. Phase-change materials for rewriteable data storage. *Nature materials*, 6(11):824–832, 2007.

[14] Yanzhong Pei, Xiaoya Shi, Aaron LaLonde, Heng Wang, Lidong Chen, and G Jeffrey Snyder. Convergence of electronic bands for high performance bulk thermoelectrics. *Nature*, 473(7345):66–69, 2011.

[15] Woochul Kim, Joshua Zide, Arthur Gossard, Dmitri Klenov, Susanne Stemmer, Ali Shakouri, and Arun Majumdar. Thermal conductivity reduction and thermoelectric figure of merit increase by embedding nanoparticles in crystalline semiconductors. *Physical Review Letters*, 96(4):045901, 2006.

[16] Kanishka Biswas, Jiaqing He, Ivan D Blum, Chun-I Wu, Timothy P Hogan, David N Seidman, Vinayak P Dravid, and Mercouri G Kanatzidis. High-performance bulk thermoelectrics with all-scale hierarchical architectures. *Nature*, 489(7416):414–418, 2012.

[17] Rama Venkatasubramanian, Edward Siivola, Thomas Colpitts, and Brooks O'quinn. Thin-film thermoelectric devices with high room-temperature figures of merit. *Nature*, 413(6856):597–602, 2001.

[18] Akram I Boukai, Yuri Bunimovich, Jamil Tahir-Kheli, Jen-Kan Yu, William A Goddard Iii, and James R Heath. Silicon nanowires as efficient thermoelectric materials. *Nature*, 451(7175):168–171, 2008.

[19] Allon I Hochbaum, Renkun Chen, Raul Diaz Delgado, Wenjie Liang, Erik C Garnett, Mark Najarian, Arun Majumdar, and Peidong Yang. Enhanced thermoelectric performance of rough silicon nanowires. *Nature*, 451(7175):163–167, 2008.

[20] Li-Dong Zhao, Shih-Han Lo, Yongsheng Zhang, Hui Sun, Gangjian Tan, Ctirad Uher, Christopher Wolverton, Vinayak P Dravid, and Mercouri G Kanatzidis. Ultralow thermal conductivity and high thermoelectric figure of merit in snse crystals. *Nature*, 508(7496):373–377, 2014.

[21] PL Richards. Bolometers for infrared and millimeter waves. *Journal of Applied Physics*, 76(1):1–24, 1994.

[22] Frank Niklaus, Christian Vieider, and Henrik Jakobsen. Mems-based uncooled infrared bolometer arrays: a review. In *Photonics Asia 2007*, pages 68360D–68360D. International Society for Optics and Photonics, 2007.

[23] Keith E Herold and Avraham Rasooly. *Biosensors and molecular technologies for cancer diagnostics*. CRC Press, 2012.

[24] O Braissant, D Wirz, B Göpfert, and AU Daniels. "the heat is on": rapid microcalorimetric detection of mycobacteria in culture. *Tuberculosis*, 90(1):57–59, 2010.

[25] D Rodríguez, AU Daniels, JL Urrusti, D Wirz, and O Braissant. Evaluation of a low-cost calorimetric approach for rapid detection of tuberculosis and other mycobacteria in culture. *Journal of applied microbiology*, 111(4):1016–1024, 2011.

[26] Li Shi, Deyu Li, Choongho Yu, Wanyoung Jang, Dohyung Kim, Zhen Yao, Philip Kim, and Arunava Majumdar. Measuring thermal and thermoelectric properties of one-dimensional nanostructures using a microfabricated device. *Journal of heat transfer*, 125(5):881–888, 2003.

[27] S Sadat, E Meyhofer, and P Reddy. Resistance thermometry-based picowatt-resolution heat-flow calorimeter. *Applied Physics Letters*, 102(16):163110, 2013.

[28] Jianlin Zheng, Matthew C Wingert, Edward Dechaumphai, and Renkun Chen. Sub-picowatt/kelvin resistive thermometry for probing nanoscale thermal transport. *Review of Scientific Instruments*, 84(11):114901, 2013.

[29] Edward Dechaumphai and Renkun Chen. Sub-picowatt resolution calorimetry with niobium nitride thin-film thermometer. *Review of Scientific Instruments*, 85(9):094903, 2014.

[30] David G Cahill. Thermal conductivity measurement from 30 to 750 k: the 3ω method. *Review of scientific instruments*, 61(2):802–808, 1990.

[31] Jung Hun Kim, Albert Feldman, and Donald Novotny. Application of the three omega thermal conductivity measurement method to a film on a substrate of finite thickness. *Journal of applied physics*, 86(7):3959–3963, 1999.

[32] T Borca-Tasciuc, AR Kumar, and G Chen. Data reduction in 3ω method for thin-film thermal conductivity determination. *Review of scientific instruments*, 72(4):2139–2147, 2001.

[33] Joseph Patrick Feser. Scalable routes to efficient thermoelectric materials. 2010.

[34] Y Sungtaek Ju, M-T Hung, MJ Carey, M-C Cyrille, and JR Childress. Nanoscale heat conduction across tunnel junctions. *Applied Physics Letters*, 86(20):203113, 2005.

[35] Zijian Li, Si Tan, Elah Bozorg-Grayeli, Takashi Kodama, Mehdi Asheghi, Gil Delgado, Matthew Panzer, Alexander Pokrovsky, Daniel Wack, and Kenneth E Goodson. Phonon dominated heat conduction normal to mo/si multilayers with period below 10 nm. *Nano letters*, 12(6):3121–3126, 2012.

[36] Elah Bozorg-Grayeli, Zijian Li, Mehdi Asheghi, Gil Delgado, Alexander Pokrovsky, Matthew Panzer, Daniel Wack, and Kenneth E Goodson. Thermal conduction properties of mo/si multilayers for extreme ultraviolet optics. *Journal of Applied Physics*, 112(8):083504, 2012.

[37] RM Costescu, DG Cahill, FH Fabreguette, ZA Sechrist, and SM George. Ultralow thermal conductivity in w/al2o3 nanolaminates. *Science*, 303(5660):989–990, 2004.

[38] A Kyarad and H Lengfellner. Al-si multilayers: A synthetic material with large thermoelectric anisotropy. *Applied physics letters*, 85, 2004.

[39] S Lee, David G Cahill, and Rama Venkatasubramanian. Thermal conductivity of si {endash} ge superlattices. *Applied physics letters*, 70(22), 1997.

[40] B Yang, JL Liu, KL Wang, and G Chen. Simultaneous measurements of seebeck coefficient and thermal conductivity across superlattice. *Applied Physics Letters*, 80(10):1758–1760, 2002.

[41] E-K Kim, S-I Kwun, S-M Lee, H Seo, and J-G Yoon. Thermal boundary resistance at ge2sb2te5/zns: Sio2 interface. *Applied Physics Letters*, 76:3864, 2000.

[42] Y Jin, A Yadav, K Sun, H Sun, KP Pipe, and M Shtein. Thermal boundary resistance of copper phthalocyanine-metal interface. *Applied physics letters*, 98(9):093305, 2011.

[43] Jun Liu, Byunghoon Yoon, Eli Kuhlmann, Miao Tian, Jie Zhu, Steven M George, Yung-Cheng Lee, and Ronggui Yang. Ultralow thermal conductivity of atomic/molecular layer-deposited hybrid organic–inorganic zincone thin films. *Nano letters*, 13(11):5594–5599, 2013.

[44] Wee-Liat Ong, Sara M Rupich, Dmitri V Talapin, Alan JH McGaughey, and Jonathan A Malen. Surface chemistry mediates thermal transport in three-dimensional nanocrystal arrays. *Nature materials*, 12(5):410–415, 2013.

[45] Mark D Losego, Ian P Blitz, Richard A Vaia, David G Cahill, and Paul V Braun. Ultralow thermal conductivity in organoclay nanolaminates synthesized via simple self-assembly. *Nano letters*, 13(5):2215–2219, 2013.

[46] Xiaojia Wang, Christopher D Liman, Neil D Treat, Michael L Chabinyc, and David G Cahill. Ultralow thermal conductivity of fullerene derivatives. *Physical Review B*, 88(7):075310, 2013.

[47] David G Cahill, Susan K Watson, and Robert O Pohl. Lower limit to the thermal conductivity of disordered crystals. *Physical Review B*, 46(10):6131, 1992.

[48] Ho-Ki Lyeo and David G Cahill. Thermal conductance of interfaces between highly dissimilar materials. *Physical Review B*, 73(14):144301, 2006.

[49] Ruxandra M Costescu, Marcel A Wall, and David G Cahill. Thermal conductance of epitaxial interfaces. *Physical Review B*, 67(5):054302, 2003.

[50] RJ Stoner, HJ Maris, TR Anthony, and WF Banholzer. Measurements of the kapitza conductance between diamond and several metals. *Physical Review Letters*, 68(10):1563, 1992.

[51] Eric T Swartz and Robert O Pohl. Thermal boundary resistance. *Reviews of modern physics*, 61(3):605, 1989.

[52] Andrew N Smith, John L Hostetler, and Pamela M Norris. Thermal boundary resistance measurements using a transient thermoreflectance technique. *Microscale Thermophysical Engineering*, 4(1):51–60, 2000.

[53] JC Duda, C-YP Yang, BM Foley, R Cheaito, DL Medlin, RE Jones, and PE Hopkins. Influence of interfacial properties on thermal transport at gold: silicon contacts. *Applied Physics Letters*, 102(8):081902, 2013.

[54] Charles Kittel. *Introduction to solid state physics*. Wiley, 2005.

[55] Pramod Reddy, Kenneth Castelino, and Arun Majumdar. Diffuse mismatch model of thermal boundary conductance using exact phonon dispersion. *Applied Physics Letters*, 87(21):211908, 2005.

[56] S Min Lee and David G Cahill. Heat transport in thin dielectric films. *Journal of applied physics*, 81(6):2590–2595, 1997.

[57] John M Poate. Diffusion and reactions in gold films. *Gold Bulletin*, 14(1):2–11, 1981.

[58] Tadashi Ishida, Yuuki Nakajima, Junji Endo, Dominique Collard, and Hiroyuki Fujita. Real-time transmission electron microscope observation of gold nanoclusters diffusing into silicon at room temperature. *Nanotechnology*, 20(6):065705, 2009.

[59] David G Cahill, My Katiyar, and JR Abelson. Thermal conductivity of a-si: H thin films. *Physical review B*, 50(9):6077, 1994.

[60] David G Cahill, Henry E Fischer, Tom Klitsner, ET Swartz, and RO Pohl. Thermal conductivity of thin films: measurements and understanding. *Journal of Vacuum Science & Technology A*, 7(3):1259–1266, 1989.

[61] BL Zink, R Pietri, and F Hellman. Thermal conductivity and specific heat of thin-film amorphous silicon. *Physical review letters*, 96(5):055902, 2006.

[62] Baowen Li, Jinghua Lan, and Lei Wang. Interface thermal resistance between dissimilar anharmonic lattices. *Physical review letters*, 95(10):104302, 2005.

[63] David G Cahill and RO Pohl. Lattice vibrations and heat transport in crystals and glasses. *Annual Review of Physical Chemistry*, 39(1):93–121, 1988.

[64] SI Anisimov, BL Kapeliovich, and TL Perelman. Electron emission from metal surfaces exposed to ultrashort laser pulses. *Zh. Eksp. Teor. Fiz*, 66(2):375–377, 1974.

[65] Arun Majumdar and Pramod Reddy. Role of electron-phonon coupling in thermal conductance of metal-nonmetal interfaces. *Applied Physics Letters*, 84(23):4768–4770, 2004.

[66] Jose Ordonez-Miranda, JJ Alvarado-Gil, and Ronggui Yang. The effect of the electron-phonon coupling on the effective thermal conductivity of metal-nonmetal multilayers. *Journal of Applied Physics*, 109(9):094310, 2011.

[67] Piyush Singh, Myunghoon Seong, and Sanjiv Sinha. Detailed consideration of the electron-phonon thermal conductance at metal-dielectric interfaces. *Applied Physics Letters*, 102(18):181906, 2013.

[68] Rogier HM Groeneveld, Rudolf Sprik, and Ad Lagendijk. Femtosecond spectroscopy of electron-electron and electron-phonon energy relaxation in ag and au. *Physical Review B*, 51(17):11433, 1995.

[69] Zhibin Lin, Leonid V Zhigilei, and Vittorio Celli. Electron-phonon coupling and electron heat capacity of metals under conditions of strong electron-phonon nonequilibrium. *Physical Review B*, 77(7):075133, 2008.

[70] SD Brorson, A Kazeroonian, JS Moodera, DW Face, TK Cheng, EP Ippen, MS Dresselhaus, and G Dresselhaus. Femtosecond room-temperature measurement of the electron-phonon coupling constant γ in metallic superconductors. *Physical Review Letters*, 64(18):2172, 1990.

[71] Wei Wang, David G Cahill, et al. Limits to thermal transport in nanoscale metal bilayers due to weak electron-phonon coupling in au and cu. *Physical review letters*, 109(17):175503, 2012.

[72] MI Kaganov, IM Lifshitz, and LV Tanatarov. Relaxation between electrons and the crystalline lattice. *Soviet Physics Jetp-Ussr*, 4(2):173–178, 1957.

[73] Dong-Wook Oh, Seok Kim, John A Rogers, David G Cahill, and Sanjiv Sinha. Interfacial thermal conductance of transfer-printed metal films. *Advanced Materials*, 23(43):5028–5033, 2011.

[74] RJ Stoner and HJ Maris. Kapitza conductance and heat flow between solids at temperatures from 50 to 300 k. *Physical Review B*, 48(22):16373, 1993.

[75] Chris Dames and Gang Chen. Theoretical phonon thermal conductivity of si/ge superlattice nanowires. *Journal of Applied Physics*, 95(2):682–693, 2004.

[76] Patrick E Hopkins. Multiple phonon processes contributing to inelastic scattering during thermal boundary conductance at solid interfaces. *Journal of Applied Physics*, 106(1):013528, 2009.

[77] Patrick E Hopkins, John C Duda, and Pamela M Norris. Anharmonic phonon interactions at interfaces and contributions to thermal boundary conductance. *Journal of Heat Transfer*, 133(6):062401, 2011.

[78] John C Duda, Patrick E Hopkins, Justin L Smoyer, Matthew L Bauer, Timothy S English, Christopher B Saltonstall, and Pamela M Norris. On the assumption of detailed balance in prediction of diffusive transmission probability during interfacial transport. *Nanoscale and Microscale Thermophysical Engineering*, 14(1):21–33, 2010.

[79] Max Born and Kun Huang. *Dynamical theory of crystal lattices*. Clarendon Press, 1954.

[80] Frank Herman. Lattice vibrational spectrum of germanium. *Journal of Physics and Chemistry of Solids*, 8:405–418, 1959.

[81] VK Thakur and TN Singh. Lattice dynamics of fcc metals. *physica status solidi (b)*, 135(1):67–73, 1986.

[82] Siqing Wei and MY Chou. Phonon dispersions of silicon and germanium from first-principles calculations. *Physical Review B*, 50(4):2221, 1994.

[83] JW Lynn, HG Smith, and RM Nicklow. Lattice dynamics of gold. *Physical Review B*, 8(8):3493, 1973.

[84] G Nilsson and G Nelin. Study of the homology between silicon and germanium by thermal-neutron spectrometry. *Physical Review B*, 6(10):3777, 1972.

[85] WA Kamitakahara, CM Soukoulis, HR Shanks, U Buchenau, and GS Grest. Vibrational spectrum of amorphous silicon: Experiment and computer simulation. *Physical Review B*, 36(12):6539, 1987.

[86] Joseph L Feldman, Mark D Kluge, Philip B Allen, and Frederick Wooten. Thermal conductivity and localization in glasses: Numerical study of a model of amorphous silicon. *Physical Review B*, 48(17):12589, 1993.

[87] Joseph L Feldman, Philip B Allen, and Scott R Bickham. Numerical study of low-frequency vibrations in amorphous silicon. *Physical Review B*, 59(5):3551, 1999.

[88] M Grimsditch, W Senn, G Winterling, and MH Brodsky. Brillouin scattering from hydrogenated amorphous silicon. *Solid State Communications*, 26(4):229–233, 1978.

[89] R Vacher, H Sussner, and M Schmidt. Attenuation of surface phonons in opaque materials measured by brillouin scattering. *Solid State Communications*, 34(5):279–281, 1980.

[90] SI Tan, BS Berry, and BL Crowder. Elastic and anelastic behavior of ion-implanted silicon. *Applied Physics Letters*, 20(2):88–90, 1972.

[91] IR Cox-Smith, HC Liang, and RO Dillon. Sound velocity in amorphous films of germanium and silicon. *Journal of Vacuum Science & Technology A*, 3(3):674–677, 1985.

[92] LR Testardi and JJ Hauser. Sound velocity in amorphous ge and si. *Solid State Communications*, 21(11):1039–1041, 1977.

[93] NW Pu and TC Li. Pulse-echo measurement of longitudinal sound velocity in nanometer thin films. *Applied Physics B*, 82(3):449–453, 2006.

[94] Xiao Wang Zhou, Reese E Jones, Christopher James Kimmer, John C Duda, and Patrick E Hopkins. Relationship of thermal boundary conductance to structure from an analytical model plus molecular dynamics simulations. *Physical Review B*, 87(9):094303, 2013.

[95] ES Landry and AJH McGaughey. Thermal boundary resistance predictions from molecular dynamics simulations and theoretical calculations. *Physical Review B*, 80(16):165304, 2009.

[96] John C Duda, Pamela M Norris, and Patrick E Hopkins. On the linear temperature dependence of phonon thermal boundary conductance in the classical limit. *Journal of Heat Transfer*, 133(7):074501, 2011.

[97] Lei Wang and Baowen Li. Reduction of thermal conductivity of anharmonic lattices. *Physical Review B*, 74(13):134204, 2006.

[98] Lifa Zhang, Jing-Tao Lü, Jian-Sheng Wang, and Baowen Li. Thermal transport across metal–insulator interface via electron–phonon interaction. *Journal of Physics: Condensed Matter*, 25(44):445801, 2013.

[99] T Hirai and G Pintsuk. Thermo-mechanical calculations on operation temperature limits of tungsten as plasma facing material. *Fusion engineering and design*, 82(4):389–393, 2007.

[100] Jochen Max Linke, Takeshi Hirai, Manfred Rödig, and Lorenz Anton Singheiser. Performance of plasma-facing materials under intense thermal loads in tokamaks and stellarators. *Fusion science and technology*, 46(1):142–151, 2004.

[101] Takeshi Hirai, Koichiro Ezato, and Patrick Majerus. Iter relevant high heat flux testing on plasma facing surfaces. *Materials Transactions*, 46(3):412–424, 2005.

[102] Y Kikuchi, D Nishijima, M Nakatsuka, K Ando, T Higashi, Y Ueno, M Ishihara, K Shoda, M Nagata, T Kawai, et al. Surface damage characteristics of cfc and tungsten with repetitive elm-like pulsed plasma irradiation. *Journal of Nuclear Materials*, 415(1):S55–S58, 2011.

[103] Th Loewenhoff, A Bürger, J Linke, G Pintsuk, A Schmidt, L Singheiser, and C Thomser. Evolution of tungsten degradation under combined high cycle edge-localized mode and steady-state heat loads. *Physica Scripta*, 2011(T145):014057, 2011.

[104] VA Makhlaj, IE Garkusha, SV Malykhin, AT Pugachov, I Landman, J Linke, S Pestchanyi, VV Chebotarev, and VI Tereshin. Residual stresses in tungsten under exposures with iter elm-like plasma loads. *Physica scripta*, 2009(T138):014060, 2009.

[105] T Hirai, G Pintsuk, J Linke, and M Batilliot. Cracking failure study of iter-reference tungsten grade under single pulse thermal shock loads at elevated temperatures. *Journal of Nuclear Materials*, 390:751–754, 2009.

[106] Theodore L Bergman, Frank P Incropera, and Adrienne S Lavine. *Fundamentals of heat and mass transfer*. John Wiley & Sons, 2011.

[107] Yasuhisa Oya, Masashi Shimada, Makoto Kobayashi, Takuji Oda, Masanori Hara, Hideo Watanabe, Yuji Hatano, Pattrick Calderoni, and Kenji Okuno.

Comparison of deuterium retention for ion-irradiated and neutron-irradiated tungsten. *Physica Scripta*, 2011(T145):014050, 2011.

[108] James F. Ziegler. http://srim.org.

[109] American Society for Testing and Materials. *Standard Practice for Neutron Radiation Damage Simulation by Charged-Particle Irradiation, E521-96, Annual Book of ASTM Standards*, volume 12.02. American Society for Testing and Materials, Philadelphia, 1996.

[110] RW Powell, Cho Yen Ho, and Peter Edward Liley. Thermal conductivity of selected materials. Technical report, DTIC Document, 1966.

[111] AT Peacock, V Barabash, W Dänner, M Rödig, P Lorenzetto, P Marmy, M Merola, BN Singh, S Tähtinen, J Van Der Laan, et al. Overview of recent european materials r&d activities related to iter. *Journal of nuclear materials*, 329:173–177, 2004.

[112] M Roedig, W Kuehnlein, J Linke, D Pitzer, M Merola, E Rigal, B Schedler, and E Visca. Post irradiation testing of samples from the irradiation experiments paride 3 and paride 4. *Journal of nuclear materials*, 329:766–770, 2004.

[113] AF Lopeandia, E André, J-L Garden, D Givord, and O Bourgeois. Highly sensitive parylene membrane-based ac-calorimeter for small mass magnetic samples. *Review of Scientific Instruments*, 81(5):053901, 2010.

[114] Y Kong and JN Hay. The measurement of the crystallinity of polymers by dsc. *Polymer*, 43(14):3873–3878, 2002.

[115] J-L Garden, Hervé Guillou, Aitor Fernandez Lopeandia, Jacques Richard, J-S Heron, GM Souche, FR Ong, Benoit Vianay, and Olivier Bourgeois. Thermodynamics of small systems by nanocalorimetry: From physical to biological nano-objects. *Thermochimica Acta*, 492(1):16–28, 2009.

[116] Wonhee Lee, Warren Fon, Blake W Axelrod, and Michael L Roukes. High-sensitivity microfluidic calorimeters for biological and chemical applications. *Proceedings of the National Academy of Sciences*, 106(36):15225–15230, 2009.

[117] Sheng Shen, Arvind Narayanaswamy, and Gang Chen. Surface phonon polaritons mediated energy transfer between nanoscale gaps. *Nano letters*, 9(8):2909–2913, 2009.

[118] Matthew C Wingert, Zack CY Chen, Edward Dechaumphai, Jaeyun Moon, Ji-Hun Kim, Jie Xiang, and Renkun Chen. Thermal conductivity of ge and ge–si core–shell nanowires in the phonon confinement regime. *Nano letters*, 11(12):5507–5513, 2011.

[119] Takashi Kodama, Ankur Jain, and Kenneth E Goodson. Heat conduction through a dna- gold composite. *Nano letters*, 9(5):2005–2009, 2009.

[120] Jonathan B Chaires. Calorimetry and thermodynamics in drug design. *Annu. Rev. Biophys.*, 37:135–151, 2008.

[121] Alexander V Savin, Mikhail A Mazo, Irina P Kikot, Leonid I Manevitch, and Alexey V Onufriev. Heat conductivity of the dna double helix. *Physical Review B*, 83(24):245406, 2011.

[122] Dvira Segal, Abraham Nitzan, and Peter Hänggi. Thermal conductance through molecular wires. *The Journal of chemical physics*, 119(13):6840–6855, 2003.

[123] R Zenobi. Single-cell metabolomics: analytical and biological perspectives. *Science*, 342(6163):1243259, 2013.

[124] Geoffrey B West, William H Woodruff, and James H Brown. Allometric scaling of metabolic rate from molecules and mitochondria to cells and mammals. *Proceedings of the National Academy of Sciences*, 99(suppl 1):2473–2478, 2002.

[125] Carlo Canetta and Arvind Narayanaswamy. Sub-picowatt resolution calorimetry with a bi-material microcantilever sensor. *Applied Physics Letters*, 102(10):103112, 2013.

[126] Seid Sadat, Yi Jie Chua, Woochul Lee, Yashar Ganjeh, Katsuo Kurabayashi, Edgar Meyhofer, and Pramod Reddy. Room temperature picowatt-resolution calorimetry. *Applied Physics Letters*, 99(4):043106, 2011.

[127] Seid Sadat, E Meyhofer, and Pramod Reddy. High resolution resistive thermometry for micro/nanoscale measurements. *Review of Scientific Instruments*, 83(8):084902, 2012.

[128] Matthew C Wingert, Zack CY Chen, Shooshin Kwon, Jie Xiang, and Renkun Chen. Ultra-sensitive thermal conductance measurement of one-dimensional nanostructures enhanced by differential bridge. *Review of Scientific Instruments*, 83(2):024901, 2012.

[129] Deyu Li, Yiying Wu, Philip Kim, Li Shi, Peidong Yang, and Arun Majumdar. Thermal conductivity of individual silicon nanowires. *Applied Physics Letters*, 83(14):2934–2936, 2003.

[130] Olivier Bourgeois, Thierry Fournier, and Jacques Chaussy. Measurement of the thermal conductance of silicon nanowires at low temperature. *Journal of Applied Physics*, 101(1), 2007.

[131] JS Heron, T Fournier, N Mingo, and O Bourgeois. Mesoscopic size effects on the thermal conductance of silicon nanowire. *Nano letters*, 9(5):1861–1865, 2009.

[132] Jean-Savin Heron, Chandan Bera, Thierry Fournier, Natalio Mingo, and Olivier Bourgeois. Blocking phonons via nanoscale geometrical design. *Physical Review B*, 82(15):155458, 2010.

[133] Olivier Bourgeois, Emmanuel André, Cristina Macovei, and Jacques Chaussy. Liquid nitrogen to room-temperature thermometry using niobium nitride thin films. *Review of scientific instruments*, 77(12):126108, 2006.

[134] Lu Xue-Hui, Kang Lin, Zhou Lei, Chen Jian, Ji Zheng-Ming, Cao Chun-Hai, Jin Biao-Bing, Xu Wei-Wei, Wu Pei-Heng, and Wang Xiao-Shu. Growth and characterization of a kind of nitrogen-rich niobium nitride for bolometer applications at terahertz frequencies. *Chinese Physics Letters*, 25(11):4076, 2008.

[135] XueHui Lu, Ning He, Lin Kang, Jian Chen, BiaoBing Jin, and PeiHeng Wu. Nb5n6 thin film on silicon and silicon oxide: A good material for terahertz detection. *Chinese Science Bulletin*, 54(18):3344–3346, 2009.

[136] Nevill Francis Mott and Edward A Davis. *Electronic processes in non-crystalline materials*. OUP Oxford, 2012.

[137] L Lu, W Yi, and DL Zhang. 3ω method for specific heat and thermal conductivity measurements. *Review of Scientific Instruments*, 72(7):2996–3003, 2001.

[138] Xun Xu, Yong Hou, Xuyang Yin, Li Bao, Aifa Tang, Luting Song, Fuqiang Li, Shirley Tsang, Kui Wu, Hanjie Wu, et al. Single-cell exome sequencing reveals single-nucleotide mutation characteristics of a kidney tumor. *Cell*, 148(5):886–895, 2012.

[139] Matthias Heinemann and Renato Zenobi. Single cell metabolomics. *Current Opinion in Biotechnology*, 22(1):26–31, 2011.

[140] Richard N Zare and Samuel Kim. Microfluidic platforms for single-cell analysis. *Annual review of biomedical engineering*, 12:187–201, 2010.

[141] Daojing Wang and Steven Bodovitz. Single cell analysis: the new frontier in 'omics'. *Trends in biotechnology*, 28(6):281–290, 2010.

[142] R Fisher, L Pusztai, and C Swanton. Cancer heterogeneity: implications for targeted therapeutics. *British journal of cancer*, 108(3):479–485, 2013.

[143] Chuang Chen, Jun Peng, Heshun Xia, Qiongshui Wu, Libo Zeng, Hao Xu, Hongwu Tang, Zhiling Zhang, Xiaobo Zhu, Daiwen Pang, et al. Quantum-dot-based immunofluorescent imaging of her2 and er provides new insights into breast cancer heterogeneity. *Nanotechnology*, 21(9):095101, 2010.

[144] Andrei V Krivtsov, Scott A Armstrong, et al. Can one cell influence cancer heterogeneity. *Science*, 338(6110):1035–1036, 2012.

[145] Victor L Roggli, Robin T Vollmer, S Donald Greenberg, Malcolm H McGavran, Harlan J Spjut, and Raymond Yesner. Lung cancer heterogeneity: a blinded and randomized study of 100 consecutive cases. *Human pathology*, 16(6):569–579, 1985.

[146] Otto Warburg et al. On the origin of cancer cells. *Science*, 123(3191):309–314, 1956.

[147] Jane E Visvader. Cells of origin in cancer. *Nature*, 469(7330):314–322, 2011.

[148] Jung-whan Kim and Chi V Dang. Cancer's molecular sweet tooth and the warburg effect. *Cancer research*, 66(18):8927–8930, 2006.

[149] Gregg L Semenza. Tumor metabolism: cancer cells give and take lactate. *The Journal of clinical investigation*, 118(12):3835, 2008.

[150] Peggy P Hsu and David M Sabatini. Cancer cell metabolism: Warburg and beyond. *Cell*, 134(5):703–707, 2008.

[151] Heather R Christofk, Matthew G Vander Heiden, Marian H Harris, Arvind Ramanathan, Robert E Gerszten, Ru Wei, Mark D Fleming, Stuart L Schreiber, and Lewis C Cantley. The m2 splice isoform of pyruvate kinase is important for cancer metabolism and tumour growth. *Nature*, 452(7184):230–233, 2008.

[152] Rob A Cairns, Isaac S Harris, and Tak W Mak. Regulation of cancer cell metabolism. *Nature Reviews Cancer*, 11(2):85–95, 2011.

[153] Russell G Jones and Craig B Thompson. Tumor suppressors and cell metabolism: a recipe for cancer growth. *Genes & development*, 23(5):537–548, 2009.

[154] Matthew G Vander Heiden. Targeting cancer metabolism: a therapeutic window opens. *Nature reviews Drug discovery*, 10(9):671–684, 2011.

[155] David C Essaka, Jillian Prendergast, Richard B Keithley, Monica M Palcic, Ole Hindsgaul, Ronald L Schnaar, and Norman J Dovichi. Metabolic cytometry: capillary electrophoresis with two-color fluorescence detection for the simultaneous study of two glycosphingolipid metabolic pathways in single primary neurons. *Analytical chemistry*, 84(6):2799–2804, 2012.

[156] Peter Nemes, Ann M Knolhoff, Stanislav S Rubakhin, and Jonathan V Sweedler. Single-cell metabolomics: changes in the metabolome of freshly isolated and cultured neurons. *ACS chemical neuroscience*, 3(10):782–792, 2012.

[157] Peter J O'Brien, Michelle Lee, Mary E Spilker, Cathy C Zhang, Zhengming Yan, Timothy C Nichols, Wenlin Li, Caroline H Johnson, Gary J Patti, and Gary Siuzdak. Monitoring metabolic responses to chemotherapy in single cells

and tumors using nanostructure-initiator mass spectrometry (nims) imaging. *Cancer & metabolism*, 1(1):1–14, 2013.

[158] Alfredo J Ibáñez, Stephan R Fagerer, Anna Mareike Schmidt, Pawel L Urban, Konstantins Jefimovs, Philipp Geiger, Reinhard Dechant, Matthias Heinemann, and Renato Zenobi. Mass spectrometry-based metabolomics of single yeast cells. *Proceedings of the National Academy of Sciences*, 110(22):8790–8794, 2013.

[159] Ales Svatos. Single-cell metabolomics comes of age: new developments in mass spectrometry profiling and imaging. *Analytical chemistry*, 83(13):5037–5044, 2011.

[160] Petra Weber, Michael Wagner, Petra Kioschis, Waltraud Kessler, and Herbert Schneckenburger. Tumor cell differentiation by label-free fluorescence microscopy. *Journal of biomedical optics*, 17(10):1015081–1015085, 2012.

[161] Robert S Balaban. Allometry of brain metabolism. *Proceedings of the National Academy of Sciences*, 110(9):3216–3217, 2013.

[162] Matthew D Johnson, Jens Völker, Holly V Moeller, Edward Laws, Kenneth J Breslauer, and Paul G Falkowski. Universal constant for heat production in protists. *Proceedings of the National Academy of Sciences*, 106(16):6696–6699, 2009.

[163] Matthew G Vander Heiden, Lewis C Cantley, and Craig B Thompson. Understanding the warburg effect: the metabolic requirements of cell proliferation. *science*, 324(5930):1029–1033, 2009.

[164] Ralph J DeBerardinis, Julian J Lum, Georgia Hatzivassiliou, and Craig B Thompson. The biology of cancer: metabolic reprogramming fuels cell growth and proliferation. *Cell metabolism*, 7(1):11–20, 2008.

[165] J Lerchner, A Wolf, H-J Schneider, F Mertens, E Kessler, V Baier, A Funfak, M Nietzsch, and M Krügel. Nano-calorimetry of small-sized biological samples. *Thermochimica acta*, 477(1):48–53, 2008.

[166] T Yahata and A Kuroshima. Influence of endocrine and chemical factors on glucagon induced thermogenesis in brown adipocytes. *The Japanese journal of physiology*, 32(2):303—307, 1982.

[167] Yuyan Zhang and Srinivas Tadigadapa. Calorimetric biosensors with integrated microfluidic channels. *Biosensors and Bioelectronics*, 19(12):1733–1743, 2004.

[168] V Baier, R Födisch, A Ihring, E Kessler, J Lerchner, G Wolf, JM Köhler, M Nietzsch, and M Krügel. Highly sensitive thermopile heat power sensor for micro-fluid calorimetry of biochemical processes. *Sensors and Actuators A: Physical*, 123:354–359, 2005.

[169] Bin Wang and Qiao Lin. A mems differential-scanning-calorimetric sensor for thermodynamic characterization of biomolecules. *Microelectromechanical Systems, Journal of*, 21(5):1165–1171, 2012.

[170] Li Wang, David M Sipe, Yong Xu, and Qiao Lin. A mems thermal biosensor for metabolic monitoring applications. *Microelectromechanical Systems, Journal of*, 17(2):318–327, 2008.

[171] Taito Yamada, Naoki Inomata, and Takahito Ono. Sensitive thermal microsensor with pn junction for heat measurement of a single cell. *Japanese Journal of Applied Physics*, 55(2):027001, 2016.

[172] Tho Phuoc Huynh, Yilei Zhang, and Cohen Yehuda. Fabrication and characterization of a multichannel 3d thermopile for chip calorimeter applications. *Sensors*, 15(2):3351–3361, 2015.

[173] Xie Chang-Li, Sun Day-Ung, Song Zhau-Hua, Qu Song-Sheng, Guo Yu, and Li Bing. Microcalorimetric studies on tetrahymena pyriformis: part 1. growth metabolic power and thermal equations. *Thermochimica acta*, 183:117–123, 1991.

[174] X-J Chen, W Miao, Y Liu, Y-F Shen, W-S Feng, T Yu, and Y-H Yu. Microcalorimetry as a possible tool for phylogenetic studies of tetrahymena. *Journal of thermal analysis and calorimetry*, 84(2):429–433, 2005.

[175] XJ Chen, WS Feng, and YH Yu. Studies on the nongrowth metabolism of the different strains of tetrahymena cells by isothermal microcalorimetry. *Journal of Thermal Analysis and Calorimetry*, 115(3):2145–2149, 2014.

[176] XJ Chen, WS Feng, and YH Yu. Comparisons among six strains of tetrahymena by microcalorimetry. *Journal of Thermal Analysis and Calorimetry*, 115(3):2151–2158, 2014.

[177] Donna M Cassidy-Hanley. Tetrahymena in the laboratory: strain resources, methods for culture, maintenance, and storage. *Methods in cell biology*, 109:237, 2012.

[178] Siwei Zhang, Zihui Ling, Shulin Wang, Yoshinori Nozawa, and Shigenobu Umeki. Tetrahymena cell culture. *eLS*, 2010.

[179] Rong Wu, Johan H Huijsing, and Kofi AA Makinwa. Dynamic offset cancellation techniques for operational amplifiers. In *Precision Instrumentation Amplifiers and Read-Out Integrated Circuits*, pages 21–49. Springer, 2013.

[180] Claes G Granqvist and A Hultåker. Transparent and conducting ito films: new developments and applications. *Thin solid films*, 411(1):1–5, 2002.